THE INFLUENCE OF GEOMETRY VARIATION ON THE STRUCTURAL BEHAVIOUR OF A MASONRY BUILDING IN AN NLPO ANALYSIS

by

Roland M. van Dijk

TU Delft Delft University of Technology

THE INFLUENCE OF GEOMETRY VARIATION ON THE STRUCTURAL BEHAVIOUR OF A MASONRY BUILDING IN AN NLPO ANALYSIS

by

Roland M. van Dijk

MASTER OF SCIENCE THESIS

in partial fulfillment of the requirements for the degree of

Master of Science
in Structural Engineering

at the Delft University of Technology,
to be defended publicly on Tuesday, March 4, 2025 at 13:30

Student number:	4189469	
Thesis committee:	Prof. dr. ir. J.G. Rots,	TU Delft
	Prof. dr. ir. M.A.N. Hendriks,	TU Delft
	Dr. F. Messali,	TU Delft

An electronic version of this thesis is available at `http://repository.tudelft.nl/`.

TU Delft Delft University of Technology

ACKNOWLEDGEMENTS

Completing this Master of Science thesis has been a long and challenging journey, one that took significantly more time than I initially anticipated. While they say there are many roads to Rome, I somehow managed to take the scenic route — full of unexpected detours, obstacles, and learning experiences. Through it all, I have been fortunate to receive the patience, support, and encouragement of many individuals, without whom this achievement would not have been possible.

First and foremost, I would like to express my gratitude to my daily supervisor, Francesco, for his guidance, patience, and understanding. His expertise, constructive feedback, and encouragement have been invaluable, especially during the times when progress seemed slow. I also extend my sincere appreciation to my committee members, Jan and Max, for their insightful suggestions and support, which have helped refine this work.

To my family and friends, who not only supported me but also never missed an opportunity to remind me just how long this thesis was taking — your good-natured teasing kept me grounded and, in many ways, motivated me to push through to the finish line. I appreciate your humour, patience, and constant encouragement, even if it sometimes came with a playful eye roll.

A special thanks goes to my partner, Audrey, whose patience, love, and support have been a constant source of strength. Thank you for standing by me, even when my detour seemed never-ending. Your encouragement and belief in me have meant everything.

Although this journey took longer than expected, it has been an invaluable learning experience. To everyone who played a role in helping me reach this milestone — whether through academic guidance, emotional support, or simply reminding me to keep going — I offer my heartfelt thanks.

Roland M. van Dijk
Utrecht, February 21, 2025

ABSTRACT

Induced seismicity has been an issue in the area of Groningen in the north of the Netherlands. Due to gas extraction from the Groningen gas field, these induced earthquakes have occurred more frequently, especially since large-scale extraction began in the 1960s. Following the reduction of gas extraction since 2018, a slight decrease in the number of induced earthquakes has been observed. Nevertheless, severe damage to buildings in the Groningen area remains a significant risk. The building stock is largely composed of unreinforced masonry (URM) buildings, which were not designed according to a seismic code. These buildings were originally designed for wind resistance, providing limited lateral capacity, and making them vulnerable to earthquake forces.

The assessment of the seismic behaviour of unreinforced masonry has been extensively studied at Delft University of Technology. Within the framework of a large-scale testing campaign, a quasi-static cyclic pushover test on a masonry assemblage was performed at the Stevin II laboratory of Delft University of Technology, as discussed by Ravenshorst *et al.* [1, 2016]. This experimental campaign was designed to serve as a benchmark for both numerical and analytical models. The masonry assemblage, chosen to represent a typical terraced house built between 1960 and 1980 in the Groningen area, consists of calcium silicate masonry walls and concrete floors. Thereafter, finite element models were created to reproduce the experimental results Xu [2]. However, relying on a single configuration limits the study, and additional cases will be studied numerically in this work to explore a wider range of geometric variations.

The aforementioned research demonstrated the accuracy and applicability of the pushover method in assessing the seismic behaviour of the calcium silicate brick masonry assemblage. This research focuses on variations in geometry, specifically the introduction of spandrels with increasing height, and determining their influence on seismic behaviour. The influence is analysed based on capacity, crack propagation, and failure mechanisms. The model variations are symmetric and are analysed using the monotonic pushover method.

The following summarizes the objectives of this thesis:

- Create finite element models based on previously performed research, introducing spandrels of varying heights.
- Investigate the seismic response of different realistic masonry geometries through nonlinear pushover analyses.
- Compare and discuss the findings of the various models based on capacity, crack propagation, and failure mechanisms.

The research in this thesis is based on experiments conducted on a CS brick masonry assemblage at TU Delft [1], along with the calibrated numerical model by Xu [2, 2018]. The numerical model was created using DIANA FEA 10.8 commercial software. To account for anisotropic properties, the Engineering masonry model was used to model the CS brick masonry. A comparison of seismic behaviour across different variations of the masonry house is made, based on capacity curves, crack patterns, and failure mechanisms.

The finite element models were set up similarly to the calibrated numerical model by Xu [2, 2018] to explore the influence of geometric variations on seismic behaviour. Curved shell elements were used to model the masonry walls and concrete floors. A displacement-controlled approach, applied through a rigid frame

connected to the model, was used to induce equal forces on both floors, which is consistent with the experimental loading protocol. Nonlinear pushover analyses performed on the base model (without spandrels) and on a model with spandrels measuring 81 mm (half the floor thickness) showed no significant change in seismic behaviour due to the introduction of spandrels to the finite element model.

The introduction of larger spandrels into the finite element model increases the maximum base shear force. There is a positive relationship between spandrel size and the maximum base shear force: increasing spandrel height results in larger capacity. A similar positive relationship was found for the initial and secant stiffness of the finite element models. Stiffness increases with spandrel height, as does the ratio between secant and initial stiffness. The increasing ratio suggests less ductile behaviour with increasing spandrel height.

Deformation behaviour changes as spandrel height increases. Models with small spandrels display relatively uniform deformation over the height of the building, whereas models with higher spandrels show more concentrated deformation at the ground-floor level.

Damage to the piers primarily occurs in the bottom storey, regardless of spandrel height. However, for smaller piers, damage is more significant in the left pier, while damage is more evenly distributed between piers in models with greater spandrel height.

Smaller spandrels are associated with a rocking failure mechanism and the formation of shear cracks after significant damage. In contrast, shear cracks occur earlier in models with larger spandrels and become the dominant failure mechanism in models with the largest spandrel heights.

The out-of-plane failure mechanism in the transverse walls is influenced by spandrel height. With smaller spandrels, the out-of-plane mechanism is associated with a one-way spanning wall. Models with larger spandrels show an out-of-plane mechanism associated with a two-way spanning wall, due to cracks along the running bond connections with the piers. However, diagonal cracks commonly associated with this mechanism were not observed.

To further advance research in this area, it is recommended to investigate the overestimation of deformation capacity in the pushover method, particularly in models with spandrels of 300 mm or greater, where post-peak softening was not observed. Future studies should introduce additional geometric variations and explore their influence on seismic behaviour, such as the addition of outer leaves, common roof structures, and changes in bond types between walls and connections between piers and floors. This approach could also be applied to study the seismic behaviour of other common building types in the Groningen area.

CONTENTS

List of Figures

LIST OF TABLES

CHAPTER 1

INTRODUCTION

The Netherlands is not exposed to tectonic seismicity, except for low seismicity experienced in the south of the country. However, over the course of many years the area of Groningen has been subject to an increasing number of earthquakes. This area of the Netherlands is known for the presence of natural gas fields. The first natural gas was discovered near Slochteren in 1959, in 1960 gas with the same properties was found near Delfzijl. Concluded was the two were part of the same gas field, it turned out to be the largest field of Europe. In the years that followed the production was started. Continuous extraction of gas causes depletion of these gas fields, of which "induced" earthquakes are a result. The first tremor was recorded December 26th 1986, hereafter about one thousand more were recorded by The Royal Netherlands Meteorological Institute (KNMI). Most of these tremors had a magnitude smaller than 2.0 on the Richter scale, only three of them had a magnitude larger than 3.0 with a maximum magnitude of 3,6 in Huizinge [24].

Not only the frequency, but also the magnitude of the earthquakes has increased. Since The Netherlands is not a seismic country, buildings are not designed according to earthquake design guidelines. Typical houses in The Netherlands are made of unreinforced masonry (URM). This building material is strong in transferring vertical loads but has a low resistance for lateral loads and has brittle behaviour. Both of these properties contribute to the impact of earthquakes on URM houses. Many houses in the area of Groningen are subject to cracking and some buildings even collapsed. All of this contributed to the growing research interest for earthquakes and the consequences on structures.

Residents of the area are concerned for their property and their safety; this makes it also a political problem. This led Henk Kamp, Minister of Economic Affairs, to reduce the gas production. This measure, taken by the Minister, could be one of the reasons that according to calculations, performed by the KNMI in 2016, based on new data, the seismic threat above the Groningen gas field has decreased. These findings resulted in a new seismic hazard map for the area. In Loppersum, located in the centre of the gas field and one of the most affected towns, this means a reduction of the expected ground acceleration from 0.36g to 0.22g, with a probability of exceedance of one in 475 years [25]. Needless to say, this does not mean research of the topic should be discontinued. There is a strong need to get a better understanding of the structural response of URM buildings subject to earthquakes. Without this understanding, it is next to impossible to take adequate measures for existing structures as well as new structures. This is a necessity to let people live in this area without concern.

1.1 OBJECTIVES

At Delft University of Technology, several studies have been conducted with the goal to better predict and understand the behaviour of materials under earthquake conditions. In 2015, a large-scale quasi-static cyclic pushover test was performed on a calcium silicate (CS) masonry assemblage. The two-storey structure, composed of masonry walls and concrete floors, is a simplified representation of a typical Dutch terraced house built in the period between 1960 and 1980 in the Groningen area [1].

Since the accuracy and applicability of the pushover method have been validated [2], the research in this thesis will focus on varying geometry of the masonry assemblage. The CS brick masonry assemblage as tested at TU Delft was not a complete house; rather, it represented the essential structural elements that constitute the load-bearing structure in a building. It provides valuable insight into the expected capacity, crack patterns and failure mechanisms. However, the geometry could be more realistic. Additional information can be obtained by means of numerical simulations conducted with models adequately calibrated against the experimental test. By varying the geometry of the numerical model, more insight could be obtained of crack propagation and failure mechanisms in more realistic house configurations. The focus will be on the addition of spandrels and varying spandrel geometry in the numerical model. A point of interest is how crack propagation would change and if failure mechanisms would change due to the change in geometry. The new geometries are used to obtain a more realistic representation of a house found in the Groningen area.

The main question to answer is:

How do variations in facade geometry affect the structural response of unreinforced masonry (URM) terraced houses to lateral loading?

The following sub-questions are formulated to explore this question comprehensively:

- How does facade geometry impact the lateral load-bearing capacity of URM terraced houses?
- How does facade geometry affect the patterns and progression of crack propagation under lateral loading conditions?
- What are the primary failure mechanisms associated with various facade geometries under lateral loading conditions?

The research in this thesis is based on experiments on the CS brick masonry assemblage conducted at TU Delft [1]. The development of a numerical model calibrated to the experimental results was subject of a previous project by Xu [2] and serves as a starting point for the numerical models used in this research. The numerical models are created in commercial software DIANA FEA 10.8. To include the anisotropic properties, the Engineering masonry model is used to model the CS brick masonry. The discussion of and comparison between the seismic behaviour of the masonry house variations is mainly based on capacity curves, crack patterns, and failure mechanisms.

1.2 OUTLINE

The thesis consists of two parts. In the first part, a review of existing literature on masonry and earthquake analysis is carried out. The characteristics of masonry as a material and the ways it can be modelled are looked into (chapter 2). Then, seismicity in general, seismicity specifically in Groningen, and the ways seismic loads can be modelled are investigated, with a focus on the pushover method (chapter 3). Hereafter, a general setup of the finite element model of the masonry assemblage is described (chapter 4).

In the second part, the finite element modelling of the masonry structures is described per geometry variation. Then, the pushover analyses (described in subsection 3.2.2) on these models are performed, showing results per finite element model. Subsequently, the results are discussed, and a comparison is made between the outcomes of the different geometries (chapter 5). Finally, conclusions will be drawn, along with recommendations for further research. (chapter 6).

I

LITERATURE REVIEW

The goal of this part is to give an overview of existing literature on the seismic behaviour of unreinforced masonry structures. First, the material itself and its properties are highlighted. It is important to have an extensive understanding of the characteristics of the material itself prior to the main objectives of this thesis. To extend this understanding, the material response at a structural level is elaborated. Apart from the material characteristics itself, also the way it can be modelled will be elaborated, as well as the modelling of seismic loading. To gain a better understanding of the way seismic loads can be modelled, the seismicity in the Groningen area is elaborated and compared to other seismic regions. Hereafter, the finite element modelling of the calibrated base structure is elaborated. The base structure serves as a starting point of the geometry variations that will be applied in the second part of this thesis.

CHAPTER 2

MASONRY

In masonry, individual units are used to build a structure. Often, but not necessarily, these units are bound together by a kind of mortar. Different materials can be used for the masonry units, common materials in the Netherlands are clay- of calcium silicate bricks, but also various types of stone can be used. Masonry is one of the oldest building types around, e.g. the great pyramids in Egypt, and it is still used frequently. One of the reasons it is still used today, it is a highly durable form of construction. However, there are various conditions that can affect the durability of a masonry structure, e.g., the materials used, workmanship, quality of the mortar and the stacking pattern of the units. Apart from the durability, masonry is a cheap way of construction and structures can be built very quickly.

2.1 GENERAL

As mentioned, there are several factors that influence the performance of masonry. One of them is the stacking pattern. Masonry is an organised arrangement of bricks, whether or not bonded by mortar. The places where mortar can be applied are called the joints between the units, the horizontal joints are also called bed joints, and the vertical joints are often referred to as head joints. The arrangement of the bricks may be of influence on the structural behaviour of a masonry structure. Figure 2.1 gives an overview of common bond types in masonry. There are some variations on these six bond types, in particular on the vertical joints, which are not necessarily filled with mortar. The running bond is most frequently used in the Netherlands and also applied in the tests on the TU Delft house. Apart from the bond type also a distinction can be made in construction method. In Figure 2.2 different construction methods are depicted. Depending on region in the world and building culture of a country different construction methods are applied. In regions with low seismicity, it is common to use unreinforced masonry, while in more seismic active regions the application of reinforced- or confined masonry is more usual.

2.1.1 UNREINFORCED MASONRY

Unreinforced masonry (2.2a) is the typical construction method in areas with low seismicity, e.g., the Netherlands. It is, however, known to be traditionally used in almost every part of the world for the construction of low-rise houses. Structures with a load-bearing system of unreinforced masonry are vulnerable to seismic events. In many construction codes, this type of masonry is categorised as not earthquake resistant.

In the construction of URM, general-purpose mortar or thin layer mortar can be used. In case of general-purpose mortar, the joint thickness should be about $1,0$ to $1,5cm$ to avoid structural problems. In a thin layer mortar, e.g., for solid block masonry, the thickness of the joints is usually $1,0$ or $2,0mm$ thick.

2.1.2 REINFORCED MASONRY

In reinforced masonry (2.2b) there are steel bars embedded in the mortar. The bars may be placed in the bed joints and, if present, in the brick holes, which are then filled with grout. Both horizontal and vertical reinforcement serve another purpose. The horizontal reinforcement increases the resistance to horizontal loads; hence, it increases the resistance to shear failure. This is an important property in earthquake design,

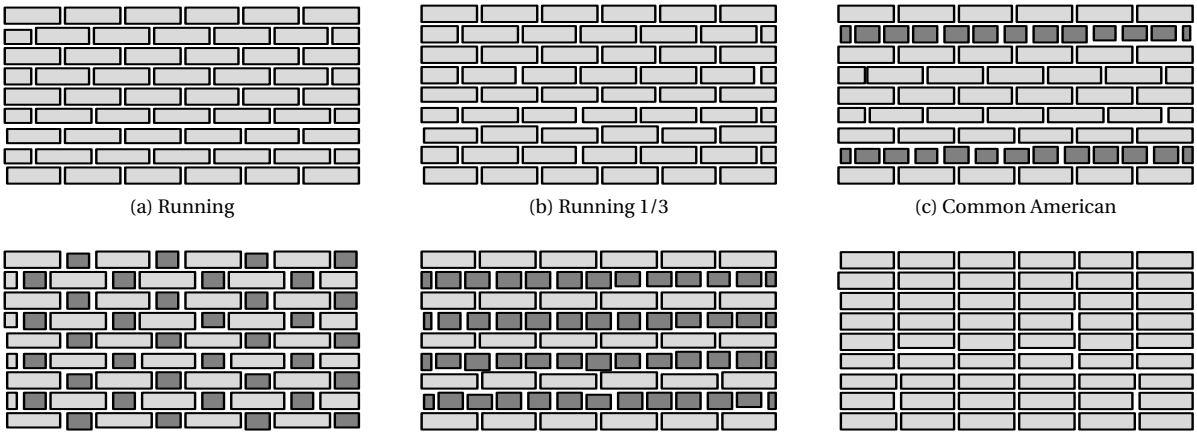

(a) Running (b) Running 1/3 (c) Common American

(d) Flemish (e) English (f) Stack

Figure 2.1: Bond types in masonry [3]

since, as mentioned in chapter 1, earthquake loads can be seen as horizontal loads. Vertical reinforcement, on the other hand, helps to improve the flexural resistance of a masonry structure.

In seismic areas, this type of masonry is often used and, in some cases, even obligatory. However, not everywhere in the world reinforced masonry is used at a sufficiently high level. Especially in underdeveloped countries, this is a serious problem, in particular the grout filling of vertical reinforcement bars is not done in a proper manner. In these countries, the damage caused by earthquakes has a more significant impact, as resources for reconstruction are limited. In other countries, the design of reinforced masonry structures is done in a regulated way, e.g., in Chile there is a specific design code for the design of these structures.

2.1.3 CONFINED MASONRY

Confined masonry, like reinforced masonry, is widely used in seismic areas and also sometimes obligatory. This type of masonry, as depicted in 2.2c, is confined within a reinforced concrete frame. This frame consists of vertical tie columns and a horizontal bond beam. The distribution of steel reinforcement in the intersection between the horizontal bond beams and columns is important and may influence the structural behaviour of a confined masonry structure. To obtain a good structural behaviour, design codes usually define requirements for the maximum area to be confined.

A distinction can be made in this type of masonry based on the construction order. If the masonry is built and then confined by the reinforced concrete, the structural system is called confined masonry. If, on the other hand, the reinforced concrete frame is built and then the masonry is built within, the structural system is called an infilled frame. The structural behaviour may differ based on the construction order, due to the application of the toothed wall edge in a confined masonry structure [26].

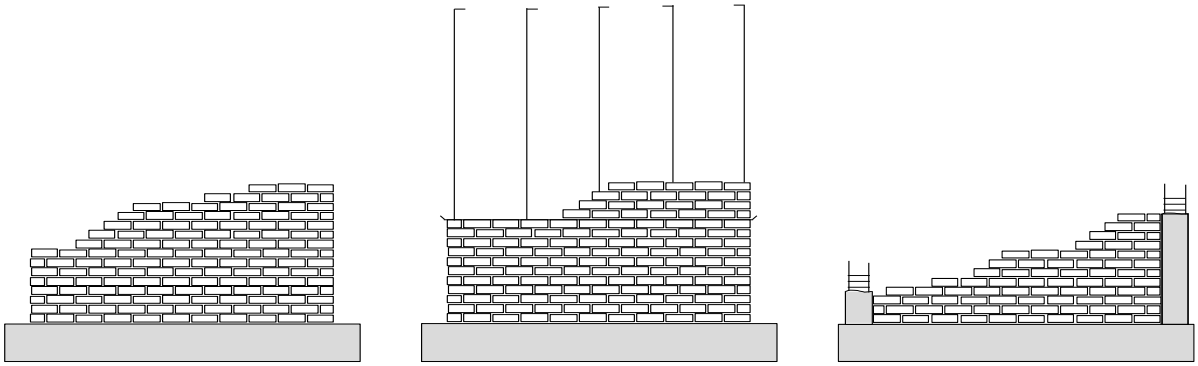

(a) Unreinforced masonry (b) Reinforced masonry (c) Confined masonry

Figure 2.2: Construction methods of masonry [3]

2.2 MATERIAL PROPERTIES

Unreinforced masonry is known for its good resistance to compressive loads and bearing of gravity loads. However, the resistance to lateral loads (e.g., wind and seismic loads) is significantly lower. This could be primarily attributed to the low tensile strength and quasi-brittle behaviour of masonry. To improve the behaviour of masonry, in case of lateral loading, the before mentioned reinforcement and confinement of masonry is often applied. However, in this thesis these two types of masonry are not considered, since the aim is to contribute to the research of masonry houses in the Groningen area, which are predominantly unreinforced masonry houses. From here on unreinforced masonry is referred to as "Masonry".

Masonry is a complex material, it is inhomogeneous, composed of bricks and mortar. As depicted in Figure 2.1, there are a lot of different ways to combine these elements, resulting in different compositions, which implies a variety of mechanical behaviour and structural performance. Not only composition, but also the properties of the constituents of masonry are of importance for the overall mechanical behaviour. The constituent elements have a strong nonlinear response to high demand loads. Masonry usually has different material properties for the vertical and horizontal direction respectively, hence, it' is an anisotropic material.

Traditionally, the compressive strength in the direction normal to the bed joint is regarded as the most relevant material property of masonry. The masonry community has accepted the difference in elastic properties between units and mortar as the precursor of failure [27]. The properties of bricks and mortar are often independently defined through experimental tests. These tests are widely described in literature and building codes. When tested separately, interaction between constituents is neglected. This could be a bad approximation, in particular for mortar, since the properties of mortar are affected by their interaction with units during hardening. Nowadays, there are also tests to determine the properties of masonry as a whole, considering a special geometric configuration and quality of the materials. These tests are also included in literature and building codes.

2.2.1 UNIT BEHAVIOUR

The properties of masonry units are subject to a great variability, depending on quality of commodities and manufacturing. As also applies to masonry as a whole, units are not homogeneous and isotropic. Material properties are not equal in different directions and also compressive and tensile behaviour are not the same [3]. Masonry units are classified as a quasi-brittle material with a disordered internal structure. In a quasi-brittle material, the transferred force does not immediately drop back to zero, it gradually decreases. This behaviour is often referred to as softening. The softening causes localization of deformations that causes quick growth of microcracks into macrocracks and finally to fully open cracks [4].

COMPRESSIVE BEHAVIOUR OF UNITS

Masonry bricks, as other stone like materials, have a better performance in compression than in tension, i.e. a higher compressive strength than tensile strength. Usually, a compressive test is performed to determine the mechanical behaviour of units. Generally, compressive strength tests provide a good indication of the

material quality. To obtain a complete characterization of the bricks, tests are performed in three orthogonal directions. The test results in a stress-strain curve of the bricks. From this curve, the characteristic compressive strength can be derived. A typical stress-strain diagram of a quasi-brittle material is shown in Figure 2.3.

The compressive behaviour of a quasi-brittle material can be classified in five distinctive components. In Figure 2.3 the transition of one stage to another is indicated by the letters "A" to "F". In the first stage, "A" to "B", existing pores and micro-cracks are closed, resulting in an increase of stiffness. The second stage, "B" to "C", is characterized as the linear elastic phase. At 30-40% of the conventional strength cracks are initiated and stable crack growth progresses, "C" to "D". This stage starts at a stress level of f_{ci}, mainly tensile cracks occur. The formation and growing of these microcracks result in a nonlinear increase of lateral- and volumetric strain. The following stage, "D" to "E", is characterized by crack damage and unstable crack growth. This stage of unstable microcracking starts at a stress level of f_{cd}, the crack damage stress. It is associated to the point where volume increase due to the cracking process exceeds the standard volumetric decrease as a result of the axial load, resulting in a volume increase. A rapid and significant increase of the lateral strain can be observed caused by the volume increase. Fracture surfaces parallel to the maximum principal stresses arise from bridging microcracks, until reaching the maximum compressive strength, f_c. The final stage of softening and growth of macrocracks, "E" to "F", is marked by the weakening of material as strain localization occurs. The rate of change in the stress strain diagram gives an indication of the materials brittleness, i.e., a sudden decrease of stress occurs in a brittle material, where a more gradual decrease is observed in a more ductile material. Macrocracks become unstable and crushing of the material occur at constant stress levels at the end of this stage.

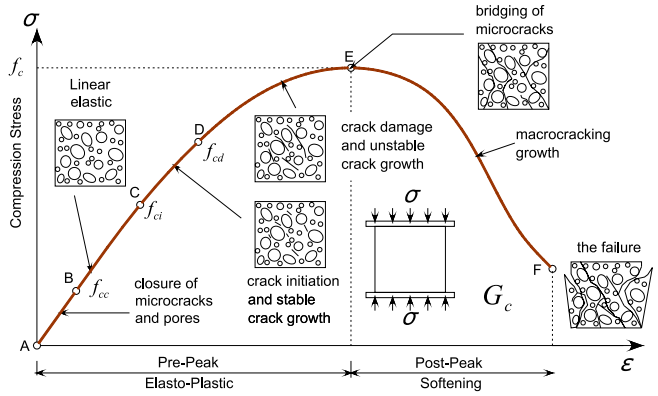

Figure 2.3: Typical compressive behaviour of a quasi-brittle material [4]

The previously mentioned uniaxial compressive test provides a good estimate of the material strength and damage behaviour. However, it is not sufficient when the general failure model of the material is important. For geo-materials, e.g. masonry constituents, it can be useful to perform a triaxial laboratory test to get more insight in the real material behaviour. A triaxial test is performed on a cylindrical specimen loaded with an axial- and a lateral stress, σ_1 and σ_3 respectively. In a triaxial state of stress the effective stress equals the stress difference: $\sigma_1 - \sigma_3$. As a result of the triaxial test a failure curve is obtained that describes the relation between the Von Mises stress (effective stress) and the hydrostatic pressure, 2.4a. This is one of the most important characteristics to describe the failure behaviour of many geo-materials. When the axial- and lateral stress are equal, the specimen is in hydrostatic compress with a pressure: $p = \frac{\sigma_1 + 2\sigma_3}{3} = \sigma$. From this state the axial- and lateral strain can be measures resulting in a relation between pressure and volume strain, describing the compaction behaviour of the material. The compaction can generally be divided in 4 stages, 2.4b:

1. The initial elastic response, $p_0 < p < p_1$. The elastic bulk modulus, K, is the slope of this part.

2. Compression of pores in the material, $p_1 < p < p_2$.

3. Full compaction of the material by removal of the voids, $p > p_2$.

4. Unloading from the fully compacted state. The bulk unloading modulus, K_{un}, is the slope of this part.

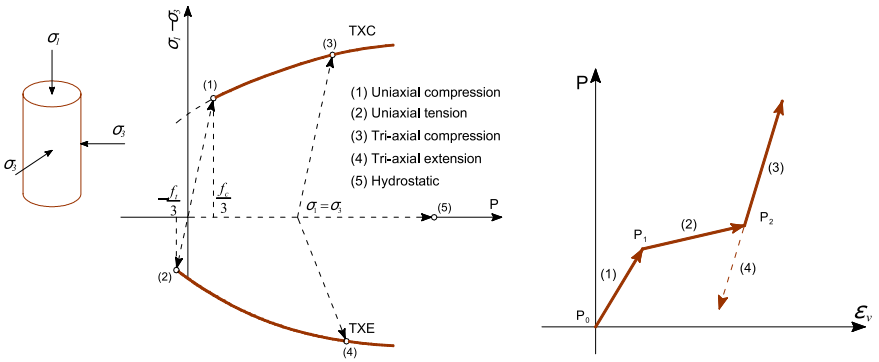

(a) Result from a triaxial test: relation between Von Mises stress and hydrostatic pressure

(b) Behaviour of geo-materials under hydrostatic compression

Figure 2.4: Triaxial test results [4, 5]

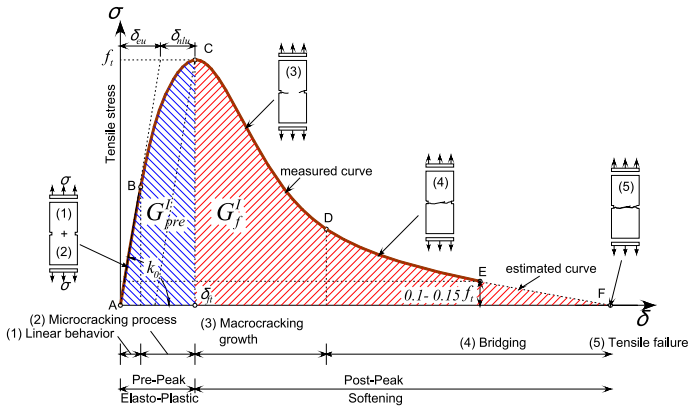

Figure 2.5: Typical uniaxial tensile behaviour of a quasi-brittle material [4]

TENSILE BEHAVIOUR OF UNITS

The tensile behaviour of masonry, a quasi-brittle material, is characterized by localization and propagation of microcracks. The tensile behaviour can be accurately described by the cohesive crack model proposed by Hillerborg *et al.* [28]. The tension softening process zone is included by means of a fictitious crack ahead of the visible crack. The Hillerborg model consists of two parts, a real crack, where stresses are no longer transferred and a damaged zone where stresses are still transferred. The model differentiates between two stages of the tensile behaviour:

1. Pre-peak stage, "A" to "C": This stage is characterized by an elasto-plastic stress-strain relationship. The relation holds until the peak stress is reached. After a small linear part, the behaviour starts to be nonlinear due to the formation of microcracks. The microcrack formation occurs in a stable manner, cracks only grow at increasing loads.

2. Post-peak stage, "C" to "F": The stage is characterized by softening behaviour around the fracture zone. A gradual stress decrease from the uniaxial tensile strength, f_t, to zero occurs, while strain increases. The behaviour is caused by the bridging of microcracks, forming macrocracks, around the peak load. The load has to be decreased to prevent the unstable macrocracks from uncontrolled growth. As a result of the stress transfer mechanism, caused by the bridging effect, the softening stage of the diagram (softening diagram) has a long tail. The softening diagram is characterized by the tensile strength (f_t) and fracture energy (G_f^I), defined as the area under the softening diagram.

STIFFNESS OF UNITS

According to Vasconcelos, a significant nonlinear relation between the tensile strength and initial stiffness in granites exists [6], Figure 2.6. The initial stiffness is calculated as the slope of the stress-strain relation up to

around 20% of the peak stress. In general, higher values of tensile strength are associated with stiffer granites. This relation is thought to be applicable to quasi-brittle materials in general.

However, the stiffness of masonry units is often obtained from the compressive part of the stress-strain relation. Since the development of microcracks starts at a relatively small load, obtaining the E-modulus from the linear-elastic part of the diagram is not a trivial task. There are various ways to determine the E-modulus from the compressive strength, these methods are based on values around 35% of the peak load in the $\sigma - \epsilon$-diagram. Effects of nonlinear behaviour due to microcracking is small in the first part of the diagram and becomes more significant further in the loading process. According to Barraza [3], the stiffness of clay bricks is in a range $150 f_b \leq E_b \leq 500 f_b$. For calcium silicate units, which are used in the TU Delft house, an estimate of the E-modulus is: $E_b = 355 f_b$.

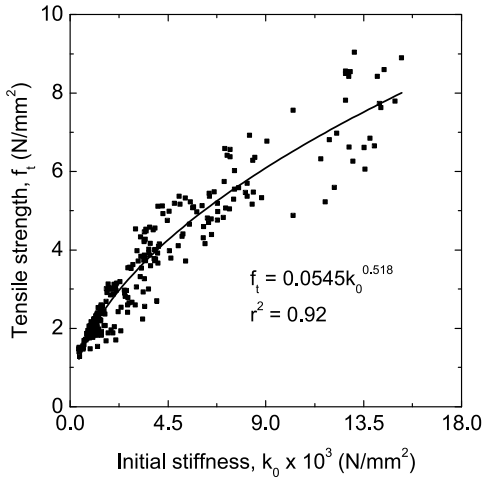

Figure 2.6: Correlation stiffness and tensile strength [6]

2.2.2 MORTAR BEHAVIOUR

The material behaviour of mortar is largely depending on the proportion of its components (sand, cement, gypsum and lime). To obtain a good performing masonry structure, in many cases, it is more important to have a good bond between mortar and unit than a high resistance mortar. Depending on the type of brick different types of mortar can be used, i.e. general-purpose mortar, thin layer mortar or lightweight mortar. General-purpose mortar is traditionally used in joints with a thickness larger than 3.0 or 4.0mm, in which only dense aggregate is used. Thin layer mortar is used in joints of $1.0 - 3.0$mm, or in case of specific requirements. Lightweight mortar is made with special lightweight components, this mortar is also used when specific requirements must be fulfilled.

COMPRESSIVE BEHAVIOUR OF MORTAR

The typical stress-strain relations for different types of mortar are shown in Figure 2.7, as found in experimental test performed in 2007 [7]. Three different grades of mortar were tested, i.e. weak-, intermediate- and strong mortar. The applied volume ratio of cement:lime:sand for the three grades of mortar were 1:0:6, 1:0.5:4.5 and 1:0:6 respectively. The compressive strength of mortar strongly depends on the water-cement ratio and cement content of mortar, it is therefore necessary to perform experimental test to determine strength properties of mortar. Two main methods can be distinguished, one method uses a bulk mortar prism or cylinder, the other method uses a disk from a masonry joint. The latter takes into account water adsorption caused by adjacent units, which influences strength properties.

TENSILE BEHAVIOUR OF MORTAR

Various tests can be performed to determine the tensile behaviour of mortar, e.g. the "uniaxial tensile strength test", "splitting tensile test", and the "flexural tensile strength". These tests are well known from literature, Figure 2.8 shows an example of a flexural tensile test performed by Bergami [8].

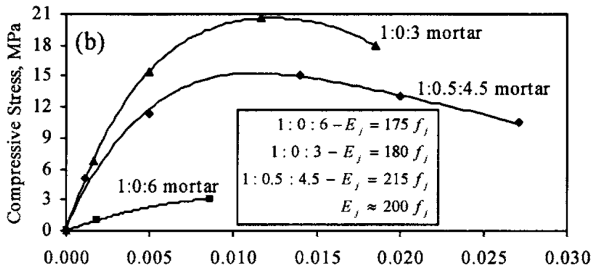

Figure 2.7: Compressive stress-strain relation in mortar [7]

(a) Mortar before loading

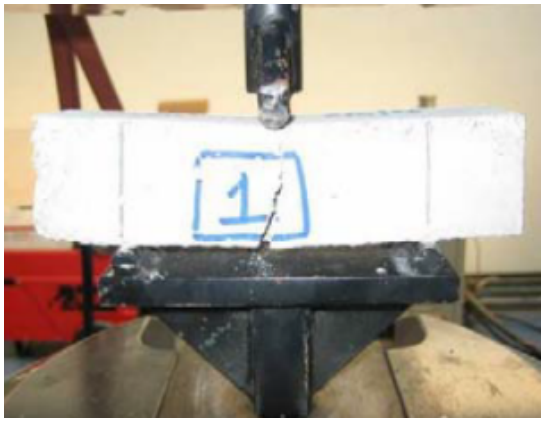

(b) Mortar after flexural crack formation

Figure 2.8: Flexural tensile test [8]

STIFFNESS OF MORTAR

An estimate of the modulus of elasticity of a mortar cube can be made by means of the compressive strength, according to Kaushik, Raj & Jain [7]. Tests on twenty-seven mortar cubes of different grades, show the stiffness to be in a range $100 f_j \leq E_j \leq 400 f_j$. The average value of the stiffness can be estimated by the relation $E_j = 200 f_j$, this estimate provides a good coëfficient of correlation ($C_r = 0.90$) with the observed experimental results, Figure 2.9.

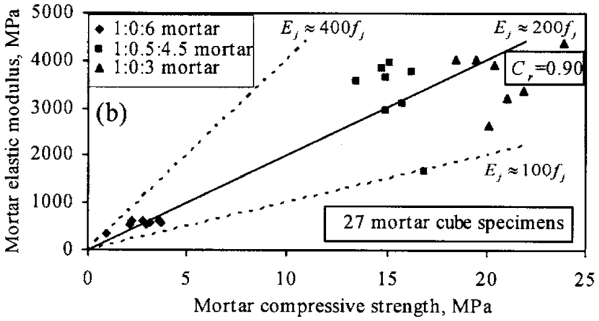

Figure 2.9: Relation between stiffness and compressive strength in mortar [7]

2.2.3 UNIT MORTAR INTERFACE BEHAVIOUR

The bond between unit and mortar has a significant influence on the overall behaviour of masonry structures. The unit-mortar interface is often the weakest link, and therefore one of the main reasons for masonry failure, especially in historic masonry. Strength of the unit-mortar interface is highly dependent on various properties, i.e. porosity of the mortar, water retention capacity of the mortar, absorption capacity of the units, curing conditions and binders in the mixture [4]. The nonlinear response of joint, caused by the unit-mortar

interface, is one of the most relevant features of masonry behaviour. Two main failure mechanisms can be distinguished for the unit-mortar interface, i.e. tensile failure (mode I) and shear failure (mode II), according to Lourenço [9].

MODE I FAILURE

Tensile strength of a brick-mortar interfaces can be determined by means of various experimental tests, some tests are described by Almeida *et al.* [29]. Solid clay and calcium-silicate units were tested in a deformation-controlled manner by van der Pluijm [30], these tests resulted in an exponential tension softening curve. The mode I fracture energy G_f^I associated with this softening curve ranges between 0.005 and $0.02 Nmm/mm^2$ for tensile bonding stresses in a range $0.3 - -0.9 N/mm^2$. The amount of energy required to form a unitary area of a crack along the unit-mortar interface is defined as the fracture energy. Further investigation of the cracked specimen revealed a reduced bond area, the so-called net bond surface, see Figure 2.11. The average surface of this area is about 35% of the total cross-sectional area, for walls this surface is estimated to be about 59% of the total cross-sectional area [9].

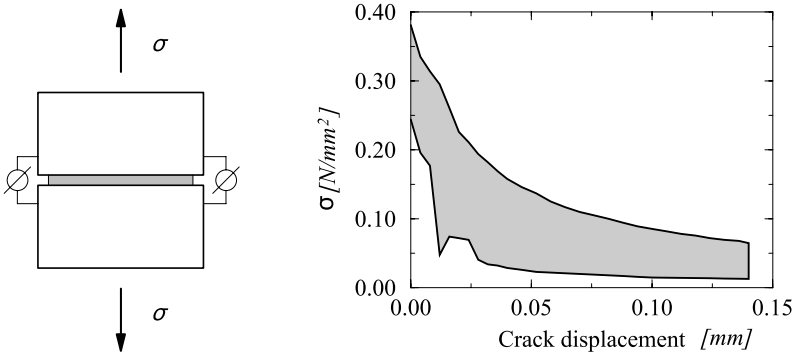

(a) Test specimen

(b) Typical experimental results of stress-crack displacement for solid clay brick masonry

Figure 2.10: Tensile bond behaviour of masonry [9]

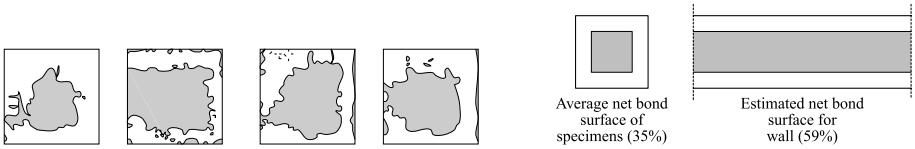

(a) Typical net bond surface for tensile specimen of solid clay units

(b) Extrapolation of average net bond surface from specimen to wall

Figure 2.11: Tensile bond surface [9]

MODE II FAILURE

To determine the shear response of masonry joints, it is required to generate a uniform stress state in the joints, a suitable test set-up is necessary. As a result of the equilibrium constraints non-uniform normal stresses develop in the joints, therefore it is difficult to satisfy the condition of a uniform stress state. The usability of different test configurations is widely described in literature, the reader is referred to Van der Pluijm and Atkinson [10, 31]. The most complete characterization of the masonry shear behaviour, for solid clay and calcium-silicate units, is presented by Van der Pluijm [10]. The applied test set-up permits to keep a constant normal confining (compressive) pressure upon shearing. Three different levels of compressive stress were applied: 0.1, 0.5 and $1.0 [N/mm^2]$. A constant normal confining pressure upon shearing can be achieved by making use of the test setup as described in Figure 2.12. Tensile confining stresses were not possible in this test setup and low confining stresses were also problematic, since they resulted in extremely brittle results and potential instability of the setup. Several test specimens with higher confining stresses resulted in shearing of the unit-mortar interface accompanied by diagonal cracking of the units.

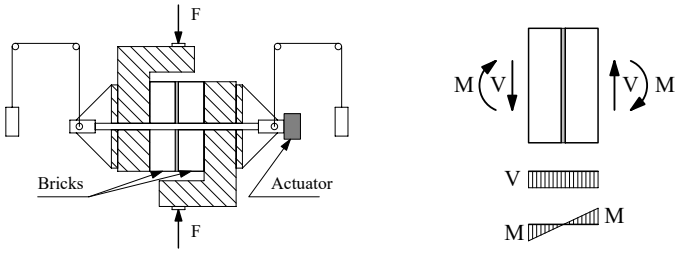

(a) Test specimen before testing

(b) Forces acting on specimen during testing

Figure 2.12: Test setup, used by Van der Pluijm [10], to obtain shear bond behaviour [9]

Experimental tests on the illustrated setup resulted in an exponential shear softening diagram with a residual dry friction level. These results are depicted in 2.13a, the mode II fracture energy G_f^{II} is defined by the area between the stress-displacement diagram and the residual dry friction. For initial cohesion [c] values ranging from 0.1 to 1.8[N/mm^2], the mode II fracture energy varies between 0.01 and 0.25[Nmm/mm^2]. From 2.13a can be concluded the fracture energy is also dependent on the applied confining stress, this relation is also depicted in 2.13b.

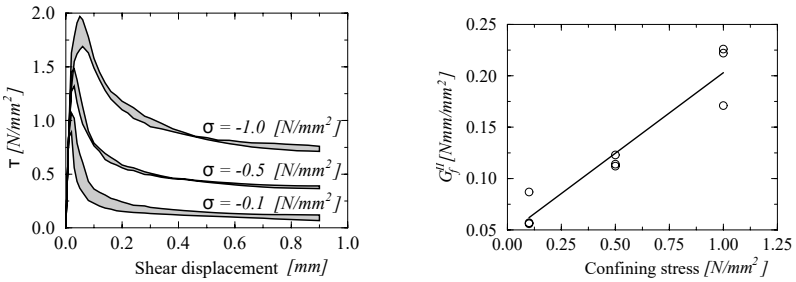

(a) Stress-displacement diagram for varying normal stresses

(b) Mode II fracture energy G_f^{II} as a function of the normal stress

Figure 2.13: Solid clay unit shear bond behaviour in joints as found by Van der Pluijm [9, 10]

Determining tensile bond strength values by means of evaluating the net bond surface is no longer possible, but the measured values are assumed to hold. Additional material properties can be obtained from experiments. The shear strength can be analysed as a function of the normal stress, based on the Coulomb friction model. The initial friction angle ϕ_0, associated with this model, is measured by $\tan\phi_0$, which ranges from 0.7 to 1.2 for different unit mortar combinations. In a similar manner, the residual friction angle ϕ_r is measured by $\tan\phi_r$, which is approximately constant with a value of 0.75. The uplift of one unit over another unit upon shearing is defined as the dilatancy angle ψ, 2.14b. This angle is not independent on the level of confining stress, a relation between the tangent of the dilatancy angle and the confining stress is presented in 2.15a. Depending on the roughness of the unit surface, for low confining stress, the value of $\tan\psi$ ranges from 0.2 to 0.7. Higher confining stress results in a decrease of $\tan\psi$ to zero. Smoothing of the sheared surface with increasing slip also influence the dilatancy angle and causes a decrease to zero.

2.2.4 MASONRY AS A COMPOSITE

In many cases it is not sufficient to determine the behaviour of all the masonry constituents, masonry should be considered as a whole in these cases. In this manner, interaction between units and mortar and the geometrical arrangement of the units can be included in the results. A variety of tests can be performed to determine composite behaviour. One of these tests is a compression test for Rilem specimen (2.17b), resulting in a stress-strain curve. Another test to determine several material properties of masonry is the diagonal compression test on walls. By varying the direction of the load with respect to the bed joint the influence

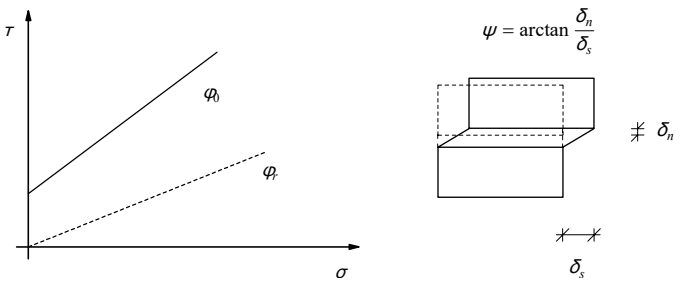

(a) Coulomb friction law, with initial and residual friction angle

(b) Dilatancy angle as the uplift of neighbouring units upon shearing

Figure 2.14: Friction and dilatancy angles as presented by Lourenço [9]

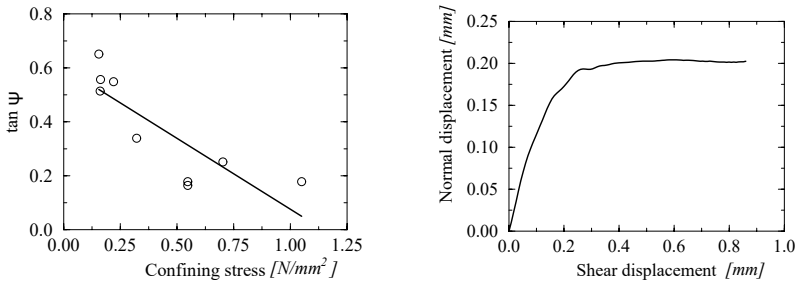

(a) Tangent of the dilatancy angle ψ as a function of the normal stress

(b) relation between the normal and the shear displacement upon loading

Figure 2.15: Typical shear bond behaviour of the joints for solid clay units as found by van der Pluijm [10], [9]

of this parameter can be determined, this is an interesting alternative in the diagonal compression test [3]. More extensive research on these tests is carried out by Anthoine [32], Bergami [8], Charry [33], Grabowski [34], Page [12]. In Figure 2.16, the failure modes for varying loading cases and varying angles compared to the bed joints θ as described by Dhanasekar *et al.* [11] are shown.

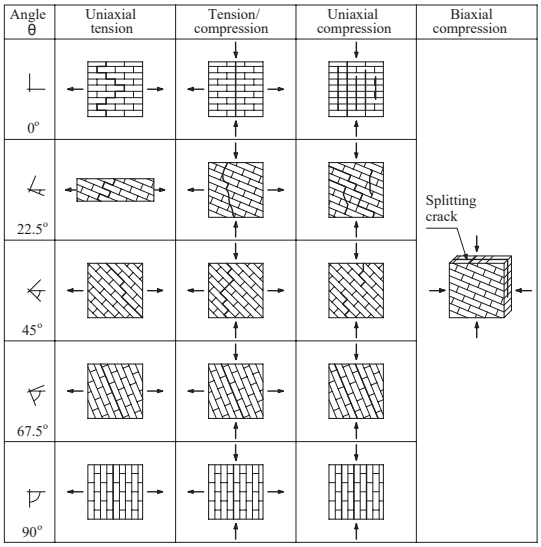

Figure 2.16: Failure mechanisms of masonry subject to different loads as presented by Dhanasekar *et al.* [11]

STIFFNESS

The stiffness of masonry as a composite is not as widely researched as other material properties. According to Eurocode 6, in the absence of a value determined by experiments, the short-term secant modulus of elasticity, used for structural analysis, can be estimated as $K_E f k$. K_E. Where K_E is a factor (700 in the Dutch National Annex) and f_k the characteristic compressive strength [35, §3.7.2]. Kaushik *et al.* [7] found a similar approximation of the modulus of elasticity, i.e. $E_m = 550 f'_m$. Where f'_m is the compressive prism strength of masonry (MPa). The used data resulted in a relatively good coëfficient of correlation ($C_r = 0.63$) between the experimentally observed and estimated values of E_m.

UNIAXIAL COMPRESSIVE BEHAVIOUR

Until the introduction of numerical methods for masonry structures, the compressive strength of masonry in the direction normal to the bed joints was regarded as the sole relevant material property. An often-used test to determine this uniaxial compressive strength is the stacked bond prism (2.17a). However, it is not clear how the use of this kind of specimens affects the masonry strength. The before mentioned test on Rilem specimen, often referred to as a compression test on a masonry wallet, is commonly accepted to yield the real uniaxial compressive strength, see 2.17b. However, this test is costly to execute, and the specimen is relatively large compared to a standard cube or cylinder test for concrete. In the masonry community it is widely accepted that the difference in elastic properties of the unit and mortar is the precursor of failure [9].

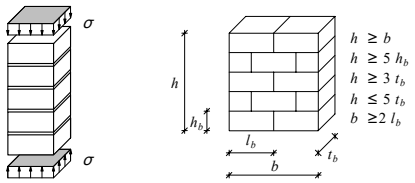

(a) Stacked bond prism

(b) Rilem test specimen

Figure 2.17: Masonry specimens used to determine uniaxial compressive behaviour [9]

UNIAXIAL TENSILE BEHAVIOUR

In case of loading perpendicular to the bed joint, a rough estimate of the masonry tensile strength is given by the tensile bond strength between the joint and the unit. Tensile failure is generally caused by the relatively low bond strength between the bed joint and unit, therefore this is often a good approximation, see Figure 2.16 bottom left. In other types of masonry, where unit strength is low and bond strength is higher, failure may occur as a result of stresses exceeding the unit tensile strength. In these cases, e.g. high strength mortar and units with many perforations, which cause a dowel effect, the masonry strength can by approximated by the unit tensile strength.

Two different types of failure can be distinguished, depending on relative strength of units and joints, in case of loading parallel to the bed joint, i.e. a zigzag crack through bed- and head joints and an almost vertical crack through head joints and units. The first type of failure is characterized by a residual plateau upon increasing deformation in the stress-displacement diagram. The post-peak behaviour is generally determined by the fracture energy of the head joints and the post-peak mode II behaviour of bed joints, see Figure 2.16 top left. The second type of failure is typically represented by a stress-displacement diagram which shows a progressive softening until zero. The post-peak behaviour is generally determined by the fracture energy of the units and head joints, see Figure 2.16 top middle [9].

BIAXIAL BEHAVIOUR

Uniaxial tests can provide a good indication of masonry material behaviour; however, it cannot completely describe the constitutive behaviour of masonry subject to biaxial stress states. To obtain a biaxial strength envelope, the influence of biaxial stress state has to be investigated up to peak stress. Since masonry is an anisotropic material, the strength envelope cannot fully be described in terms of principal stresses. It can be described in terms of the principal stresses, however, rotation angle θ between principal stresses and material

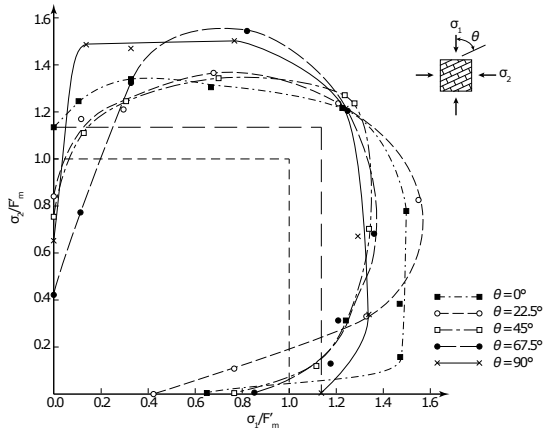

Figure 2.18: Failure surface for masonry projected onto the $\sigma_1 - \sigma_2$ plane as presented by Page [12]

axes should be included. Another way of describing the biaxial stress envelope is in terms of the full stress vector in a fixed set of material axes.

The most complete set of experimental data of masonry subjected to proportional biaxial loading was assembled by Page [12, 36]. The tests were carried out with half scale solid clay units. Both the orientation of the principal stresses with regard to the material axes and the principal stress ratio considerably influence the failure mode and strength [9]. The different modes of failure are illustrated in Figure 2.16, see also Figure 2.18 for the failure surface of masonry projected onto the $\sigma_1 - \sigma_2$ plane.

2.3 MASONRY FAILURE MECHANISMS

As a material of structural components several failure mechanisms of masonry can be distinguished. In de following subsections (subsection 2.3.1 and subsection 2.3.2) the most common in-plane and out-of-plane failure mechanisms for unreinforced masonry walls subject to earthquake loading are described.

2.3.1 IN-PLANE FAILURE

Three types of masonry failure mechanisms can be distinguished for masonry subject to in-plane loads. Two failure mechanisms are caused by shear, i.e. sliding and diagonal cracking, while the third one, rocking failure, is a flexural mechanism.

SLIDING SHEAR FAILURE

Sliding-shear failure, as observed in masonry structures, is distinguished by the displacement of the masonry element within its own plane. This movement results in a progressive loss of bearing capacity, a phenomenon that can have negative consequences for structural stability. Introduction of horizontal cracks, usually at one of the extremities of a pier, in the bed-joints indicate the initial stage of sliding-shear failure, as shown in 2.19a. Sliding-shear failure tends to occur only in very squat piers Calderini *et al.* [37].

The likelihood of sliding-shear failure is notably heightened when masonry structures are subjected to low levels of vertical loads. These reduced vertical loads result in a diminished ability to resist lateral forces, making the structure more susceptible to sliding along its own plane.

Another critical factor contributing to sliding-shear failure is the friction coefficient at the interface between masonry components. When the friction coefficient is low, it amplifies the potential for sliding-shear failure, as the resistance to lateral displacement decreases.

DIAGONAL SHEAR FAILURE

Diagonal-shear failure is typically introduced by the formation of a diagonal crack, usually starting at the centre of a masonry pier, and propagating to the corners under increasing lateral load [37]. The crack can either, predominantly pass through mortar joints, or also through the bricks. The first one can be distinguished by the formation of a 'stair-stepped' crack. In 2.19b the damage pattern associated with diagonal shear failure is shown. Diagonal shear failure tends to occur more often than sliding shear and flexural failure in moderately slender piers for increasing levels of vertical compression [37].

Increasing levels of vertical compression may also cause diagonal cracking through bricks to occur rather than through mortar. Increasing ratios between mortar- and brick strength tend to have the same effect.

A transition from diagonal cracking through the mortar to sliding shear, diagonal cracking through bricks or rocking may be introduced by increasing interlocking of bricks. The interlocking is determined by the aspect ratio of the bricks and masonry pattern.

FLEXURAL FAILURE

Flexural failure may include two failure mechanisms, commonly occurring in slender piers. When the vertical load applied to the pier is relatively low compared to its compressive strength, a horizontal load induces tensile flexural cracking primarily at the corners of the structure, as shown in 2.19c. Under such conditions, the pier's behaviour begins to mimic that of a nearly rigid body, exhibiting rotational movement about its toe, a phenomenon commonly known as "rocking".

Conversely, when a high vertical load is applied, preventing significant flexural cracking, the pier undergoes a distinct pattern of damage. In this scenario, a widespread damage pattern emerges, characterized by sub-vertical cracks oriented toward the corners experiencing higher compressive forces, often termed "crushing".

In both cases, the ultimate limit state of failure is achieved when structural integrity is compromised at the corners subjected to the highest compressive forces, as depicted in 2.19c.

2.3.2 OUT-OF-PLANE FAILURE

When an unreinforced masonry structure is exposed to lateral shaking caused by seismic activity, as a consequence the majority of its walls undergo a combination of in-plane and out-of-plane responses. Previous studies concerning the seismic response of unreinforced masonry structures have predominantly centred on

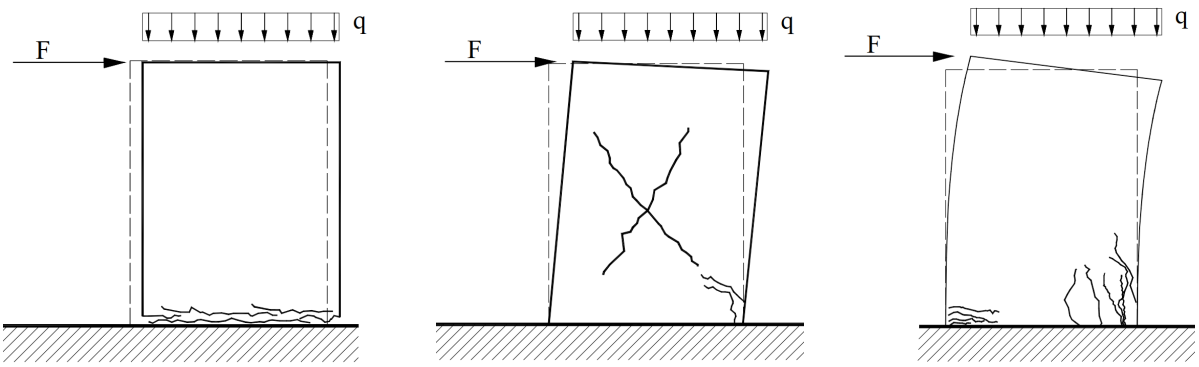

(a) Shear-sliding (b) Shear-diagonal (c) Flexural-rocking

Figure 2.19: Masonry in-plane failure mechanisms

the in-plane shear behaviour of walls. This emphasis is due to its essential role as the primary load-bearing path for transmitting the lateral seismic forces from the building to its foundation, as shown in Figure 2.20. Although out-of-plane behaviour is typically not regarded as an integral component of the building's seismic load path, it is essential for walls to possess adequate capacity to prevent out-of-plane collapse. This is crucial because even localized failure can present significant risks to life safety. Moreover, the failure of load-bearing walls has the potential to initiate a partial or total structural collapse by undermining the structure's ability to resist gravity or lateral in-plane loads.

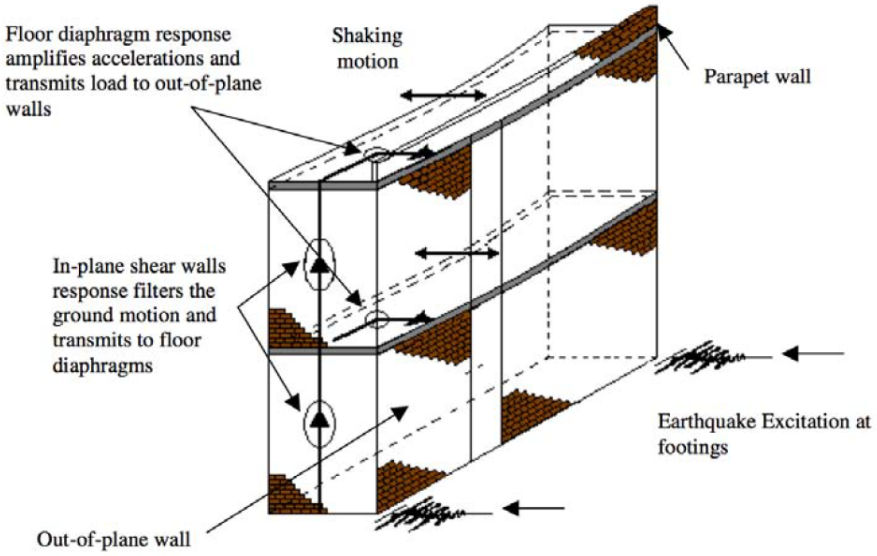

Figure 2.20: Seismic load path as presented by Doherty [13]

Therefore, it is important to have a good understanding of the mechanisms occurring when an unreinforced masonry wall is loaded out of plane, e.g. due to wind or earthquake loading. As a result of out-of-plane loading a wall it experiences flexural deformation (bending). The orientation of internal stresses within the wall and the resulting pattern of cracks that develop are determined by the positioning of its supporting edges, as illustrated in Figure 2.21. One-way spanning walls (as shown in 2.21a) undergo uniaxial bending, which can be categorized as either vertical or horizontal depending on the orientation of the span. Consequently, cracks tend to form parallel to the supports of the wall and the axis of internal bending.

The conventional terminology used to describe vertical and horizontal bending originates from the alignment of the principal flexural stresses induced by the applied bending moment. Vertical bending generates flexural stresses that act perpendicular to the bed joints, as depicted in 2.22a. In contrast, horizontal bending results in flexural stresses that are oriented perpendicular to the head joints, as shown in 2.22b. It is impor-

tant to clarify that the direction of crack formation is counterintuitive to the names given. Vertical bending corresponds to the development of horizontal cracks, while horizontal bending leads to the formation of vertical cracks[14].

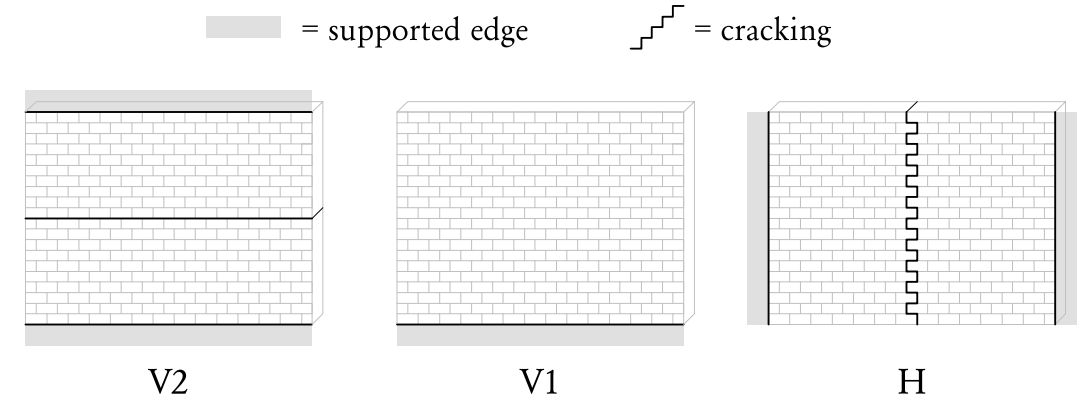

(a) One-way spanning walls, vertically (V1 and V2) and horizontally (H)

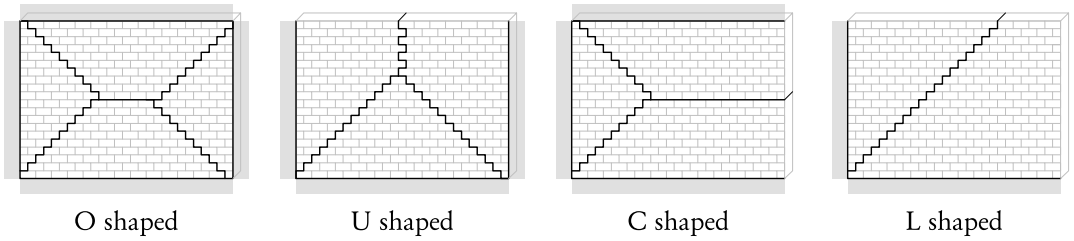

(b) Two-way spanning walls

Figure 2.21: Various wall support configurations and their corresponding patterns of out-of-plane flexural cracking, as illustrated by Vaculik [14]

On the other hand, the behaviour of two-way spanning walls, which is the case for any wall configuration supported on at least one vertical edge and one horizontal edge, result is a more complex response. This complexity arises from the anisotropic nature of masonry materials and the structural indeterminacy of such wall configurations. These walls undergo biaxial bending, by which the resulting internal flexural stresses act in vertical as well as horizontal direction. Consequently, two-way spanning walls typically exhibit crack patterns comprising a combination of horizontal, vertical, and diagonal crack lines.

Furthermore, the internal moments along the various types of crack lines may include a combination of flexural (normal stress) and torsional (shear stress) components, as illustrated in 2.22c [14].

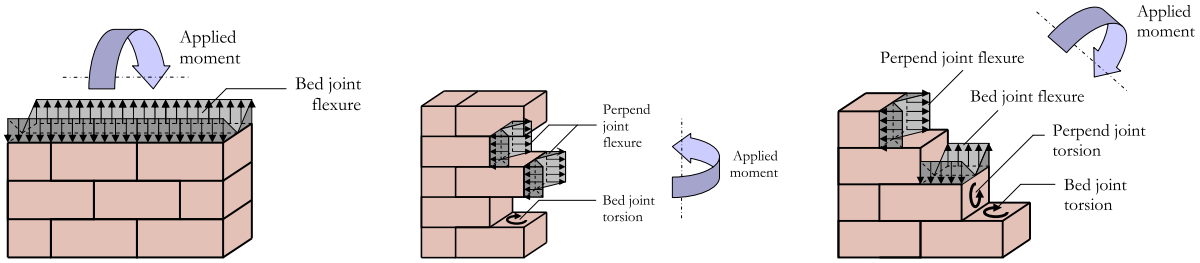

(a) Vertical bending (b) Horizontal bending (c) Diagonal bending

Figure 2.22: Mechanics of internal moment resistance for various types of bending, as illustrated by Vaculik [14]

2.4 MODELLING OF MASONRY

Masonry is a heterogeneous material and its mechanical behaviour is mainly determined by the properties of its constituents, as explained in section 2.2. Therefore, it is not a trivial task to model the behaviour, let alone a general method to apply when modelling a masonry structure. There has been extensive research on the topic of masonry modelling, resulting in various proposals to model masonry adequately. Every method has its benefits and its shortcomings, the most suitable method is mainly determined by the structure which is modelled. In general, the methods can be classified in two separate categories, i.e. micromodelling and macromodelling.

The level of detail included in the model is the main difference between micro- and macromodelling, hence, the ability to yield accurate results can be different. In a micromodel the individual components, i.e. units and mortar, are modelled separately, in contrast to a macromodel, where masonry is modelled as a composite [9]. Between micromodelling and macromodelling is an intermediate level of detail called simplified micromodelling, shown in 2.23c, this type of modelling is also referred to as mesomodelling.

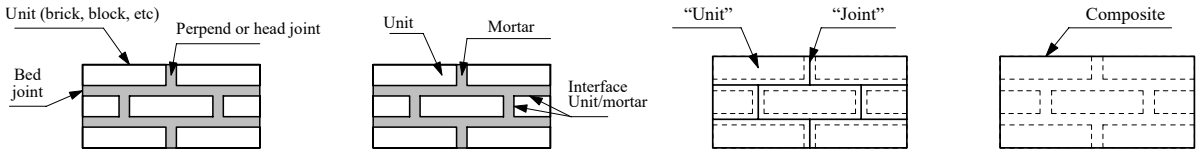

(a) Masonry sample (b) Detailed micromodel (c) Simplified micromodel (d) Macromodel

Figure 2.23: Various strategies for masonry modelling as described by Lourenço [9]

2.4.1 MICROMODELLING

Micro-models have been used to describe the behaviour of masonry since the beginning of masonry modelling. It is the most intuitive, and logical, way to model masonry. As all the individual components in a micromodel are modelled separately, it is a time-consuming task to build a model following this approach. Both bricks and mortar are modelled as continuum elements with defined failure criteria. The interfaces between the two are modelled separately by special elements, which can represent a potential crack/slip plane. These elements are given an initial dummy stiffness to avoid interpenetration of the continuum. All the properties of the constituents should be known to obtain a useful model, furthermore, there is a great number of degrees of freedom [38]. Due to this detailed level of modelling, most failure mechanisms of masonry are represented in this type of modelling [3]. Hence, micromodels are particularly useful when studying the behaviour of single structural elements, e.g. a wall or a floor [38].

In a simplified micromodel the units are defined similar to the detailed micromodel, however, the mortar joints and interface elements are lumped in an "average" interface. Each interface consists of mortar and two unit-mortar interfaces. In order to keep the geometry unchanged, the units are expanded. Using this approach implies considering masonry as a set of elastic blocks bounded by potential crack/slip planes at the joints. Poisson's ratio of the mortar cannot be included; therefore, accuracy is lost and less failure mechanisms are represented by these models [9].

The most important aspect of a detailed micromodel is the ability to describe most failure mechanisms accurately, Andreaus [39] defined ten mechanisms. The most basic failure mechanisms that characterize masonry, namely cracking of the joints, sliding along the bed or head joints at low values of normal stress, cracking of the units in direct tension, diagonal tensile cracking of the units at values of normal stress sufficient to develop friction in the joints and masonry crushing, commonly identified with splitting of units in tension as a result of mortar dilatancy at high values of normal stress, should in any case be identified by the model [9]. In Figure 2.24 these failure mechanisms are shown, they can be divided in joint mechanisms (2.24a, 2.24b), unit mechanisms (2.24c) and combined mechanisms (2.24d, 2.24e). To consider these phenomena into a simplified micromodel all damage is concentrated into the relatively weak joints and, if necessary, in potential pure tensile cracks in the units placed vertically in the middle of each unit. Lourenço [9] showed that failure envelopes resulting from this approach are in accordance with those found in experiments and therefore it can be considered a good alternative to a micromodelling approach.

In a finite element model the mechanical behaviour is described by a material model. A well described example of a simplified micromodel is the composite interface model, which includes three failure criteria.

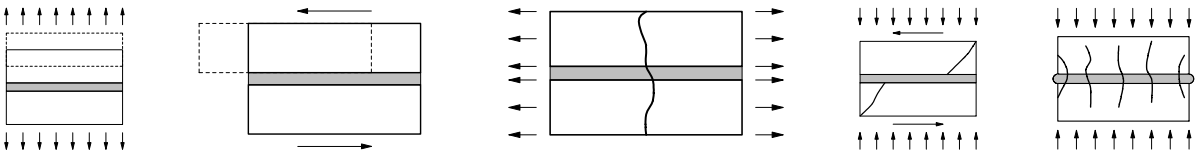

(a) Joint tensile crack (b) Joint slip (c) Unit direct tensile crack (d) Unit diagonal tensile crack (e) Masonry crushing

Figure 2.24: Basic failure mechanisms of masonry as depicted by Lourenço [9]

Namely, a tension cut-off criterion to include mode I failure, a Coulomb friction envelope for mode II failure and a compressive cap criterion for compressive failure. Assuming all inelastic phenomena occur in the interface elements, this type of modelling a structure is capable of following the complete load path until complete degradation of the stiffness in a robust and stable manner [9].

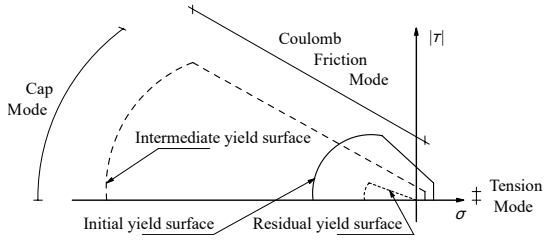

Figure 2.25: Interface cap model proposed by Lourenço [9]

2.4.2 MACROMODELLING

There is not a distinction between units, mortar, and unit-mortar interfaces in a macromodel, their properties are smeared out over a homogeneous anisotropic continuum. A macromodel is also referred to as a single-phase material model. These models treat masonry as an ideal homogeneous material which constitutive equations differ from those of its constituents [4]. The geometrical arrangement of units and mortar cause anisotropy in the effective constitutive behaviour, even if the properties of the constituents are isotropic [15].

In general, a macromodel requires fewer input data than a micromodel and usually it is easier to construct a model following this approach. The reduced time and memory requirements as well as the user-friendly mesh generation in macromodelling makes it more practise oriented, it is valuable when a compromise between accuracy and efficiency is required. As a result of the way a macromodel is made, they are particularly useful in situations where the general structural behaviour of masonry walls with sufficient large dimensions is of importance, in contrast to micromodelling where local behaviour is of importance. This assumption can be justified when stresses along or across a macrolength are approximately uniform [9]. The type of model may be able to represent the general structural behaviour, however not all types of failure mechanisms can be reproduced.

The macroscopic failure behaviour is directly related to the mesoscopic structure, damage localizes in narrow zones with an order of magnitude equal to that of the thickness of mortar joints. To obtain an accurate description of both the failure modes and the associated energy dissipation, this localization phenomenon should be considered properly in terms of its size and orientation [40]. The shift from a micromodel to a macromodel, i.e. from local structural behaviour to more global structural behaviour, is called homogenisation.

HOMOGENISATION TECHNIQUES

Some assumptions are required in the homogenisation process of a composite material since it is not possible to include all material behaviour in the model. A deliberate choice over what behaviour should be included and what behaviour can be excluded is of paramount importance for a useful model. The main objective is to make as few assumptions as possible in order to most fully describe the actual behaviour. Many researchers have developed homogenisation techniques for masonry, such as Dhanasekar *et al.* [11], Gambarotta and

Lagomarsino [41], Van Zijl [42], Berto *et al.* [43]. Each of these techniques have their shortcomings, often omitted phenomenon are post-peak behaviour and localized damage. The assumption that a material model based on proportional loading is also valid for non-proportional loading conditions is often made, however this validity can be doubted due to the effect of damage induced anisotropy. Damage induced anisotropy together with bond induced anisotropy, periodic geometry and nonlinearity are important aspects of homogenisation techniques [38].

One of the more straightforward methods to obtain an accurate constitutive model is by means of experimental tests. Tests have to be performed to determine material parameters and the composite behaviour of masonry as described in section 2.2 on page 13. These results are then used to fit a material model, with a multi-yield or single-yield surface. The main disadvantage of this approach is the number of required experimental tests and their associated cost. Another limitation of this approach is the validity of the model, since the material model is only valid in the range of the material parameters obtained from the experiment. Therefore, such material models are not immediately applicable to other situations. An example of a, widely discussed and well documented, material model based on experimental results is the Rankine-Hill model. This phenomenological model is based on an approach that extends conventional formulations for isotropic quasi-brittle materials to describe orthotropic behaviour. In this case a Hill type yield criterion for compression and a Rankine type yield criterion for tension are applied, see Figure 2.26.

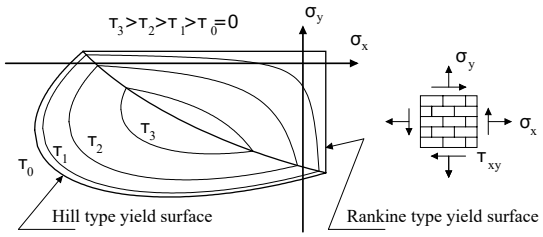

Figure 2.26: Rankine-Hill composite yield surface with iso-shear stress lines with different strength values for tension and compression along each material axis proposed by Lourenço *et al.* [15]

Another approach researched by different authors is a two-step homogenisation procedure. In this approach a masonry basic cell, i.e. a periodic pattern associated to some frame of reference, is used (Figure 2.27). However, the structure of a masonry basic cell is clearly not layered, these authors suggested an approximate approach based in a two-step homogenisation procedure, under the assumption of layered materials.

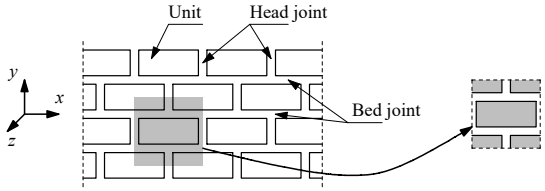

Figure 2.27: The definition of the masonry basic cell depicted by Lourenço [9]

Pande *et al.* [44] used a process where in the first step a horizontal homogenisation is performed, including both vertical joints and units. In step two the vertical homogenisation is performed of the previously homogenised material and the horizontal joints, see Figure 2.28b. Papa [45] used the opposite approach, i.e. first a vertical homogenisation is performed subsequently a horizontal homogenisation is performed. The vertical homogenisation includes the units and vertical joints as well as the units and the horizontal joints. In the second step the previously obtained materials are used and horizontally homogenised, see Figure 2.28c. Bear in mind, both methods will produce different results, hence, the procedures are not objective. This is the case even in a linear elastic analysis, let alone when nonlinear behaviour is present, the differences are expected to grow [9].

In addition to this two-step approach there is another approach which can be regarded as a one-step technique, both bed joints and head joints are introduced simultaneously. The basis of this approach lies in the identification of a certain repetitive shape within the masonry bond, to take the bond pattern into account [38]. This repetitive shape is also known as a Representative Volume Element (RVE) and is an intermediate step in the homogenisation process. This approach is widely applied in homogenisation research,

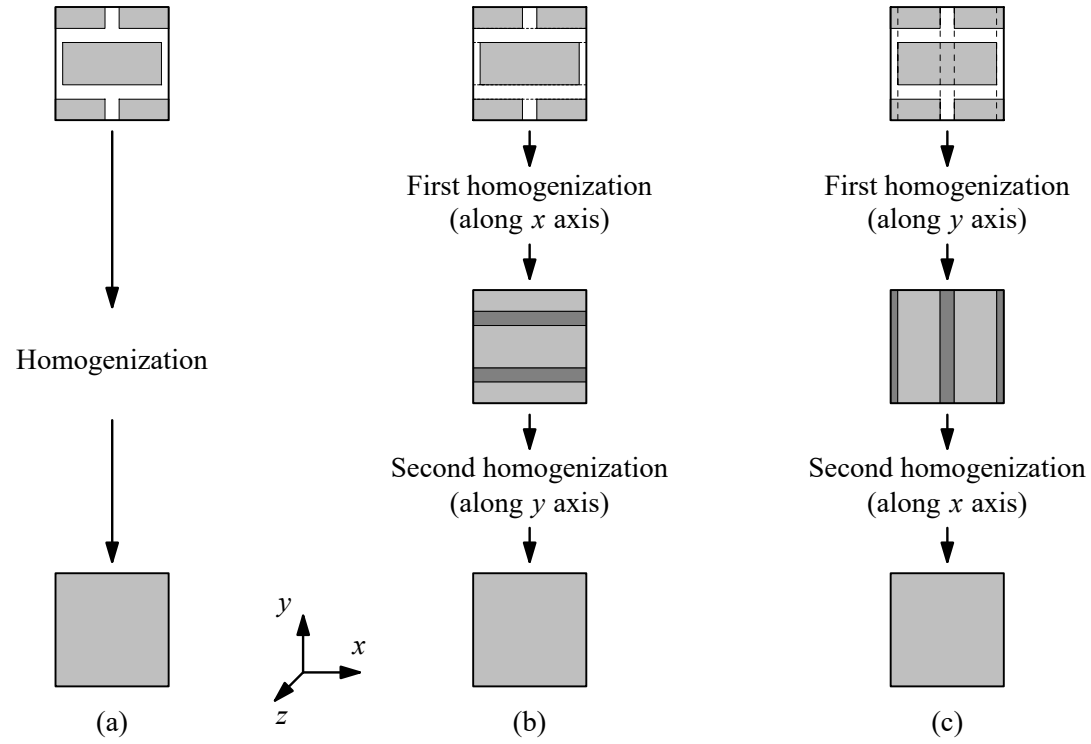

Figure 2.28: Two-step homogenisation procedure usually adopted for masonry structures as depicted by Lourenço [9]: (a) objective of homogenization; (b) homogenisation $x-y$; (c) homogenisation $y-x$

e.g. Anthoine [46], Luciano and Sacco [47], Cecchi and Di Marco [48], Cecchi and Di Marco [49], Zucchini and Lourenço [50] and Massart *et al.* [51].

Multi-scale homogenisation is a technique which seems rather paradoxical, since homogenisation is almost completely avoided. Luciano and Sacco [47] have tried to nest the mesoscopic scale into the macroscopic scale, in contrast to the above-mentioned methods where the main property is scale bridging. However, it is very difficult to implement this multi-scale homogenisation technique into a numerical model [38].

2.4.3 CONSTITUTIVE MODELS FOR SMEARED CRACK MACROMODELLING OF MASONRY

There are a lot of similarities between the material behaviour of masonry and concrete, e.g. their relative high resistance in compression and low tensile strength. Therefore, one could question the necessity of a special way to model masonry. A lot of literature is available on concrete smeared-crack models. These models should be applicable to masonry as well, given appropriate material properties of masonry are used. A few smeared crack model types can be distinguished, which can be separated into two categories, i.e. total strain-based crack models and a multidirectional crack model [23]. A short overview of these models is given below:

MULTIDIRECTIONAL FIXED CRACK MODEL

In the multidirectional fixed crack model, cracking is defined as a combination of tension softening, tension cut-off and shear retention. Crack initiation inside an element is governed by the tension cut-off criterion and a threshold angle between two consecutive cracks. To initiate successive cracks two criteria must be met simultaneously, i.e. the principal tensile stress violates the maximum stress condition and the angle between the existing crack and the principal tensile stress exceeds the value of a threshold angle. However, it is possible that the tensile stress temporarily becomes greater than three times the tensile strength while the threshold angle is still not violated, especially for high values of the threshold angle [23, 52]. The direction of all cracks is fixed upon initiation, and therefore does not change in a modified stress state.

TOTAL STRAIN-BASED CRACK MODELS

The total strain-based crack models follow a smeared approach for the fracture energy, like the multidirectional fixed crack model. In a total strain-based constitutive model the stresses are describes as a function of

the strains. A commonly used approach is the coaxial stress–strain, also known as the rotating crack model. Stress-strain relations are evaluated in the principal directions of the strain vector, implying, after the exceedance of a tension cut-off criterion, an element is considered to be cracked and continuously updated with the direction of the principal strain of the element.

A method where the physical nature of cracks is more preserved, is the fixed stress–strain concept. Essentially, it is very similar to the other strain-based crack model, however, the stress–strain relations are evaluated in a fixed coordinate system which is fixed upon cracking.

As stated above the main difference between the three variants lies in the orientation of the crack, which is either kept constant (fixed single), updated in a stepwise manner following a threshold angle (fixed multidirectional), or updated continuously (rotating). The damage orientation is permanently preserved in the fixed crack concept, which is not the case for the rotating crack concept. Consequently, inactive defects cannot be re-activated during a subsequent stage of the loading process in the rotating crack concept, which could influence the outcome when a nonproportional loading process is followed [52].

However, using these models for masonry applications can result in incorrect outcomes. It neglects masonry's anisotropic characteristics and significantly underestimates energy dissipation during cyclic loading. Additionally, these models do not differentiate between tensile and shear cracks, making it unable to accurately simulate the various failure modes observed in masonry.

ENGINEERING MASONRY MODEL

To overcome these shortcomings the engineering masonry model was developed. It is designed for modelling the failure of masonry walls using plane stress (membrane) and curved shell elements. Unlike the Total Strain crack models, which underestimate energy absorption during cyclic loading in masonry, the Engineering Masonry model provides a more realistic representation of unloading behaviour with strong stress decay and includes a shear failure mechanism based on the Coulomb friction failure criterion. Other distinctive features that make it a valuable tool for analysing the behaviour of masonry structures are the consideration of the anisotropic nature of masonry, acknowledging differences in stiffness along the bed and head joints. Furthermore, several failure mechanism are considered, i.e. tensile cracking of the bed joint, compressive crushing in the direction normal to the bed joint, tensile cracking of the head joint, compressive crushing in the direction normal to the head joint, cracking in the direction normal to diagonal stair step cracks, frictional shear sliding, out-of-plane shear failure. The engineering masonry model is applied in Diana to model the calcium-silicate masonry assemblage. In subsection 4.3.1 the finite element modelling of the structure is described and a more in depth description of the engineering masonry model is given.

CHAPTER 3

SEISMICITY

The majority of earthquakes worldwide are caused either by local fault lines or originate from edges of tectonic plate boundaries. Earthquakes of the former category are called crustal or shallow earthquakes. Different types of earthquakes can occur depending on the type of tectonic plate, i.e. oceanic or continental, and the direction of the movement of the plate. These plates can move in three distinct directions, divergent, convergent or of the transform fault type where plates move past each other. An example of convergent movement of tectonic plates is near Panama, where oceanic and continental plates move towards each other. A phenomenon called subduction occurs here, the denser oceanic plate moves underneath the less dense continental plate. The so-called subduction earthquakes, which are caused by a rupture in the boundary between oceanic and continental plates, have a low rate of occurrence but have high magnitudes. Crustal earthquakes usually have a much lower magnitude but occur random and are therefore rather unpredictable. They occur away from tectonic plate boundaries in fault lines, they are caused by sudden stress relief, hence the unpredictability. Fault lines are planar fractures in rock where both sides move in different directions, see Figure 3.1. A reverse fault, 3.1c, with small dip angle is also referred to as a thrust fault [53]

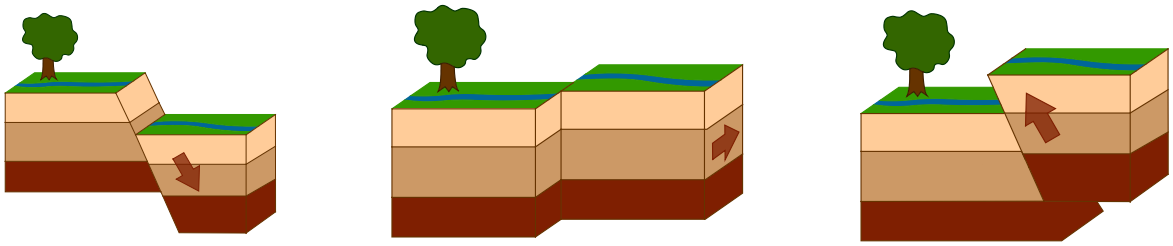

(a) Normal fault (b) Strike-slip fault (c) Reverse fault

Figure 3.1: The three principal fault types [16]

3.1 GENERAL OVERVIEW OF SEISMIC WAVES AND SEISMICITY IN GRONINGEN

There are two types of seismic waves caused by earthquakes; both propagate in a different manner through the earth. A distinction between body waves and surface waves can be made, both can propagate either by means of compression or shear. Body waves are called P-waves or S-waves, surface waves are called Rayleigh or Love waves. A seismograph can register these seismic waves when it is located close enough to the source of the earthquake. The registration provides information on the location of the hypocentre and epicentre of the earthquake, since body waves have a higher wave speed compared to surface waves and therefore will be recorded first. In Figure 3.2 the epicentre is indicated with "A", the hypocentre with "B" and the fault plane with "C". The hypocentre is the point within the earth where an earthquake rupture starts, also called the focus [54]. Directly above this point on the surface of earth is the epicentre located [55].

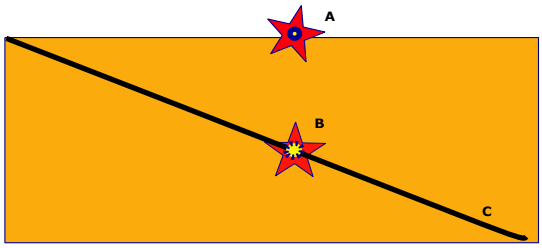

Figure 3.2: Hypocentre and epicentre of an earthquake [17]

Body waves travel through the earth's interior depending on the material properties of the medium, density and stiffness are determining factors for the path of a body wave. Surface waves, on the other hand, travel along the earth's surface and they diminish when they get further from the surface. In an ideal homogeneous flat elastic surface, waves are non-dispersive. In a more realistic situation, e.g. in an inhomogeneous solid where density varies with depth, wave velocity depends on the wavelength.

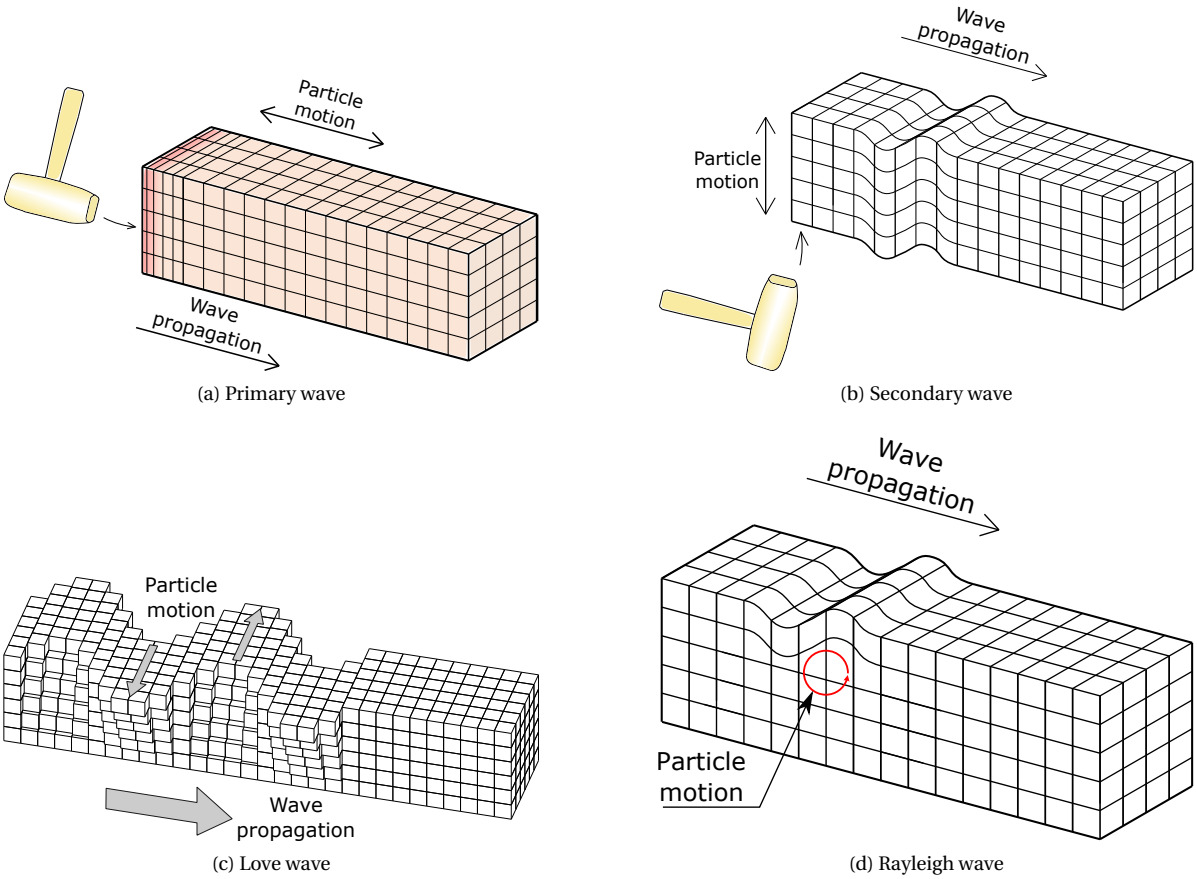

(a) Primary wave

(b) Secondary wave

(c) Love wave

(d) Rayleigh wave

Figure 3.3: Four types of seismic waves, body- and surface waves [18]

In Figure 3.3 the behaviour of the four seismic waves is shown. Primary waves are compressional waves and are longitudinal in nature, which means, the displacement of the medium is in the same direction as, or the opposite direction to, the direction of propagation of the wave. They are the fastest propagating seismic waves, hence the name primary waves, it is the first signal recorded by a seismograph.

A secondary wave, or shear wave, propagates as a transverse wave, the displacement of the medium is perpendicular to the direction of wave propagation. The name secondary wave originates from the moment when these waves are registered by a seismograph, an S-wave propagates at approximately 60% of the speed

of a P-wave.

Love waves are categorized as seismic surface waves, they cause horizontal shifting of the earth during an earthquake. Love waves are transverse waves, the particles move in a horizontal line perpendicular to the direction of wave propagation. They are formed by the interaction of S-waves with Earth's surface and propagate at a speed of around 90% of an S-wave which is slightly faster than Rayleigh waves. Generally, Love waves are what people feel directly during an earthquake.

Rayleigh waves are surface waves and travel as ripples on the earth's surface. When a Rayleigh wave passes by soil particles follow an elliptical path, closer to the surface this motion is greater. Although the speed of a Rayleigh wave varies with the medium it travels in, typically its speed is about 90% of an S-wave. However, generally slightly slower than Love waves.

In Figure 3.4 an example of what a seismogram is gives with the arrival of the different seismic waves, as stated above the arrival of a wave is determined by the medium and the distance, this figure is just an indication.

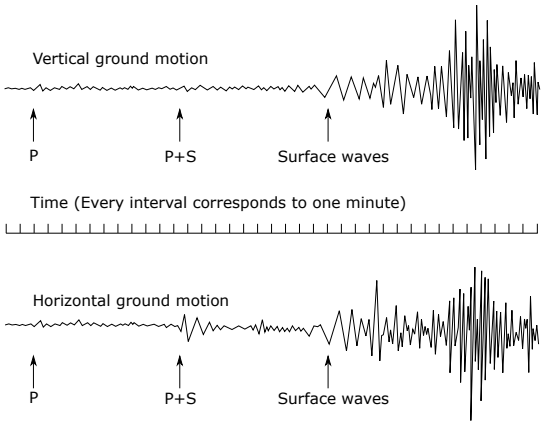

Figure 3.4: An example of seismogram with the arrival seismic waves

The heaviest earthquakes registered in the Netherlands was caused by a local fault line and occurred in the south of the country. In 1992 an earthquake with a magnitude of 5.8 on the Richter scale was measured near Roermond, which was the strongest earthquake measured in the Netherlands and one of the strongest ever in North-west Europe.

The earthquakes in the Groningen area are of another type, they follow from human activity. These so-called induced earthquakes are typically minor earthquakes that alter the stresses and strains in the earth's crust. There are several mechanisms that could cause induces seismicity. The mechanism causing earthquakes in Groningen is the extraction of fluids. It causes a decrease of pore pressure in the reservoir, with a resulting stress change that is transferred to the surrounding levels.

In Groningen gas is captured at a depth of 3000 m in sandstone rocks. Induced seismicity caused by the gas extraction has become a growing problem for more than 20 years. The first induced earthquake associated to gas production was registered in 1986. After this event, the earthquake detection network in the north of the Netherlands was refined and further extended by the KNMI.

The growing seismic activity is shown in Figure 3.5, where a cumulative number of events per year with magnitude greater than 1.5 is depicted [19]. The relatively small magnitudes of these seismic events, their occurrence near producing gas fields in an originally aseismic region, as well as their shallow hypocentres, indicate that most of these earthquakes are in fact induced [56]. Typically, the hypocentre of these induced earthquakes is at a depth of -800 m to -3500 m, which is shallow compared to hypocentres of tectonic seismicity.

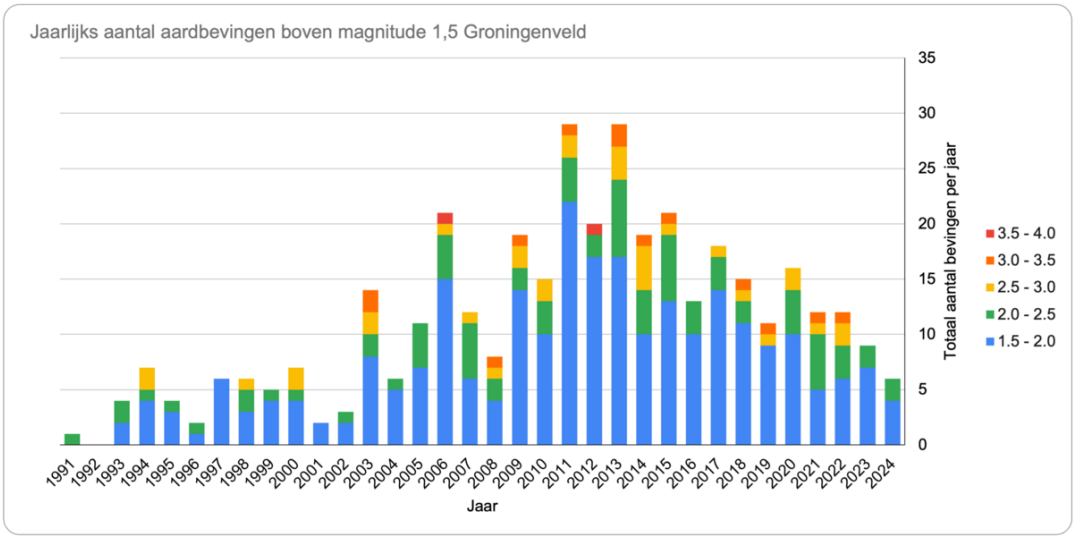

Figure 3.5: Activity rate of observed induced earthquakes in Groningen over the years. Only events with a magnitude greater than 1.5 are included, as depicted by Spetzler and Dost [19]

Apart from the magnitude of an earthquake to indicate the size of an earthquake it is not the only factor to indicate the effect of an earthquake on a building. The peak ground acceleration (PGA) is an important property to determine the forces acting on a structure due to an earthquake.

Usually, there are empirical relations used for ground motion prediction equations or attenuation relations. Due to several factors, e.g. focal mechanism, site response, rupture process and uncertainties in the 3D crustal structure, these relations show large variability. None of these attenuation relations are calibrated for small, shallow earthquakes, which are present in the Groningen area. These small-magnitude, shallow-source, induced earthquakes are able to cause large PGAs, mainly due to their shallow hypocentre. The energy released by the earthquake is close to earth's surface, which implies there is a smaller distance it has to travel, hence, less energy dispersion [57]. As a response to the nonexistence of an adequate ground motion prediction equation (GMPE), the KNMI proposed one based on a model for Europe and the Middle East [58] and modified according to the available Groningen data [59].

Using this GMPE a contour plot of the expected PGA can be constructed, which was done by Dost *et al.* [59]. The maximum value for the PGA in 2013 was found to be 0.42 g. This value has dropped to 0.36 g in 2015 and 0.24 g in 2017, see Figure 3.6. The physical upper limit to the magnitude of earthquakes that can be induced by gas production from the Groningen Field is estimated at $M = 6.5$. This limit is caused by the finite elastic energy or strain associated with reservoir compaction or the finite size of pre-existing faults. This could theoretically occur if all strain accumulated over the life cycle of the field were released in a single event at the very end of field life. The probability of such an event is essentially zero, but physically not impossible, therefore this is an absolute upper limit [60].

3.2 MODELLING OF SEISMIC LOADS

Earthquake loads act on a building in a single way, unlike other hazards, e.g. floods which produce static pressure and wave action. An earthquake produces only a dynamic acceleration of the building's base, the structure has a response to this action. Various methods are available to determine the response of a structure to a dynamic load, like an earthquake load. These methods will be addressed shortly, except the static push-over (PO) analysis, which will be discussed more in-depth, since it will be applied in this thesis. The main methods used for determining structural behaviour, as included in [61, NEN-EN 1998-1] are:

- A lateral force analysis is a static analysis where the seismic action is applied as a concentrated force at the centre of mass for each floor.
- A response spectrum analysis is a linear dynamic analysis where the seismic load is applied as a spec-

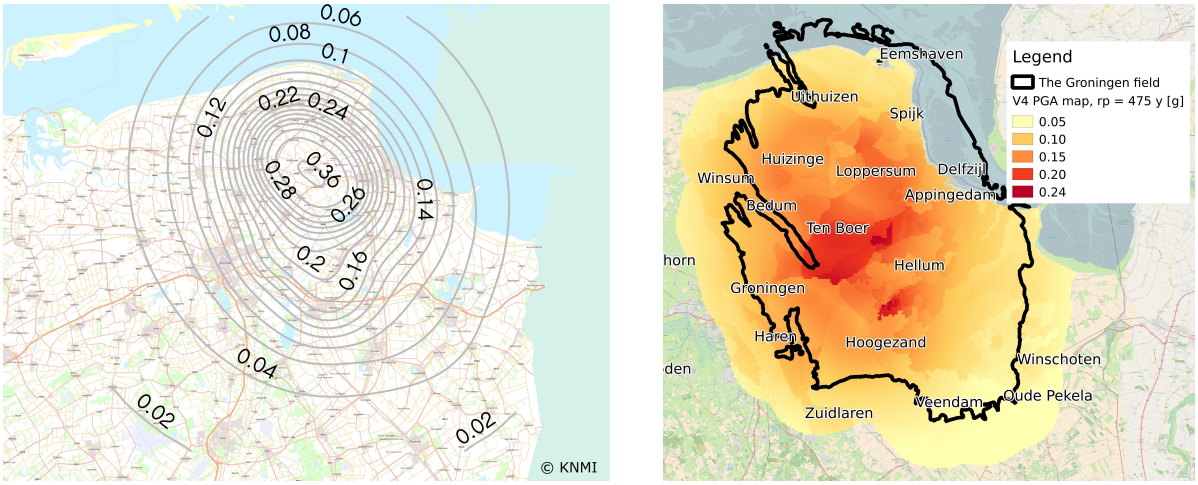

(a) Contour plot in 2015

(b) Contour plot in 2017

Figure 3.6: Contour plot peak ground acceleration with a return period of 475 years

trum, but the structures response is linear elastic.

- A pushover analysis is a nonlinear static analysis where the seismic action is applied statically, but nonlinearity of the structure's material is taken into account.
- A nonlinear time history analysis is a nonlinear dynamic analysis where the load is applied as an accelerogram, and nonlinearity of the structure's material is taken into account.

3.2.1 OVERVIEW MODELLING METHODS

In many cases it is convenient to perform a linear elastic analysis to get a first insight on the behaviour of a structure. The initial response of the structure, before any damage occurs, can be reasonably well modelled by such an analysis. This can yield locations in the structure where peak stresses will occur under a given load, which are places of interest for further analysis.

The lateral force analysis is a linear elastic analysis where the seismic load is applied as a concentrated force. The forces are applied at the centre of mass of each floor and are determined by the displacement of the mass in the fundamental mode shape. The most import condition to be able to use this method, according to [61, NEN-EN 1998-1], is a response governed by the first mode. Other requirements are bounds to the fundamental period of vibration. When these conditions are met a seismic base shear force F_b can be determined. This base shear force is distributed in horizontal seismic forces acting on the storeys of the structure. The fundamental mode shapes in the horizontal direction can either be determined using methods of structural dynamics or approximated by assuming a linear increase of the horizontal displacement along the height of the structure.

The response spectrum analysis can be applied when the criteria for a lateral force analysis are not met. With this method the peak responses of a linear elastic structure can be determined by response spectra representing the ground motions. In earthquake engineering it is particularly interesting to determine peak response quantities rather than the whole time history of the response for design purposes. To perform a response spectrum analysis a response spectrum is used as seismic input, generally an acceleration response spectrum is used. The response spectrum defines the maximum response quantity of a single degree of freedom (SDoF) system to a given ground motion. The response spectrum can be presented as a graph, where every point represents the maximum response of a SDOF system to a given input motion. The response spectra can either be taken from a source, e.g. Eurocode, or can be derived following structural dynamic principles [62].

Linear analyses can be very useful to get an insight in a structure's general behaviour. However, when

a more specific response of the structure is required a more advanced method of analysis should be used. Especially in the Groningen area, where damage to houses as a result of induced seismicity is the case, it is interesting to perform nonlinear analyses to incorporate the damage of the structures in the analysis and how this affects the response.

The most detailed of the named analysis methods is the Nonlinear Time History (NLTH) analysis. It allows an engineer to obtain the complete response history of a structure subject to earthquake loading. The obtainable time-dependent behaviour is very valuable, since it gives an extended insight in the structural behaviour, which makes it a suitable analysis method to study nonlinear effects.

The earthquakes acceleration signal is used in the NLTH analysis as an external force of the system. The signal is discretised into small time intervals, in each interval the new state of the system is calculated. Numerical integration is performed to satisfy the equations of motion. The state can be determined either by an explicit or implicit method, i.e. by information from the previous step only or information from the previous step and the current step combined. Additionally, the computation incorporates dynamic forces, hence, the results include dynamic amplification effects, e.g. resonance, damping effects as hysteresis and elastic material behaviour [63]. In many finite element software, an option is available to perform these kinds of analyses, e.g. in Diana the transient dynamic analysis is available for these problems.

3.2.2 ELABORATION ON PUSHOVER ANALYSIS

A pushover (PO) analysis is essentially very similar to the lateral force method. An eigenvalue analysis of the equivalent linear system is performed to determine eigenfrequencies ω_i and eigenmodes Φ_i. An eigenmode $\hat{\Phi}_i$ is chosen which is expected to contribute most to the structural response, in earthquake engineering usually the fundamental vibration mode is taken. With the chosen mode of vibration $\hat{\Phi}_i$, the structure is subjected to a monotonically increasing lateral force pattern compatible with this mode, as shown in Equation 3.1.

$$\hat{F}_i = \mathbf{M}\hat{\Phi}_i \tag{3.1}$$

Equation 3.1 provides the force vector $\hat{F}_i$ with the forces applied at each DoF "i", $\hat{\Phi}_i$ is the chosen eigenmode representing the dynamic behaviour of the system and $\mathbf{M}$ is the mass matrix associated with the structural system.

Assumptions and implications A linear system subject to uniform ground excitation can be described by the system of equations given in Equation 3.2. To be able to solve the system of equations an eigenvalue problem should be formulated. The eigenvalue problem yields the characteristic equation, which provides the eigenfrequencies and eigenmodes of the physical system.

$$\mathbf{M}\ddot{\mathbf{x}}(t) + \mathbf{C}\dot{\mathbf{x}}(t) + \mathbf{K}\mathbf{x}(t) = -\mathbf{M}\mathbf{r}\ddot{u}_g(t) \tag{3.2}$$

Using the solution of the eigenvalue problem, an eigenmatrix can be compiled from the eigenmodes. Together with the orthogonality property of the modes. the eigenmatrix can be used to obtain a system of uncoupled ordinary differential equations (ODEs), given in Equation 3.3.

$$\ddot{u}_i(t) + 2\zeta_i\omega_i\dot{u}_i(t) + \omega_i^2 u_i(t) = -\Gamma_i\ddot{u}_i \tag{3.3}$$

The solution of this uncoupled system of equations provides modal displacements, which can be converted to a displacement response in the real coordinate system by means of Equation 3.4.

$$\mathbf{x}(t) = \sum_{i=1}^{N} \hat{\Phi}_i u_i(t) = \Phi\mathbf{u}(t) \tag{3.4}$$

In a system where nonlinearity is included Equation 3.2 should be slightly adjusted. Since nonlinearity is rate-independent and concentrates in the stiffness term, the equation of motion (EoM) can be expressed as Equation 3.5.

$$\mathbf{M}\ddot{\mathbf{x}}(t) + \mathbf{C}\dot{\mathbf{x}}(t) + \mathbf{f}_s(\mathbf{x}, \text{sign}(\dot{\mathbf{x}}), t) = -\mathbf{M}\mathbf{r}\ddot{u}_g(t) \tag{3.5}$$

The response of the nonlinear system can be expressed as small oscillations around the original equilibrium position, which implies it is based on the vibration modes of the equivalent linear system. Interpreting the modes this way results in a final response where each mode of vibration is subject to contributions of all other modes. The coupling of the modes can be expressed by means of Equation 3.6.

$$\mathbf{x}_i(t) = \sum_{r=1}^{N} \hat{\Phi}_r u_r(t) \tag{3.6}$$

In a linear system this coupling of modes does not occur, since the response the response due to mode i is determined by consideration of mode i alone. In the nonlinear system the coupling of the modes is caused by the nonlinear stiffness matrix ($\mathbf{f}_s(\mathbf{x}, \text{sign}(\dot{\mathbf{x}}), t)$), since the chosen modes are based on the initial stiffness of the system. Furthermore, the dependence of the stiffness on position $\mathbf{x}(t)$, the sign of the velocity sign$\dot{\mathbf{x}}(t)$ and time t, makes the modes essentially time-dependent. Hence, it is questionable if a converged solution can be found using the modes of the original state of the system [62].

To simplify the problem an approximation of the nonlinear system can be made, which is only exact for linear systems. This approximation is based on the assumption that $u_r(t)$ equals zero for all modes $r \neq i$, as in the case of a linear system. With this assumption Equation 3.6 simplifies to:

$$\mathbf{x}_i(t) = \sum_{r=1}^{N} \hat{\Phi}_r u_r(t) \approx \hat{\Phi}_i u_i(t) \tag{3.7}$$

This approximation is only valid if the total response of the nonlinear system can be represented by the superposition of the response of each mode separately. The principle of superposition is generally not applicable to nonlinear systems. Therefore, this assumption is far from conservative and does not always reflect reality well. However, this weak coupling of the modes occasionally occurs in reality and assuming a converged solution of the nonlinear system is guaranteed for the chosen modes, an uncoupled set of EoMs can be formulated. The obtained set of EoMs is given in Equation 3.8.

$$\ddot{u}_i(t) + 2\zeta_i \omega_i \dot{u}_i(t) + \frac{F_{si}}{m^*_{ii}} = -\Gamma_i \ddot{u}_g(t) \tag{3.8}$$

Where:

Γ_i	=	The modal participation factor given by	L_i / m^*_{ii}; $L_i = \hat{\Phi}_i^\intercal \mathbf{M}\mathbf{r}$
m^*_{ii}	=	The modal mass given by	$\hat{\Phi}_i^\intercal \mathbf{M} \hat{\Phi}_i$
F_{si}	=	The modal stiffness per mode given by	$\hat{\Phi}_i^\intercal \mathbf{f}_s(u_i, \text{sign}(\dot{u}_i), t)$

This implicitly assumes a transformation of the nonlinear force-displacement relation to the modal domain which is known per vibration mode. The force-displacement can be found per vibration mode by means of a nonlinear static analysis. However, this method is not beneficial, since in the exact solution in the real coordinates the nonlinear stiffness term would couple all vibration modes. To overcome this shortcoming, another transformation of coordinates can be introduced, as given in Equation 3.9.

$$u_i = \Gamma_i D_i(t) \tag{3.9}$$

This transformation can be substituted in the EoM, given in Equation 3.8 to obtain $D_i(t)$ (Equation 3.10), and therefore the response of the nonlinear system.

$$\ddot{D}_i(t) + 2\zeta_i \omega_i \dot{D}_i(t) + \frac{F_{si}(D, \text{sign}(\dot{D}), t)}{L_i} = -\ddot{u}_g(t) \tag{3.10}$$

With Equation 3.7 and Equation 3.9 the total response can be found, given in Equation 3.12.

$$\mathbf{x}_i(t) = \hat{\Phi}_i \Gamma_i D_i(t) \tag{3.11}$$

$$\mathbf{x}(t) = \sum_{i=1}^{N} \mathbf{x}_i(t) = \sum_{i=1}^{N} \hat{\Phi}_i \Gamma_i D_i(t) \tag{3.12}$$

The approximation in Equation 3.11, as discussed above, assumes no involvement of other modes on the response of a given mode. Secondly, Equation 3.12 uses the principle of superposition, where vibration modes are superimposed, which is only applicable to linear systems. Furthermore, the dynamic response

cannot be scaled linearly when the nonlinear behaviour of the load acting on the system is considered, which is done by the participation factor Γ_i in Equation 3.11.

Apart from the clear shortcomings of the method, there are cases where it can be a useful method which gives a good estimate of seismic performance to a given seismic load. Especially in systems characterised by a predominant vibration pattern, i.e. simple systems vibrating at a single vibration mode, this can beneficial.

The modal pushover analysis is based on Equation 3.10 and obtaining a suitable plot of the F_{si}/L_i term. The seismic capacity of the system can be approximated once this is found. However, it is only applicable when the mode of vibration does not change in time and the spatial and time components of the nonlinear system can be separated, as in Equation 3.4. Thus, the method cannot be applied if a certain mode of vibration cannot be fixed and the mode of vibration Φ is time dependent, i.e. $\Phi \longrightarrow \Phi(t)$.

Additionally, when the response of the linear system is described by a large number of modes and the eigenfrequencies related to the system are close to each other, the modal pushover analysis is not expected to yield accurate predictions. There are three main reasons for the inaccuracy in this case [62]:

- The response cannot be found for each mode of vibration separately; therefore, predictions based on decoupling of the modes are inaccurate.
- The superposition of modes in a system where various modes contribute to the response of the system, is less accurate than in a system where two dominant vibration modes contribute.
- The assumption that modes do not change in time is not accurate. Modes do change in time; therefore, the separation of variables does not hold, and the modal set is a function of time and needs to be updated at every time moment.

Analysis procedure To obtain a solution of Equation 3.10, the nonlinear description of the term F_{si} (D, sign($\dot{D}$), t) must be known. Once this is known, the equation can be solved and D_i and then the total response can be found. There are two possibilities to obtain the nonlinear force-displacement pattern F_{si}, either a numerical computation of a pushover analysis or performing experiments. The execution of experiments is the most favourable method since it is more accurate than numerical computations.

The linear system is first considered to obtain the F_{si}/L_i–D_i plot per vibration mode. This is used as input of Equation 3.10, to determine the dynamic response $D_i(t)$. By means of Equation 3.11, this result can be transformed to the real coordinate $\mathbf{x}_i(t)$. However, only the peak response $\mathbf{x}_{i,max}$ is usually kept from the solution, since the PO curve is for one point only [62].

In an experimental setup of numerical computation of a PO analysis the lateral forces are distributed to the height with the load increased to push the structure until an ultimate displacement is reached. Information about the peak response in terms of floor displacement, storey drift or other deformation quantities can be obtained this way. A capacity curve should be obtained from the PO analysis, in this curve the displacement is plotted against the developed base shear. An example of a capacity curve, as depicted by Facconi *et al.* [20], is shown in Figure 3.7, including the difference between experimental- and numerical results [64].

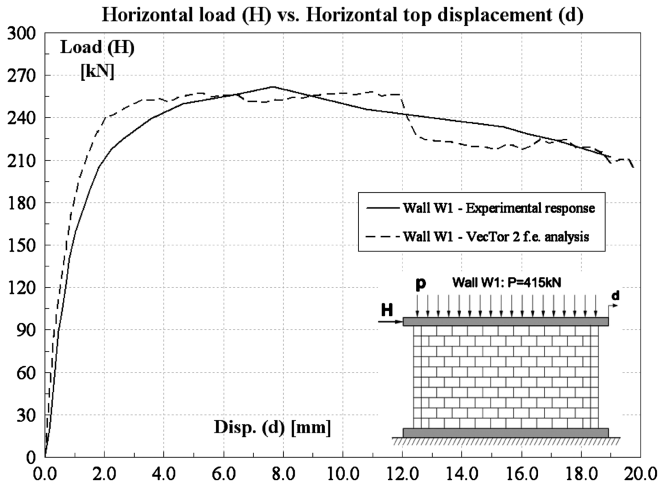

Figure 3.7: Experimental versus numerical capacity curve [20]

The loads can be applied in various ways, which leads to different results of the PO analysis. In a monotonic pushover analysis, the lateral load is increased monotonically until the lateral capacity of the structure is reached. The capacity of the structure also depends on the loading pattern, which can take various shapes, e.g. uniform, linear, or parabolic (Figure 3.8).

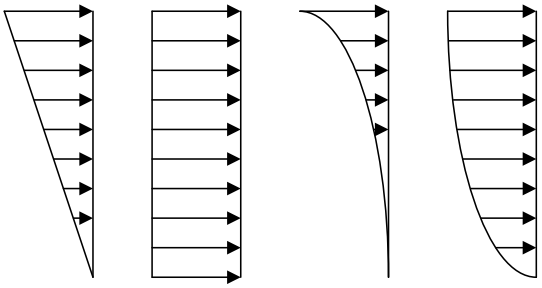

Figure 3.8: Various load patterns in pushover analysis

Another type of monotonic PO analysis is an adaptive analysis, the loading pattern reflects the deformation pattern of the structure at the end of each load step. In this case, the initial loading does not influence the capacity of the structure.

Thirdly, a cyclic pushover analysis, as performed on the TU Delft house, can be seen as a series of pushover analyses. The load changes to the opposite direction in every step of the analysis, the stiffness also changes for each load step to the stiffness at the end of the previous step. The result is a plot of various pushover analyses in the same figure, an equivalent viscous damping can be defined from the characteristic hysteretic loop, see Figure 3.9.

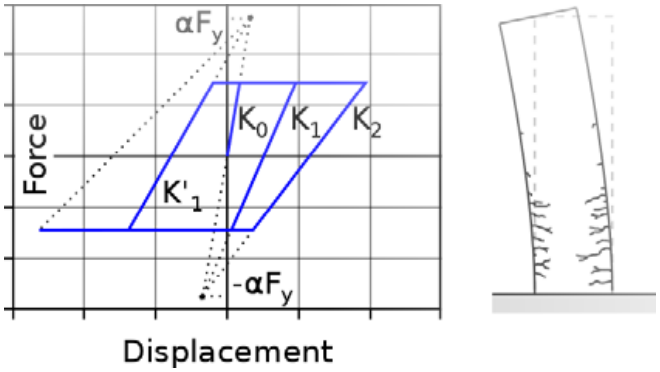

Figure 3.9: Cyclic load and stiffness degradation as depicted by Tsouvalas [21]

Regulations are mainly focused on monotonic pushover curves, e.g. in the Eurocode the PO analysis is performed by application of a constant gravity load and monotonically increasing horizontal loads [61, NEN-EN 1998-1]. Capacity is defined in terms of roof displacement in masonry buildings, where the ultimate displacement capacity is given by a total lateral resistance which drops below 80% of peak resistance. The decrease of lateral resistance (base shear) is caused by the accumulation of damage and subsequently failure of lateral load resisting elements.

These methods were initially developed considering rigid diaphragms, the application to unreinforced masonry buildings with flexible diaphragms is therefore questionable. Some studies show less reliability of the method when flexibility is considered [65]. The decrease of in plane stiffness of the diaphragms can cause the structural response to include more modes, which, as mentioned previously, causes less accurate results due to the assumptions associated with this method.

With all this in mind, the steps to perform a PO analysis can be summarised as follows [62]:

- Solving the eigenvalue problem of the equivalent linear system and obtain eigenfrequencies ω_i and eigenmodes Φ_i.
- Develop the $(V_{b,i} - x_{r,i})$ curve for vibration mode i, either numerically or experimentally, where the force is distributed following the mode shape, i.e. $\hat{s}_i = \mathbf{M}\hat{\Phi}_i$. The force can either be applied monoton-

ically or cyclic until collapse. Any other loads, e.g. live loads and gravity loads, can be applied prior to the lateral load.

- Obtain a $(F_{si}/L_i - D_i)$ curve from the $(V_{b,i} - x_{r,i})$ curve using $F_{si}/L_i = V_{b,i}/M_i^*$ and $D_i = u_{r,i}/(\Gamma_i \hat{\Phi}_{ri})$. The modes are normalised so $\hat{\Phi}_{ri} = 1.00$. The r in the previous expressions denotes the target point of the structure, while i denotes the considered vibration mode.
- Approximate the $(F_{si}/L_i - D_i)$ curve by bilinear relation using the approach of equal energies.
- Solving Equation 3.10 and obtain the peak deformation $D_{i,max}$.
- Use $D_{i,max}$ and transform to the real coordinates by applying $u_{r,i,max} = \Gamma_i \, \hat{\Phi}_{ri} \, D_{i,max} = \Gamma_i \, D_{i,max}$.
- Obtain the exact values of the response quantity of interest (r_{i+g}) from the original $(V_{b,i} - x_{r,i})$ curve, caused by the combined dynamic peak response $u_{r,i,max}$ and the static load $u_{r,g}$.
- Compute the dynamic response of mode i, using $r_i = r_{i+g} - r_g$. In this expression r_g is the ground load above.
- Perform these steps for all modes significantly contributing to the total response, determined in the first step.
- Combine the dynamic response of the significant modes by statistical combination rules, e.g. the absolute sum rule $r_d = \sum_{i=1}^{N} |r_i|$ or the square root of sum of squares rule $\left(\sum_{i=1}^{N} (r_i)^2\right)^{1/2}$.
- Determine the total seismic demand, with $r \approx \max\left(r_d \pm r_g\right)$

The previously describes procedure to determine the nonlinear response of a system is time consuming and in many practical cases not applicable. However, a modified version of this complex approach can be used in the seismic design of structures. To simplify the procedure, the peak response of a given mode is usually obtained from an earthquake design spectrum instead of being the solution to Equation 3.10. The use of this equation is often not possible, since $\ddot{u}_g$ is not provided in many practical cases and a solution to Equation 3.10 cannot be found. Furthermore, higher vibration modes are often neglected, implying a limitation of application to relatively simple structures. However, as mentioned previously, incorporating many modes is questionable, due to the validity of the principle of superposition in nonlinear systems [62].

CHAPTER 4

REFERENCE FINITE ELEMENT MODEL FOR THE BENCHMARK TEST

In this chapter a general description of the finite element model, adopted to reproduce numerically the benchmark pushover test conducted on a URM structure at TU Delft [1], is provided. In following chapters this model is used as a basis, any modifications are noted if applicable. A finite element model is only a tool to get a better understanding of what is happening in a structure, however, to be useful great consideration should be put in the way the model is set up. Ultimately, a finite element model is as good as the assumptions made to produce the model. The assumptions made are mainly based on the work done by Xu [2], to be able to make adequate comparisons.

The following model is based on the calcium silicate (CS) brick masonry assemblage with concrete floors as tested at Delft University of Technology [1], which is representative of a typical terraced house built between 1960 and 1980 in the Groningen area. The performed laboratory tests were designed to investigate the influence of the following building characteristics:

- Presence of slender piers, due to the presence of large openings in the facades.
- Presence of long transversal walls connected by a running bond to the facade.
- Limited connection between concrete and masonry.

The influence of other characteristics, such as soil structure interaction, cooperation between inner and outer leaf of cavity walls and the presence of spandrels were not addressed in the test, to reduce complexity of the performed quasi-static pushover test and computational burden in numerical analyses. The influence of the presence of spandrels, however, will be investigated in chapter 5.

This chapter will consist of three sections that cover respectively the overall geometry, the finite element discretisation and model properties, e.g. material models and material characteristics.

4.1 OVERALL GEOMETRY

The assembled structure as tested in the laboratory was designed to represent the load-bearing parts of a typical Dutch terraced house. A 3D view and front view of this laboratory setup is shown in Figure 4.1.

The geometry of the house, without the steel frame, consists of two continuous masonry walls, four masonry piers and two concrete floors. The two continuous load-bearing transverse walls have a length of 5.2 meters in global $y-$direction, they represent the walls separating two terraced houses. The walls respectively on the east and west of the assemblage are identical, see Figure 4.2. The same figure shows the south side of the assembled structure, which is identical to the north side, which consists of two masonry piers. The piers, which run in global $x-$direction, connect to the transverse walls by means of a running bond. The piers connecting to the transverse wall on the west side have a length of 1.1m, the piers on the east side have a length

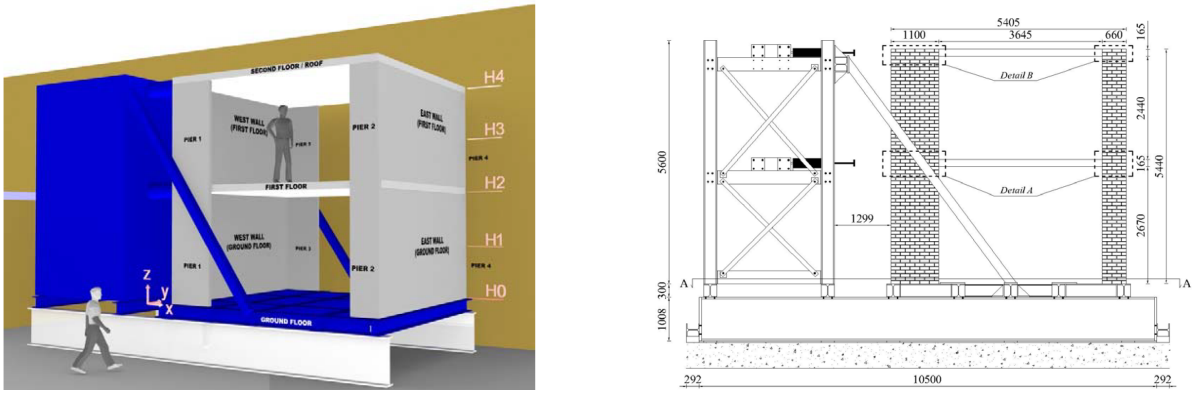

(a) 3D view (b) Front view

Figure 4.1: Overview of assembled structure as depicted by Ravenshorst *et al.* [1]

of 0.6m. The first floor is at a height of 2.7m, the second-floor level is at a height of 5.3m, which is the total height of the structure.

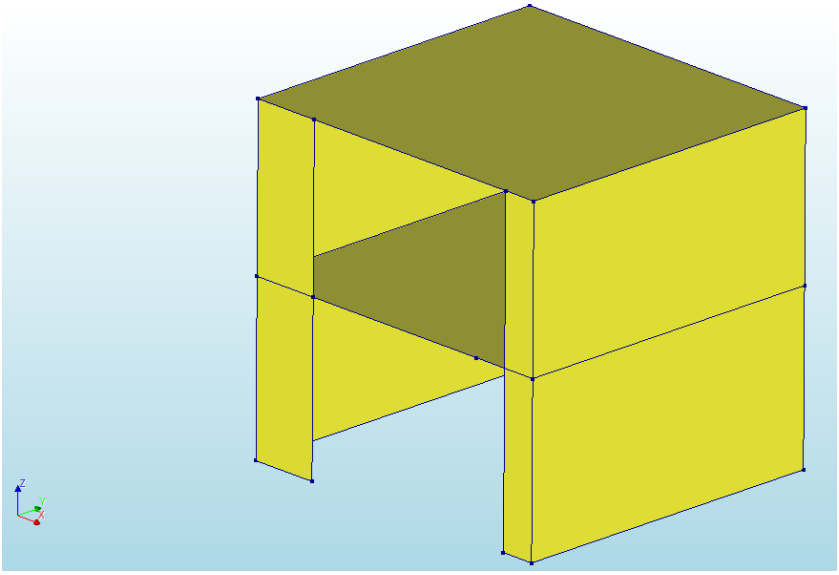

Figure 4.2: 3D view of the test setup recreated in DIANA

From Figure 4.2 it is clear that there are some key differences between the setup of the DIANA model and the test setup. The blue steel structure from 4.1a is not present in Figure 4.2. Since the first layer of masonry was glued to the steel frame to prevent it from being the governing connection, the bottom can be modelled as a fixed boundary condition. Note that a steel frame will be added in chapter 5 to provide an equal load at both floor levels during the PO analyses. A less visible difference can be found in some of the dimensions of the structure, they have been rounded up or down to decrease complexity.

4.1.1 CONNECTIONS

The model had to take the behaviour of the real structure into account as realistically as possible. Two contributors to this behaviour are the wall-to-wall connections and the floor-to-wall connections, and particularly the extent to which they are connected.

WALL CONNECTIONS

The transverse walls and piers were connected by a running bond in the laboratory setup. In this type of bond there is not a single mortar joint between the two masonry walls, the bricks of both walls alternate, see

Figure 4.3. The alternating way to stack the bricks causes interlocking between the two walls, the connection therefore can be seen as a solid connection. In the finite element model this means it is not necessary to use a type of interface elements between the two walls, the use of shared nodes is applicable in this case.

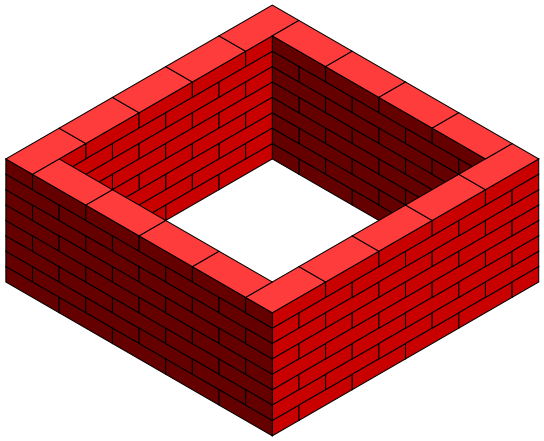

Figure 4.3: Isometric view of connection with running bond

FLOOR CONNECTIONS

The connection of the first floor and second floor should be viewed separately since both concrete floors make use of a different connection detail. The connection details as used in the laboratory test [1] will be described as well as how these connections are implemented in the finite element model.

First floor The concrete floor is connected to both the continuous transverse walls as to the piers. In 4.4a the connection detail between the first floor and the transverse walls is shown. The floor is placed on top of the load-bearing walls and connected by means of a mortar joint. The wall continues above the floor, again connected with a mortar joint. The floor could be considered as a part of the wall, the connection is relatively stiff. In the finite element model this behaviour is included by modelling it fully connected, again shared nodes are applicable.

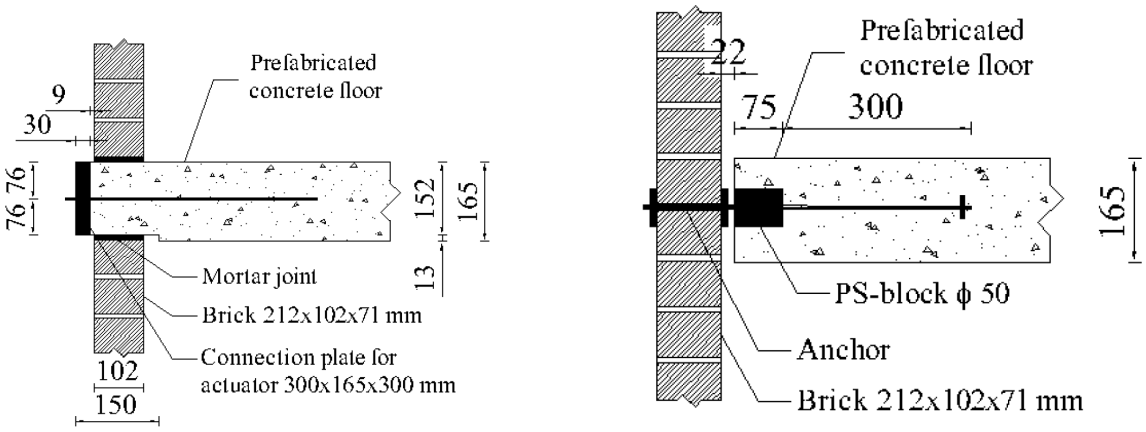

(a) Floor connection to transverse wall

(b) Floor connection to masonry pier

Figure 4.4: Construction detail of first floor connections as depicted by Ravenshorst *et al.* [1]

The connection of the first floor to the piers is different, see 4.4b. Anchors are used to connect the floor to the walls, the wide piers are connected by five anchors, the narrow piers are connected by three anchors. The anchors have a diameter of 6mm and are cast in the concrete and masoned in the piers. It is clear these anchors do not provide a full connection between the floor and piers. Their main purpose is to act as a shear

connector in the global $x-$direction. They cannot transfer loads in the direction perpendicular to the piers nor the vertical direction, in these directions the stiffness is negligible. In this case shared nodes are not applicable, and interface elements are applied to realistically include the properties of the anchors.

Second floor At the second-floor level, the concrete floor is first connected to the masonry transverse wall by means of a mortar joint, see 4.5a. The floor is directly placed on top of the load-bearing wall, which results in a relatively stiff connection, therefore shared nodes are used for this connection.

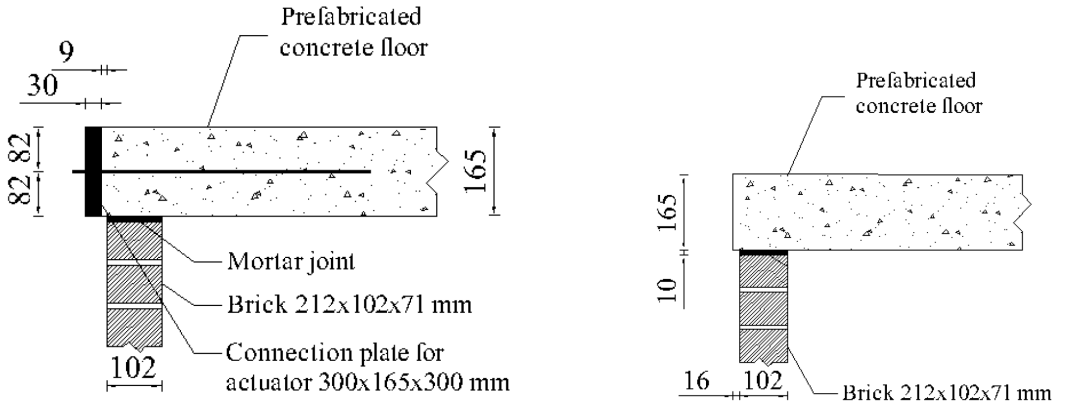

(a) Floor connection to transverse wall

(b) Floor connection to masonry pier

Figure 4.5: Construction detail of second-floor connections as depicted by Ravenshorst *et al.* [1]

The connection between the second floor and the piers is similar to that between the second floor and the transverse walls. However, the mortar joint between the floor and piers is filled after the mortar joint of the transverse wall has dried. As a result, the piers do not initially function as load-bearing walls. When lateral loads are applied, the connection begins to work in compression. To simulate this behaviour, shared nodes are used between the floor and piers in the model, allowing the piers to act as load-bearing walls. While this is a simplification of real conditions, it eliminates the need for a phased analysis.

4.1.2 SYMMETRY

Symmetry is of great importance when configuring a finite element model to reduce computational cost of the simulations. Especially in case of NLTH analyses which are very computationally heavy, it is preferred to make use of symmetry. The use of symmetry reduces the complexity of the finite element model by essentially halving the number of elements and nodes, and therefore the number of required calculations.

In Figure 4.2 an isometric view of the test setup recreated in DIANA is show, Figure 4.6 shows the same mode where symmetry is used. Since the global $x-$direction is less stiff than the global $y-$direction due to the large openings in the facade, this is the governing direction. All tests are performed with a loading in global $x-$direction, therefore symmetry in global $y-$direction can be applied.

In Figure 4.6 the red cones across the plane of symmetry, indicate a boundary condition. These boundary conditions restrict the displacement in $y-$direction along this plane. Since there is only loading in $x-$direction and the model is symmetrical, no displacements in $y-$direction should occur at this plane of symmetry.

The following chapters will slightly alter the geometry of this model but are all based on the reduced model to improve calculation time.

4.2 FINITE ELEMENT DISCRETISATION

The finite element model can be further simplified to reduce computational complexity. Since the dimensions of the walls, i.e. length and height, are relatively large compared to the thickness the need to use full 3D elements is not necessary. The same applies to the floors, which length and width are relatively large compared to their height. This allows to make use of 2D elements, which reduces the number of nodes per element and therefore the computational burden.

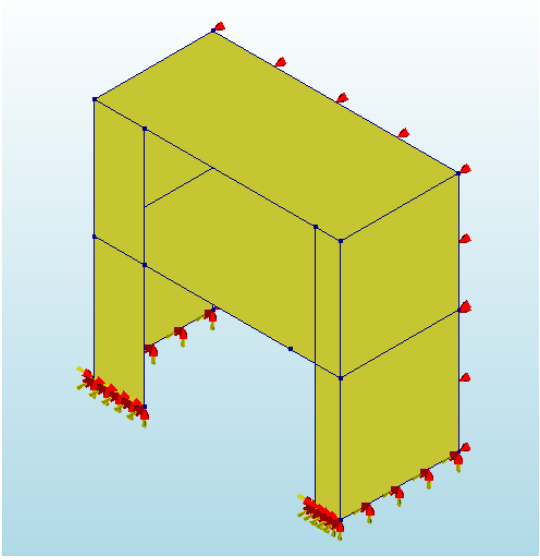

Figure 4.6: Finite element model with symmetry applied

4.2.1 TYPE OF ELEMENTS

Both the masonry walls and concrete floors are modelled with two-dimensional elements, i.e. curved shell elements, see Figure 4.7. These elements are applicable to describe both in-plane and out-of-plane deformations. Furthermore, curved shells are usable in combination with the engineering masonry model, which will be discussed in section 4.3. Two shell hypotheses are introduced to base the curved shell elements on isoparametric degenerated-solid approach in DIANA [22], more specifically:

- Straight-normals – the normals remain straight, but not necessarily normal to the reference surface. The Mindlin-Reissner theory is applied to account for transverse shear deformation.
- Zero-normal-stress – the normal stress component in the normal direction of a lamina basis is forced to zero: $\sigma_{zz_{l(\xi,\eta,z)}} = 0$. The element tangent plane is spanned by a lamina basis which corresponds to a local Cartesian coordinate system (x_1, y_l) defined at each point of the shell with x_1 and y_l tangent to the ξ,η plane and z_1 perpendicular to it.

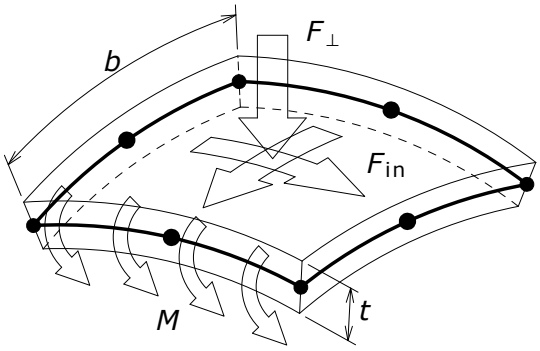

Figure 4.7: Characteristics of a curved shell as depicted by Manie and Kikstra [22]

The in-plane lamina strains ($\epsilon_{xx}, \epsilon_{yy} and \gamma_{xy}$) vary linearly over the thickness of the element, in contrast to the transverse shear strains ($\gamma_{xz} and \gamma_{yz}$), which are forced to be constant. In reality, the transverse shear strains and stresses vary parabolically over the thickness of the element. To account for this, a shear correction factor is applied, to ensure a constant transverse shear stress yields approximately the same shear strain energy as the actual shear stress.

The type of curved shell element used in the DIANA model is an eight-node quadrilateral isoparametric curved shell element (CQ40S), see Figure 4.8. The element uses quadratic shape functions for interpolation

and Gauss integration over the $\xi\eta$ element area. A reduced 2×2 integration scheme is used to prevent membrane and shear locking. Integration over the thickness of the element (ζ) may be Gauss or Simpson, by default a three-point Simpson integration scheme is used, however, a seven-point integration scheme is used over the thickness to better show out of plane deformations and cracks in the transverse walls.

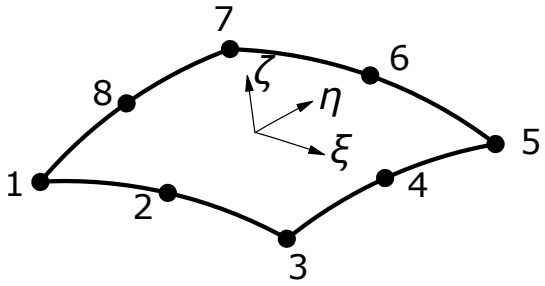

Figure 4.8: CQ40S element as depicted by Manie and Kikstra [22]

The polynomials to describe the translations and rotations can be expressed as shown in Equation 4.1. In a rectangular element, these equations typically yield the following stress and strain distribution along the element area in a ζ lamina. The strain, curvature, moment, membrane force and shear force, respectively ϵ_{xx}, κ_{xx}, m_{xx}, n_{xx} and q_{xz} vary linearly in $x-$direction and quadratically in $y-$direction. Similarly, ϵ_{yy}, κ_{yy}, m_{yy}, n_{yy} and q_{yz} vary linearly in $y-$direction and quadratically in $x-$direction.

$$\begin{aligned} u_i(\xi,\eta) &= a_0 + a_1\xi + a_2\eta + a_3\xi\eta + a_4\xi^2 + a_5\eta^2 + a_6\xi^2\eta + a_7\xi\eta^2 \\ \o_i(\xi,\eta) &= b_0 + b_1\xi + b_2\eta + b_3\xi\eta + b_4\xi^2 + b_5\eta^2 + b_6\xi^2\eta + b_7\xi\eta^2 \end{aligned} \tag{4.1}$$

The mesh of the half house model is shown in Figure 4.9, a mesh size of 100mm is used in this figure. The mesh size used for the PO analyses in chapter 5, will be coarser to reduce computational time.

The first-floor connection to the piers is indicated by the red line, since this is the only connection that uses interface elements to properly model the connection. Since the masonry model includes the anisotropic behaviour of masonry, special attention is required during the setup of the model. The material properties are not equal in all directions, therefore the local coordinate system of the two transverse walls differ from the local coordinate system of the piers, see Figure 4.9. In both cases the local $x-$axis coincides with the bed joint of the masonry, the local $y-$axis is the in-plane direction perpendicular to the bed joint and the local $z-$axis is the out-of-plane direction. The local coordinate systems of both concrete floors coincide with the global coordinate system. The same integration scheme is used for the floors as for the walls. The main difference between the elements used in the walls and the floors is their thickness, i.e. 102mm for the walls and 165mm for the floors.

4.2.2 CONNECTION INTERFACES

As previously described, there are four individual connection details present in the test setup. These can be divided in two groups:

- Rigid connections - where the two elements of the structure are modelled with shared nodes, present at all connections on the second-floor level as well as the connection from the first floor to the transverse wall.
- Shear connection - no vertical load or out-of-plane load is transferred, present on the first-floor level in the connection to the piers (red lines in Figure 4.9).

The first connection is automatically generated in DIANA by merging nodes at the same position after meshing. The latter is modelled by the addition of interface elements between floor and piers. These interface elements are 3D line interface elements (CL24I), the elements consist of six nodes and are used between two lines in a curved shell configuration.

Like the shell elements it connects, the interface element is based on quadratic interpolation, see Figure 4.10. The same order of interpolation polynomial is necessary to prevent incompatibility, e.g. gaps could

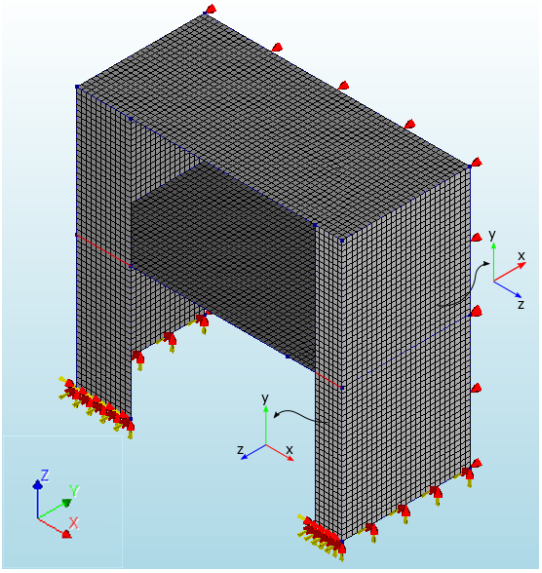

Figure 4.9: Mesh of the half house model

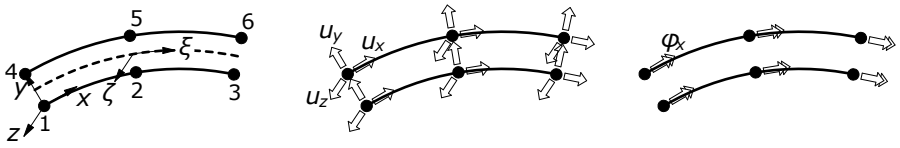

Figure 4.10: CL24I element as depicted by Manie and Kikstra [22]

form between elements if the elements are not of the same order. By default, a 3-point Newton-Cotes integration scheme in the longitudinal (ξ) direction and a 3-point Simpson integration scheme in the thickness (ζ) direction is applied by DIANA. The thickness of these elements corresponds to the thickness of the elements in the concrete floor, i.e. 165mm.

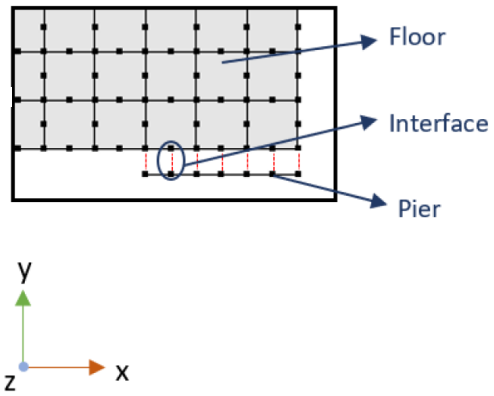

Figure 4.11: Visual representation of interface elements as depicted by Xu [2]

In Figure 4.11 a schematic representation of the interface elements is shown. One row of nodes is connected to the nodes of the floor, the other row of nodes is connected to the nodes of the piers. In the real model, however, there is no gap present between the nodes of the floor and the nodes of the pier, they share their coordinates, but the same principle still applies.

As previously mentioned, the anchors will act as shear connectors, in the global $x-$direction, between the floor and the piers. No force transfer in $y-$ and $z-$direction will occur. To enforce this behaviour the 3D line interface elements will only have a stiffness in $x-$direction, both other directions are given a stiffness of zero.

4.3 CONSTITUTIVE MODELS AND MATERIAL PROPERTIES

The model consists of two materials, i.e. masonry for the walls and concrete for the floors. However, three material properties are used, since the interface between the first floor the piers cannot be modelled with shared nodes separate interface elements are introduced to properly model this connection. These three models are discussed in this section.

4.3.1 ENGINEERING MASONRY MODEL

To accurately model the masonry behaviour, the Engineering Masonry model is adopted. The model can be applied combined with regular plane stress or curved shell elements to model failure of masonry walls and is a smeared failure model. The energy absorption of masonry models subject to cyclic loading is underestimated in the Total Strain crack models, since they are based on secant unloading and reloading. The unloading behaviour is more realistic described by the Engineering Masonry model by strong stress decay with the original linear stiffness. Additionally, the model includes a shear failure mechanism based on the Coulomb friction criterion. According to the DIANA material library, the Engineering Masonry model is especially recommended for static nonlinear cyclic or transient dynamic nonlinear analyses of components and full structure [23].

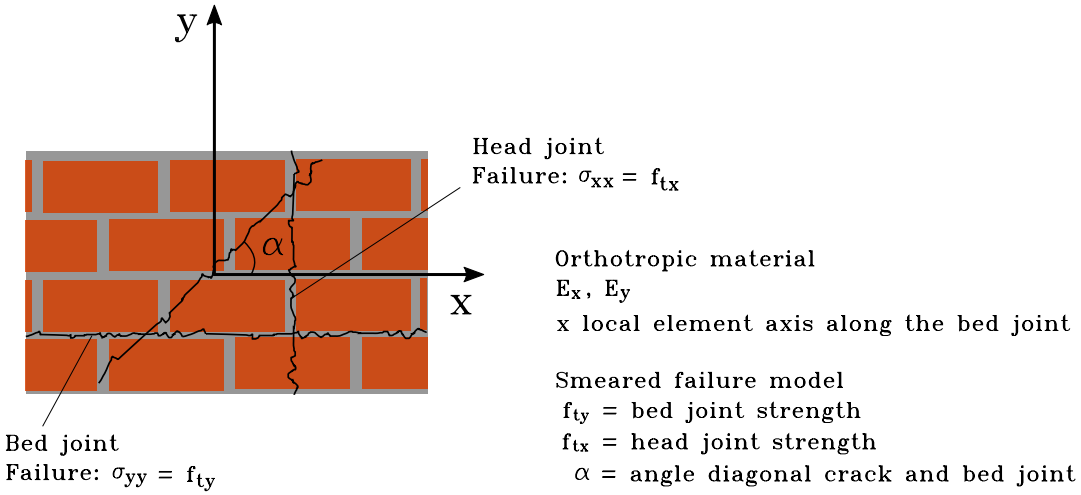

Figure 4.12: Engineering Masonry model characteristics as depicted by Manie and Kikstra [23]

The Engineering masonry model, see Figure 4.12, is defined by the following characteristics:

- To consider the anisotropy of the masonry a different stiffness in the direction of the bed joint and head joint is applied. As shown in Figure 4.9, the element $x-$direction coincides with the bed joint and is normal to the head joint, which aligns with the element $y-$direction.
- In the plane of the element four predefined cracks are present, in the local $x-$direction, in the local $y-$direction and two in the direction of predefined angle.
- The model assumes no coupling between the stiffness of the normal components in the $x-$ and $y-$direction and that of the in-plane shear component when the diagonal cracks are not active or not checked. The Engineering Masonry model (EMM), therefore, behaves like an orthotropic material with a Poisson ration set to zero.
- Seven individual failure mechanism are considered:
  - Tensile cracking of either the head or the bed joint
  - Compressive crushing either in the direction of the bed joint or the head joint
  - Cracking in the direction normal to diagonal stair step cracks
  - Frictional shear sliding

  - Out-of-plane shear failure

- Secant nonlinear unloading and reloading behaviour is assumed for tensile cracking (similar to the Total Strain Crack model), which is assessed in either the direction normal to the head joint or the bed joint.
- In contrast, nonlinear non-secant unloading and reloading is considered for compressive crushing, the directions coincide with those of tensile cracking.
- Diagonal cracks are assessed in the directions normal to the diagonal stair step cracks, at a predefined angle. The tensile stress normal to the diagonal crack and the shear stress in the diagonal plane are reduced when one of the diagonal cracks is active and the crack is opening. A linear stiffness equal to the initial elastic stiffness is applied when the crack is closing.
- Based on the stress in the direction normal to the bed joint, shear stresses are limited by a standard Coulomb friction failure criterion.
- Out-of-plane shear stiffness components are assumed to be linear elastic in shell elements, when the out-of-plane shear failure option is not chosen. If that option is selected, the out-of-plane shear stress in the bedding plane is checked with the Coulomb friction criterion.

CRACKING

The stresses in the element $x-$ and $y-$direction are defined by the respective strain components ε_x and ε_y and the maximum stress that has ever been reached, see Figure 4.13.

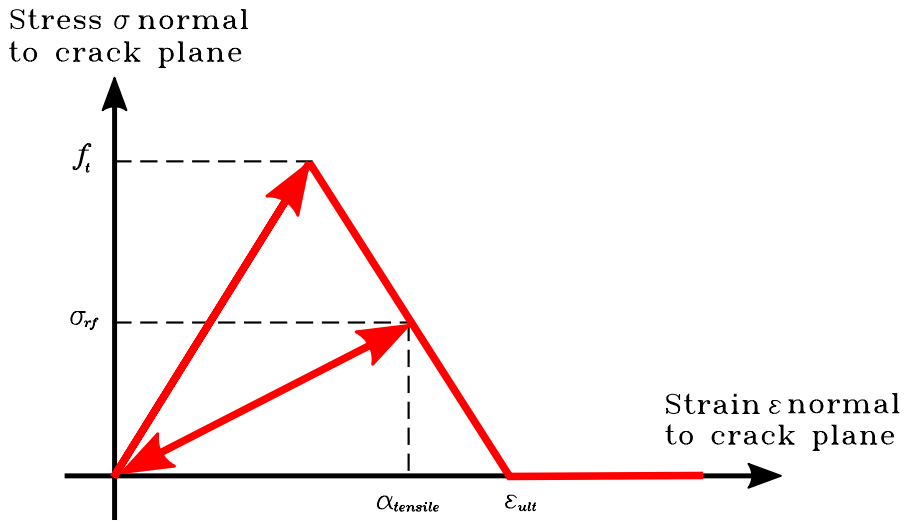

Figure 4.13: Cracking behaviour of Engineering masonry model as depicted by Manie and Kikstra [23]

In this figure $\alpha_{tensile}$ represents the maximum tensile strain ever reached, the corresponding stress is given by σ_{rf}. The tensile stress-strain curve for both $x-$ and $y-$direction are defined by the Young's modulus E, the tensile crack energy G_{ft} and the tensile strength F_t. The softening is assumed to be linear, and the ultimate strain ε_{ult} is defined as the strain where the crack is fully open and cannot transfer any stresses.

$$\varepsilon_{ult} = \frac{2G_{ft}}{hf_t} \tag{4.2}$$

Where h is the crack bandwidth of the element, which can be calculated from the area over which the crack is smeared ($h = \sqrt{A}$, where A is the area of the element). Secant unloading and reloading is applied, i.e. a straight line to the origin is followed. In Figure 4.13 the stress-strain diagram of the EMM is only shown in the tensile regime ($\varepsilon > 0$). If a new strain extreme is reached ($\varepsilon > \alpha_{tensile}$) the new $\alpha_{tensile}$ is equal to ε. The corresponding stress σ is:

$$\sigma = \begin{cases} \varepsilon E & \text{for } 0 \leq \varepsilon < \frac{f_t}{E} \\ \frac{E(\varepsilon_{ult}-\varepsilon)}{E\varepsilon_{ult}-f_t} f_t & \text{for } \frac{f_t}{E} \leq \varepsilon < \varepsilon_{ult} \\ 0 & \text{for } \varepsilon_{ult} \leq \varepsilon \end{cases} \tag{4.3}$$

At the maximum tensile strain ever reached $\alpha_{tensile}$, the corresponding stress σ_{rf} is:

$$\sigma_{rf} = \sigma \tag{4.4}$$

However, at a strain lower than the maximum strain ever reached ($\varepsilon < \alpha_{tensile}$), i.e. tensile unloading or reloading. Stress is calculated by:

$$\sigma = \frac{\varepsilon}{\alpha_{tensile}} \sigma_{rf} \tag{4.5}$$

The tensile strength f_{ta}, when checking in diagonally stair step cracks is activated is calculated by:

$$f_{ta} = \frac{f_{tx} f_{ty}}{f_{tx}^2 \sin^2(\frac{\pi}{2} - \alpha) + f_{ty}^2 \cos^2(\frac{\pi}{2} - \alpha} \tag{4.6}$$

Where the user defined bed joint tensile strength is represented by f_{ty} and the user defined head joint tensile strength is represented by f_{tx}, which is defined as:

$$f_{tx} = \frac{\tau_{max}}{\tan(\alpha)} \tag{4.7}$$

Where α represents the user defined angle between the bed joint and the direction of the diagonal stair step cracks. The expected orientation of the cracks, based on size and pattern of the bricks, should lead to how α is defined. In Equation 4.7, τ_{max} represents the maximum frictional shear stress, defined by:

$$\tau_{max} = \max \begin{cases} 0 \\ c - \sigma_{yy} \tan(\phi) \end{cases} \tag{4.8}$$

where c is the cohesion and ϕ the friction angle.

CRUSHING

The compressive fracture energy G_{fc}, compressive strength f_c, Young's modulus E and a factor n mainly describe the masonry compressive behaviour in the Engineering Masonry model. The latter considers the deformation capacity of the masonry beyond the elastic limit, and is defined by:

$$n = \frac{E\varepsilon_{peak}}{f_c} \tag{4.9}$$

where ε_{peak} corresponds to the masonry strain at the compressive strength f_c.

The compressive stress-strain relation applied along the local $x-$ and $y-$axis is the same. The compressive curve consists of a third and second order polynomial up to the compressive strength, then up to a residual stress of 10% of the compressive strength a linear softening is assumed, see Figure 4.14.The strain where the extended linear softening curve would reach a stress of zero is defined as the ultimate compressive strain ε_{ult}. The value of the ultimate compressive strain can be derived from the compressive fracture energy G_{fc} and the crack bandwidth h [66].

A bilinear unloading relation is adopted in the engineering masonry model. Unloading with the initial stiffness E is used up to the point where secant unloading is adopted. This point is determined by an unloading factor λ ($0 \leq \lambda \leq$), where $\lambda = 0$ corresponds to unloading with the initial stiffness and $\lambda = 1$ to secant unloading to the origin with stiffness $\sigma_{rf}/\alpha_{comp}$. The initial stiffness for unloading is applied until a compressive stress of $\lambda\sigma_{rf}$ is reached, then a secant stiffness to the origin is followed:

$$E_{secant} = \frac{\lambda\sigma_{rf}}{\alpha_{comp} - \lambda\frac{\sigma_{rf}}{E}} \tag{4.10}$$

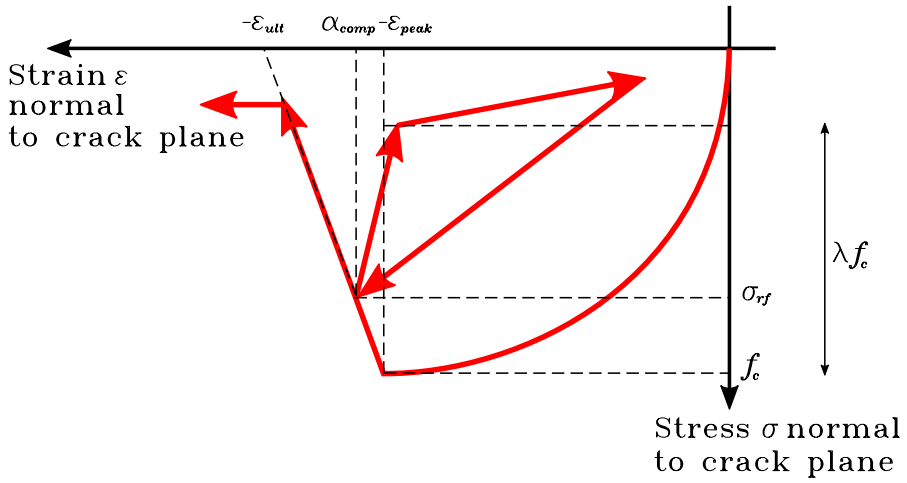

Figure 4.14: Crushing behaviour of Engineering masonry model as depicted by Manie and Kikstra [23]

The stiffness at reloading is determined by the last loading extreme points $(\alpha_{comp}, \sigma_{rf})$. A straight line to this last loading extreme is followed. The energy dissipation of masonry under cyclic loading can be modelled properly using these assumptions.

SHEARING

The in-plane shear stress τ is defined by the stress normal to the bed joint σ_{yy} and the in-plane shear strain γ. The shear stress is limited by the maximum friction stress τ_{max}, defined in Equation 4.8. This is a standard Coulomb friction criterion, where c is the cohesion, ϕ the friction angle and G is the initial shear stiffness.

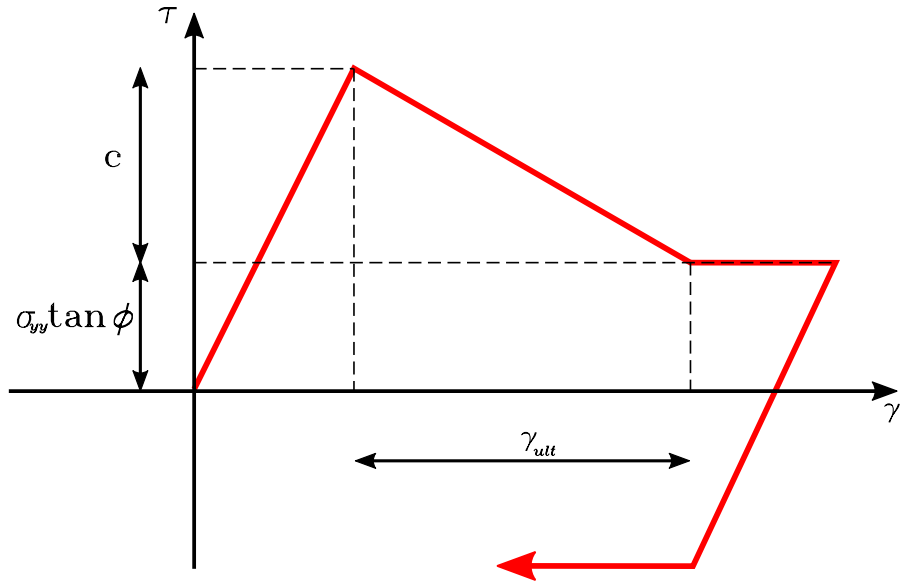

Figure 4.15: Shearing behaviour of Engineering masonry model as depicted by Manie and Kikstra [23]

4.3.2 MASONRY MODEL PROPERTIES

As the model is based on the calibrated model described by Xu [2], the material properties are chosen accordingly. The values of the material properties as entered in the finite element model are summarized in Table 4.1. Some parameters are obtained from material tests conducted on components, i.e. Young's modulus in both $x-$ and $y-$ direction E_x, E_y, compressive strength f_c and shear properties ϕ, f_{v0}. Other values are derived from equation found in literature.

4.3.3 CONCRETE MODEL PROPERTIES

To focus on the behaviour of the masonry walls when subject to seismic loading, the concrete floors are assumed to behave linear elastically. The reinforced concrete slabs used in the experiments ware of strength class C53/65. A wet concrete joint was used to connect the slabs in-situ. The values of the material properties as entered in the finite element model are summarized in Table 4.1.

4.3.4 INTERFACE MODEL PROPERTIES

The connection between the concrete first floor and masonry piers was previously discussed in section 4.2. To simulate the shear connection 3D line interface elements are applied. These elements solely incorporate linear material properties, i.e. normal stiffness in $y-$direction and shear stiffness in both $x-$ and $z-$direction.

Since there is only force transfer in global $y-$direction, due to the used shear connectors between the masonry piers and concrete floor, only a stiffness in this direction should be applied. Therefore, stiffness in both $x-$ and $z-$direction are equal to zero. To estimate the shear stiffness of the interface elements the following equation is used:

$$E_{n,y} = \frac{100E}{l_{adj}} \tag{4.11}$$

where the interface element normal stiffness is represented by $E_{n,y}$, E and l_{adj} are respectively the stiffness and the length of the elements adjacent to the interface.

The stiffness of masonry is significantly lower that the stiffness of concrete, therefore the masonry stiffness is used to estimate the interface stiffness. In Table 4.1 the stiffness of masonry is given (E_y = 3264 MPa), the length of adjacent elements is 200mm, which results in a stiffness of $E_{n,y}$ = 1632 MPa according to Equation 4.11. The stiffness is shown in Table 4.1, together with the other material properties.

Material	Property	Parameter			Unit	Value
Masonry	Elasticity	Young's modulus	Perpendicular to head joints	E_x	MPa	2212
			Perpendicular to bed joints	E_y	MPa	3264
		Shear modulus		G_{xy}	MPa	1306
		Mass density		ρ	kg/m^3	1805
	Cracking	Tensile strength	Normal to bed joint	f_{ty}	MPa	0.19
		Tensile fracture energy		G_{ft}	N/mm	0.0127
		Angle between stepped diagonal crack and bed joint		θ	rad	0.792
	Crushing	Compressive strength		f_c	MPa	5.84
		Compressive fracture energy		G_{fc}	N/mm	17.39
		Factor to strain at compressive strength		n		5
		Unloading factor		λ		0
	Shearing	Friction angle		ϕ	rad	0.406
		Cohesion		f_{v0}	MPa	0.14
Concrete	Elasticity	Young's modulus		E_s	MPa	35500
		Poisson's ratio		ν		0.2
		Mass density		ρ	kg/m^3	2400
Interface	Elasticity	Normal stiffness		$E_{n,y}$	MPa	1632
		Shear stiffness		$E_{t,x}$	MPa	0
				$E_{t,z}$	MPa	0

Table 4.1: Material properties used in the Finite element model

II

Geometry Variation in Masonry Building

This part focusses on the finite element modelling of the full-scale CS brick masonry assemblage of the house tested at the TU Delft, which is representative for a terraced house built in the period between 1960 and 1980 in the Groningen area. Some modifications to the geometry are applied to obtain a more realistic view of crack propagation and failure mechanisms. A general setup of the finite element model was described in chapter 4, in chapter 5 variations on this calibrated model are made. The focus here is on nonlinear push over analyses conducted on the models with a variation in geometry, i.e. varying spandrel height. Results are shown per model and finally discussed and compared to each other.

CHAPTER 5

NONLINEAR PUSHOVER ANALYSES ON MASONRY BUILDINGS WITH VARIATION IN GEOMETRY

Multiple nonlinear pushover analyses were performed to investigate the influence of varying spandrel dimensions on the seismic response of the building. Three aspects are considered to determine the influence, i.e. capacity curves, crack evolution and interstorey drifts. The basics of the model are based on the calcium silicate (CS) brick masonry assemblage with concrete floors as tested at Delft University of Technology [1] and the model described by Xu [2] and were presented in chapter 4. Variations in geometry were applied and will be discussed in section 5.1. Then, in section 5.2 the settings used to perform the NLPO analyses are shown, as is the application of the pushover loads. In section 5.3 the resulting capacity curves, crack evolution and interstorey drifts of the various geometries are presented.

5.1 GEOMETRY VARIATIONS

To investigate the influence of spandrels to the seismic response of the building, some variations were made to the geometry. The first variation on the geometry compared to the model described in chapter 4 is the dimension of the small pier at the east side of the building. The width of that pier was made equal to the pier on the west side of the building, i.e. 1100 mm. This variation in geometry was applied to obtain a symmetrical model. The response to an earthquake load in a symmetrical model will be similar in both directions. A monotonic pushover analysis in only one direction (positive $x-$direction) will provide insight in the structural behaviour, without the computational burden of performing the analysis in both directions. This is favourable when multiple geometry variations will be compared to each other.

Multiple variations in the spandrel geometry are analysed. The first model uses a spandrel height of 81 mm, which is about half the floor thickness. It is used as a reference to the original finite element model. As illustrated in Figure 5.1, the height of the spandrel at second-floor level is defined as $h_{spandrel}$, the height of the spandrel at first floor level is defined as $2 * h_{spandrel}$.

Subsequent models were defined with a spandrel height of 200 mm, 300 mm, 400 mm, 500 mm, and 800 mm. These variations of the model are depicted in Figure 5.2. By increasing the spandrel height, the height of the openings is decreasing at the same time. The height of the opening in its turn is related to the effective height of the piers. If the piers are relatively slender (ratio l/h is small) the pier is expected to fail in a flexural or rocking fashion. In case the slenderness of the piers decreases (ratio l/h increases) the type of failure is expected to change to a shear failure of the piers. To investigate when and if this behaviour will occur, the model with a spandrel height of 800 mm was included. This model is arguably no longer a good representation of a

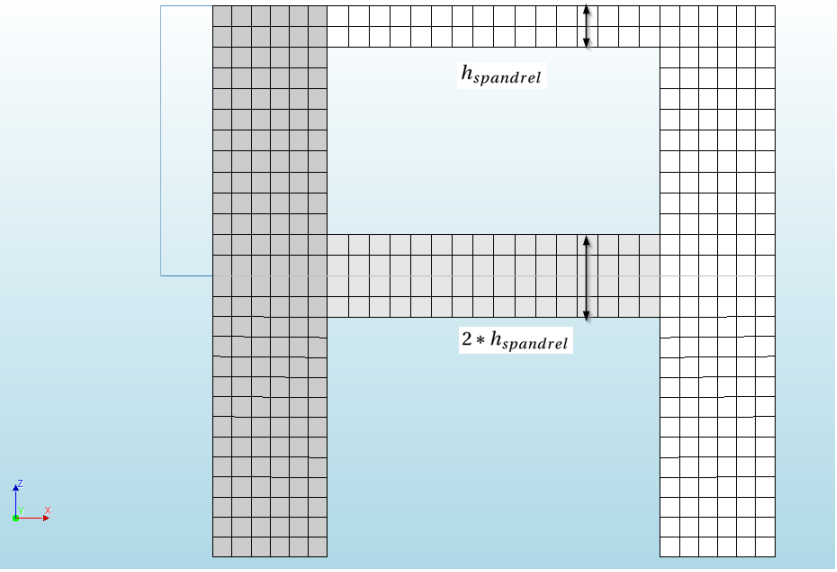

Figure 5.1: Definition of spandrel height at first- and second-floor level

typical Groningen terraced house, however the possible insight in a change of failure mechanism makes it a valuable addition to the analysed models.

The increase of spandrel height is expected to have some additional effects on the structure. It is expected to see an increase in the capacity of the structure as well as an increase of the stiffness of the structure.

5.2 SETUP NONLINEAR PUSHOVER ANALYSES

The general setup of the pushover analyses was chosen to be in line with the quasi-static pushover analysis on the calcium-silicate brick masonry assemblage described in Ravenshorst *et al.* [1] and the following finite element analyses performed by Xu [2]. In the laboratory tests on the full-scale assemblage, a steel frame (Figure 4.1) was used to apply the lateral load on the structure. In the finite element analyses a similar approach was applied to impose a prescribed displacement on the structure. The loading method is further explained in subsection 5.2.1.

5.2.1 PUSHOVER LOAD

The goal of the setup of the PO analysis is to obtain results that can be compared to the laboratory tests and previously performed finite element analyses. Therefore, displacement-controlled loading is applied to the structure, which also performs better with regard to convergence in the post-peak phase of the analyses. Taking into account the symmetrical building, only half of it is modelled, a single rigid vertical steel beam is added to the model which is connected at first- and second floor by a rigid steel truss element. The position of the steel beam is based on the location of the actuators in the experiment and the steel beam in the model derived from it.

By applying the load this way, the same force is applied on both floors, as was done in the experiment. The vertical steel beam is positioned 1100 mm inward from the façade. The load, a deformation load, is applied at midheight of the two floors. To apply this load a support is required in the direction of the prescribed deformation. Therefore, a support in x-direction is added, so a deformation in global x-direction can be applied. To make sure two equal forces are applied at both floors the support at the middle of the steel beam allows for rotation of the beam in the xz-plane. Displacement in z-direction is restricted in the point, as is rotation around its longitudinal axis to prevent torsion in the beam. Furthermore, displacement in y-direction at both ends of the beam is restricted to prevent rotation in the yz-plane, see Figure 5.3.

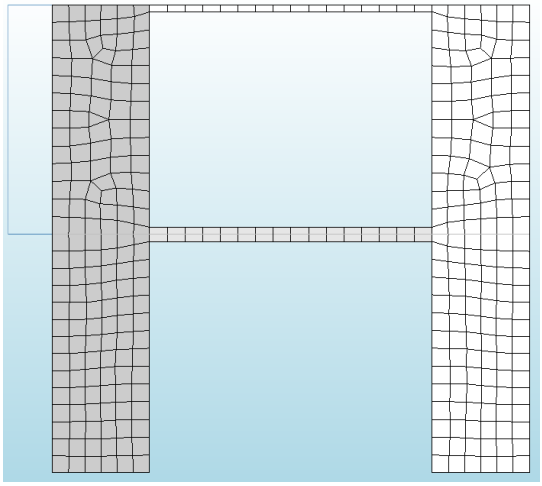

(a) $h_{spandrel}$ = 81mm

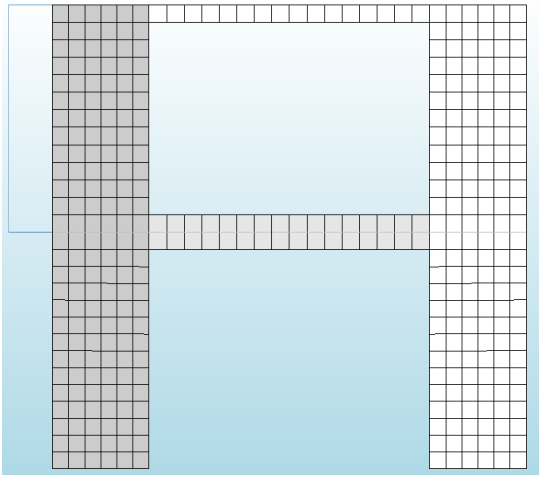

(b) $h_{spandrel}$ = 200mm

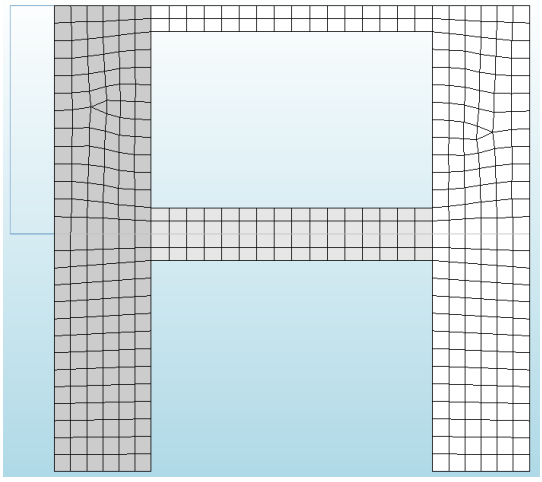

(c) $h_{spandrel}$ = 300mm

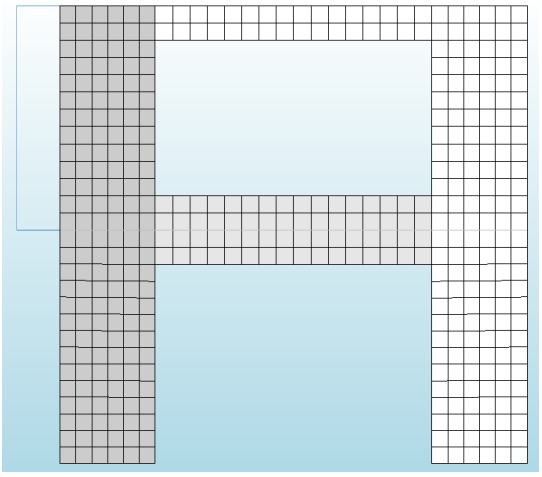

(d) $h_{spandrel}$ = 400mm

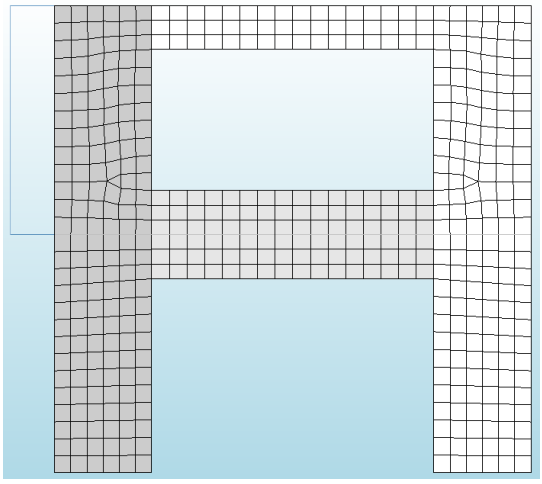

(e) $h_{spandrel}$ = 500mm

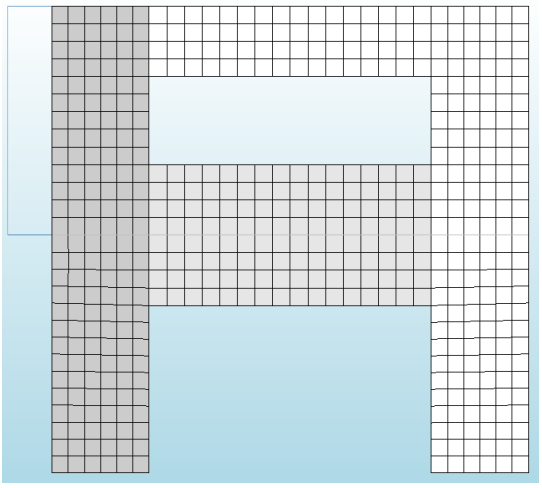

(f) $h_{spandrel}$ = 800mm

Figure 5.2: Spandrel geometry variations

5.2.2 ANALYSIS PROCEDURE

The analysis is performed using DIANA. In the first ten load steps the self-weight of the structure is applied. After this initial phase, the monotonic pushover is applied in positive $x-$direction. In Table 5.1 the analysis

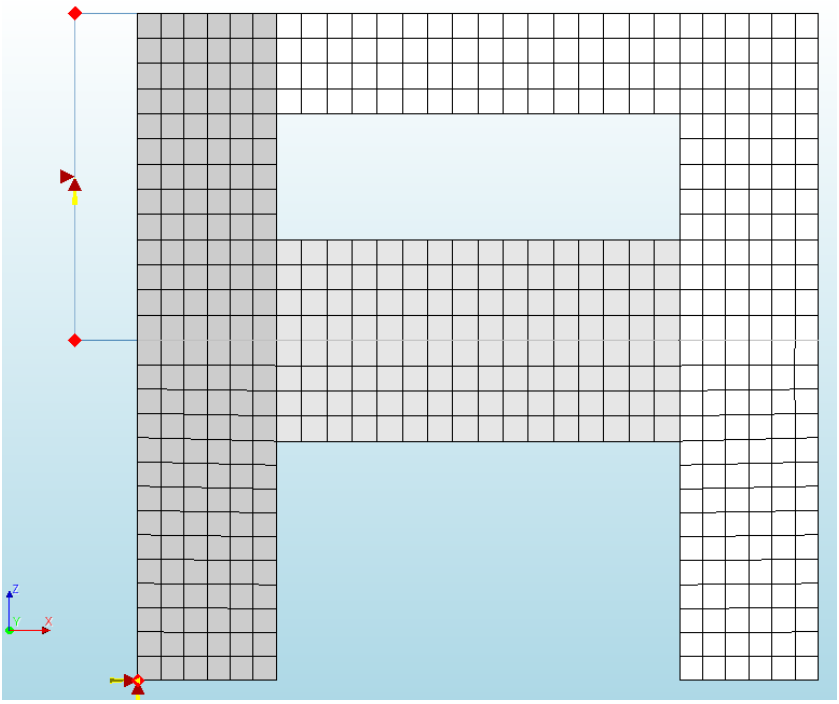

Figure 5.3: Steel frame to apply imposed displacement

Load Steps	Self-weight	10
	Monotonic Loading	300 steps (0.35 mm per step)
Iteration method	Max. number of iterations	100
	Iteration method	Regular Newton – Raphson
	First tangent	Tangential
	Line search	Yes
Convergence norm	Satisfy either displacement norm (tolerance 0.01) or force norm (tolerance 0.01)	

Table 5.1: Analysis procedure of the monotonic pushover analysis

procedure of both phases is summarized. In this numerical analysis both physical and geometrical nonlinearities are considered. The monotonic pushover load is applied in 300 steps of 0.35 mm. The maximum prescribed deformation in the last load step is 105 mm, which is 150% of the maximum displacement found in the original laboratory tests.

The regular Newton-Raphson iteration method is used with a maximum number of iterations limited to 100 per load step. The line search option is enabled for the iteration method. The convergence criteria are set to either satisfy the force norm of or the displacement norm.

5.3 RESULTS

The results of the monotonic pushover analyses in positive global x-direction on the various geometries are discussed in this section. The following subsections contain the results per geometry variation, starting with the base model, followed by models with increasing spandrel height. For all variations, the results are discussed by presenting the capacity curves obtained from the NLPO analyses. Initial- and secant stiffness as well as stiffness degradation are presented in relation to the capacity curves. Furthermore, the crack evolution is presented in relation to the capacity curves, as well as the interstorey drift and displacement profile. Finally, the results of the geometry variations are discussed and compared in relation to each other.

5.3.1 BASE MODEL

The base model is a slight variation on the building tested in the laboratory [1] and original model analysed by Xu [2]. The analysis on the original model was later repeated for a monotonic pushover analysis by Bhattarai *et al.* [67]. The change of the base model compared to the original model is the use of symmetry. Both piers have the same width, so the response in both direction is equal, therefore only one direction is considered. The results of the base model are presented and used to be able to make a clear comparison between these results and the results obtained from the models with a variation in geometry.

CAPACITY CURVE BASE MODEL

The capacity curve of the monotonic pushover analyses performed on the base model is shown in Figure 5.4. The figure presents the base shear force obtained from the boundary condition at the bottom left of the left pier in Figure 5.3. Since only half the model was analysed, due to symmetry, the obtained base shear force is doubled to represent the value for the full model. The second-floor displacement, shown in the graph, is derived from the node at the top left of the left pier.

The original model showed a similar initial stiffness of the numerical model compared to the experimental results. However, the finite element model exhibits an overestimation of the maximum shear force of the structure compared to the experimental findings. Additionally, it is evident that the shear force in the numerical model diminishes at a slower rate than in the experimental results, suggesting a higher ductility within the numerical representation. The peak force obtained from the numerical model is 52.3 kN, marking a 12% increase compared to the peak force obtained from the experimental results. It is expected that the numerical models for the geometry variations also show overestimation of maximum base shear force and slower shear force reduction compared to experimental results on these geometries.

Compared to the original model, the capacity of the base model is higher. The maximum base shear force obtained from the base model is 70.2 kN, which is 35% higher than the original model. This increase could be explained by the increase in width of the pier in the right side from 600 mm to 1100 mm. The piers, providing in-plane resistance, increase in total width by approximately 30%. Additionally, a monotonic PO analysis is applied, excluding the degradation related to cyclic loading in the original model. To illustrate the difference the capacity curve of the base model, the calibrated model by Xu [2] and the experimental results are shown in Figure 5.4.

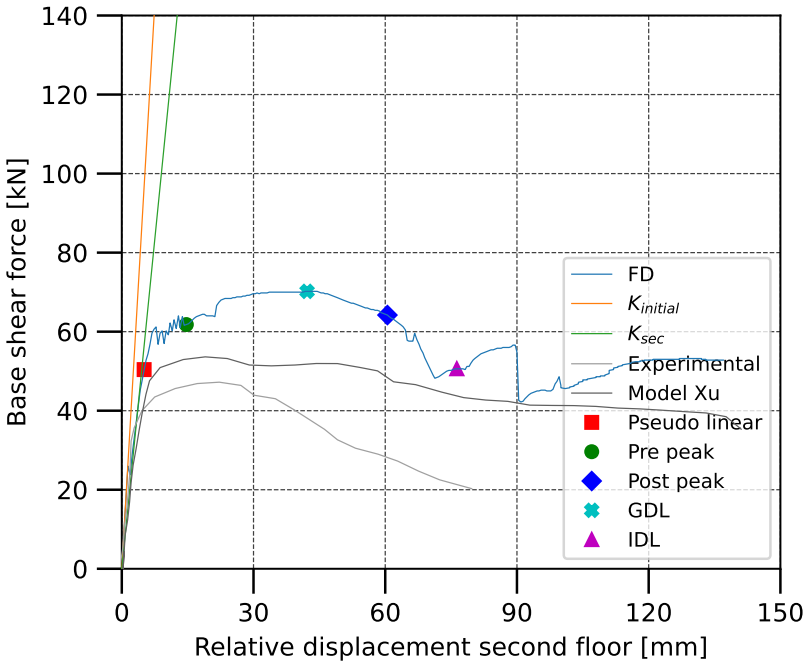

Figure 5.4: Capacity curve of base case model

In Figure 5.4 not only the capacity curves are shown, also the initial stiffness and secant stiffness of the base model are presented. The initial stiffness is defined as the stiffness obtained from the first load step of the pushover analysis. The secant stiffness is defined as the secant line through the origin and the point on the capacity curve where 60% of the maximum base shear force is reached. This value is given in NPR9998 [68] as a reliable equivalent stiffness that can be used to bi-linearise the force-displacement curve. The initial stiffness obtained from the model is 19.0 kN/mm, while the secant stiffness is 11.1 kN/mm. The ratio between the two values is 0.58, low values of this ratio are related to progressive damage, while when the ratio is close to 1.0 cracking occurs close to the peak load and the max capacity is reached more suddenly.

In the capacity curve five points are indicated. The pseudo linear point is defined in the stage of the analysis where the behaviour of the structure is still linear. In this stage no significant damage has occurred. The pre-peak point is defined before the maximum base shear force is reached, in the stage of the analysis where damage has occurred. The behaviour is clearly no longer linear, and some stiffness degradation has occurred. The post-peak point is defined after the maximum base shear force is reached, significant damage and stiffness degradation has occurred.

Note that the models with a spandrel height of 300 mm and more do not show a clear peak. These models reach a plateau. For these models, the same names are used for the three points; however, the pre-peak and post-peak points are defined differently. The pre-peak point is defined in the stage of the analysis following the pseudo linear stage. Similar to the definition in the other models some damage has occurred in this stage. The post-peak point is defined after a clear drop of capacity in the plateau stage. Similar to the definition in the other models, significant damage has occurred in this stage.

Apart from these three stages global drift limit (GDL) and interstorey drift limit (IDL) are indicated. These are the points where global drift reaches 0.8% and interstorey drift reaches 1.5%. Global drift and interstorey drift denote the ratio of the second-floor's displacement to the building's total height and the ratio of relative floor displacement to the height of the corresponding floor, respectively.

CRACK EVOLUTION BASE MODEL

The crack pattern observed during the positive monotonic pushover analysis is discussed, since this load case is considered for the following geometry variations. For comparison, the crack pattern obtained from the experimental results are included in Figure 5.5. The crack plots obtained from the model are presented in terms of the crack widths of the masonry walls. The crack width corresponding to a fully open crack can be reasonably estimated by multiplying the crack strain (Equation 4.2) by the element size, i.e. 200 mm. Based on the material properties a crack strain of 0.0007 is considered fully open. Consequently, a crack width of 0.13 mm is considered fully open and therefore used in the considered crack plots.

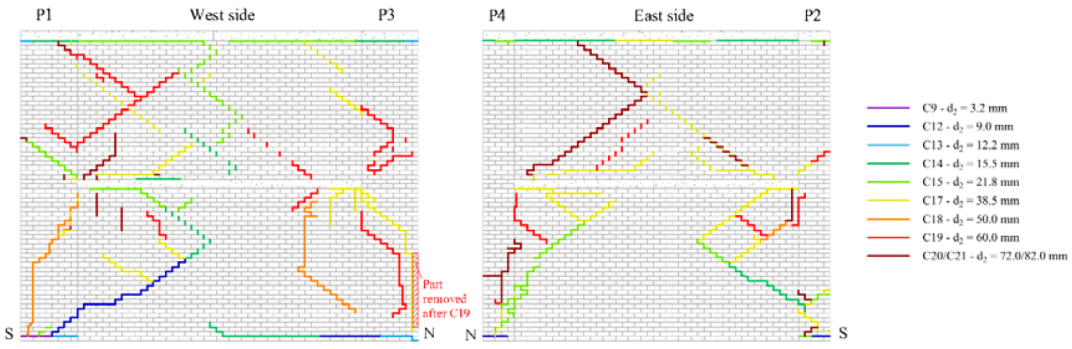

Figure 5.5: Crack pattern obtained from experimental results [1]

The initial cracks in the base model appear first at the top and bottom of the piers, mainly in the pier on the right side. These cracks gradually widen, implying a rocking mechanism in both piers when the base shear force reaches 50.4 kN and a corresponding second-floor displacement of 5.01 mm. In Figure 5.6 this stage's crack pattern is displayed, revealing cracks not only in the piers but also in the transverse walls at the

location of rigid connections between wall and floor.

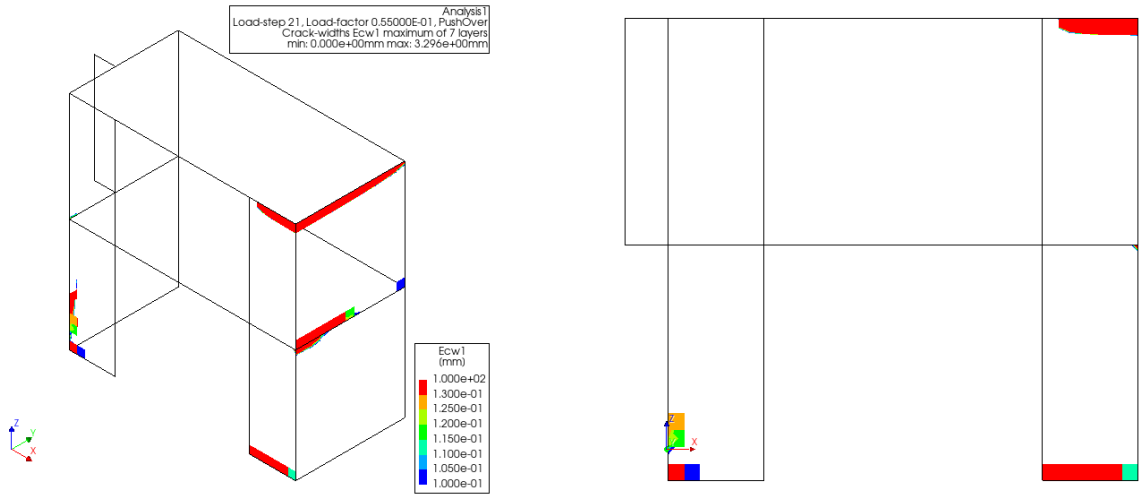

Figure 5.6: Crack pattern in the pseudo linear stage of base model

While the primary cracks persist in their positions at the top and bottom of the pier, they progressively extend into other areas of both the piers and the transverse walls. Notably, crack openings emerge at the edge of the left pier and into the transverse wall on the ground floor when the base shear force reaches 61.8 kN, and the lateral displacement of the second floor hits 14.7 mm. In Figure 5.7 the crack width at this stage is shown. With increasing displacement diagonal cracks emerge in the centre of the left pier at the ground floor. These shear cracks within the left pier further develop and, start to form at the first floor of the right pier, with increasing lateral displacement, a trend demonstrated in Figure 5.8, depicting the crack width when the base shear force and second-floor displacement attain 64.2 kN and 60.5 mm, respectively. It is crucial to highlight that the latter stage is in the post-peak region of the pushover capacity curve.

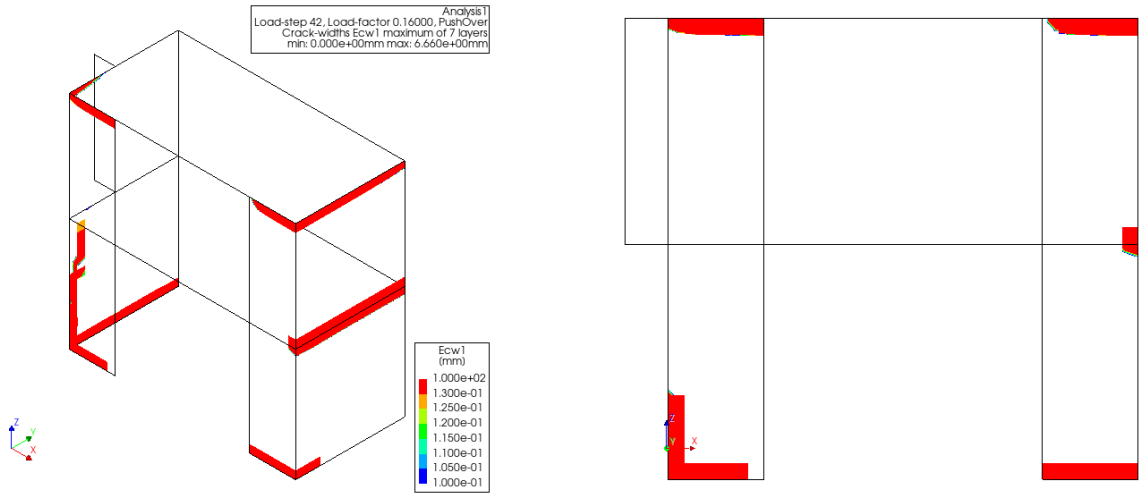

Figure 5.7: Crack pattern in the pre-peak stage of base model

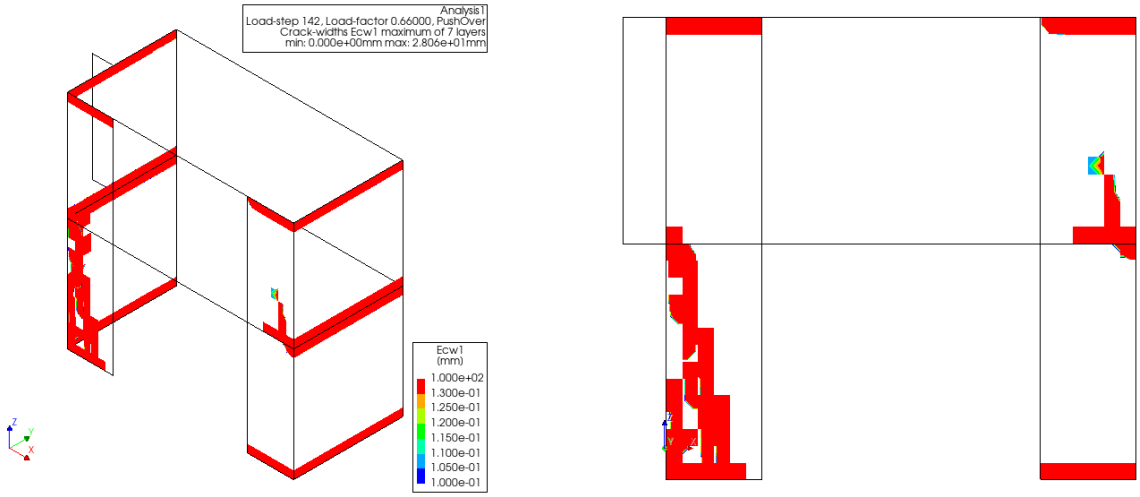

Figure 5.8: Crack pattern in the post-peak stage of base model

Apart from the three discussed stages, it is crucial for interpreting damage evolution to monitor specific points where the global drift limit (GDL) reaches 0.8% and the interstorey drift limit (IDL) hits 1.5%. Global drift and interstorey drift denote the ratio of the second-floor's displacement to the building's total height and the ratio of relative floor displacement to the height of the corresponding floor, respectively. Figure 5.9 illustrates the crack widths observed at the GDL. Similarly, Figure 5.10 depicts the crack widths observed when the IDL, specifically at the first-floor level, is reached. At the latter stage cracks are extending into the piers on the first floor and the transverse wall on the left.

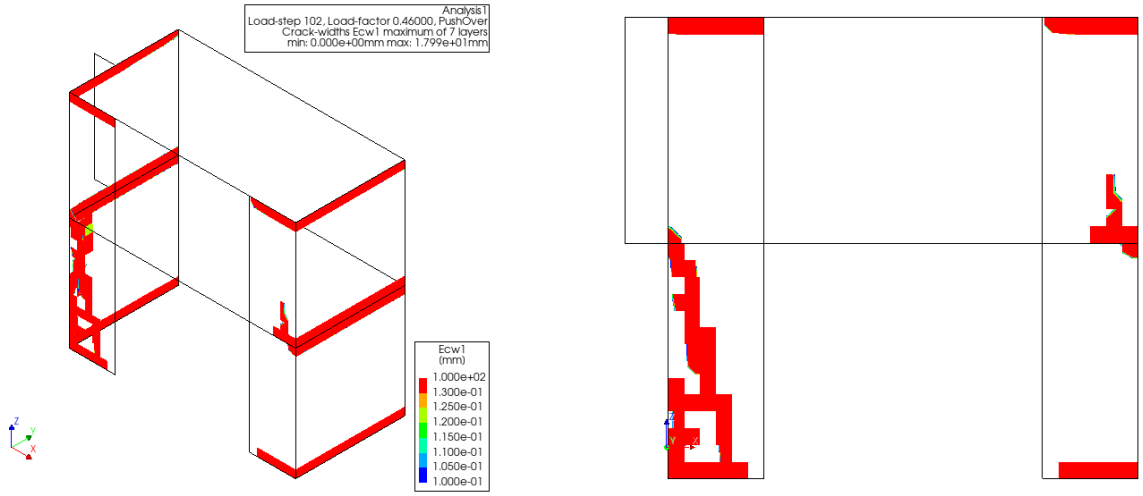

Figure 5.9: Crack width when global drift reaches 0.8% in the base model

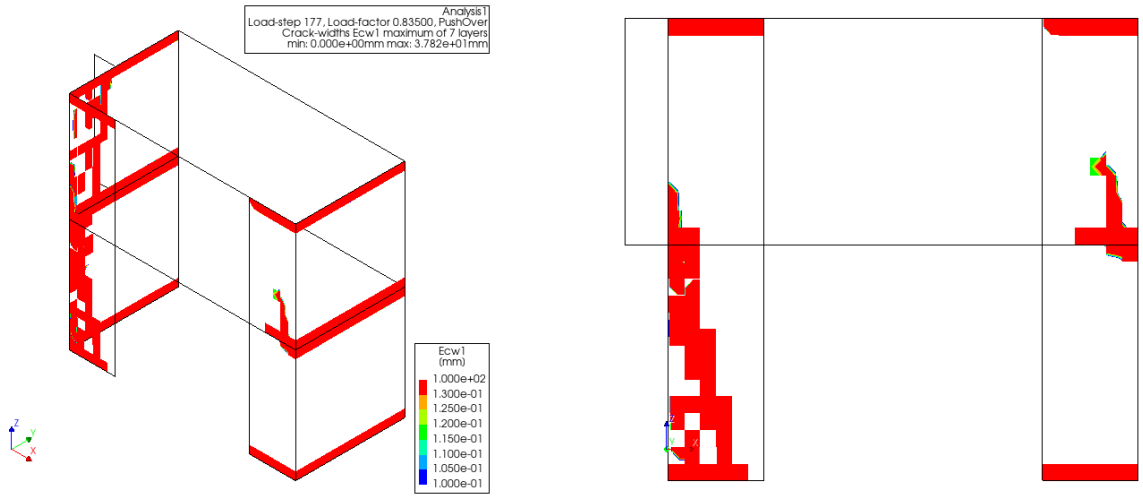

Figure 5.10: Crack width when interstorey drift reaches 1.5% in the base model

INTERSTOREY DRIFT

The interstorey drift, as explained above, is determined by dividing the relative floor displacement by the interstorey height, i.e. 2700 mm at ground floor level and 2600 mm at first floor level. In Figure 5.11 the interstorey drift for both floors is shown. The interstorey drift of the ground floor increases more than the interstorey drift of the first floor. Therefore, the limit of 1.5% is reached in the ground floor first. This is in line with the cracks observed, which are more prevalent in the ground floor.

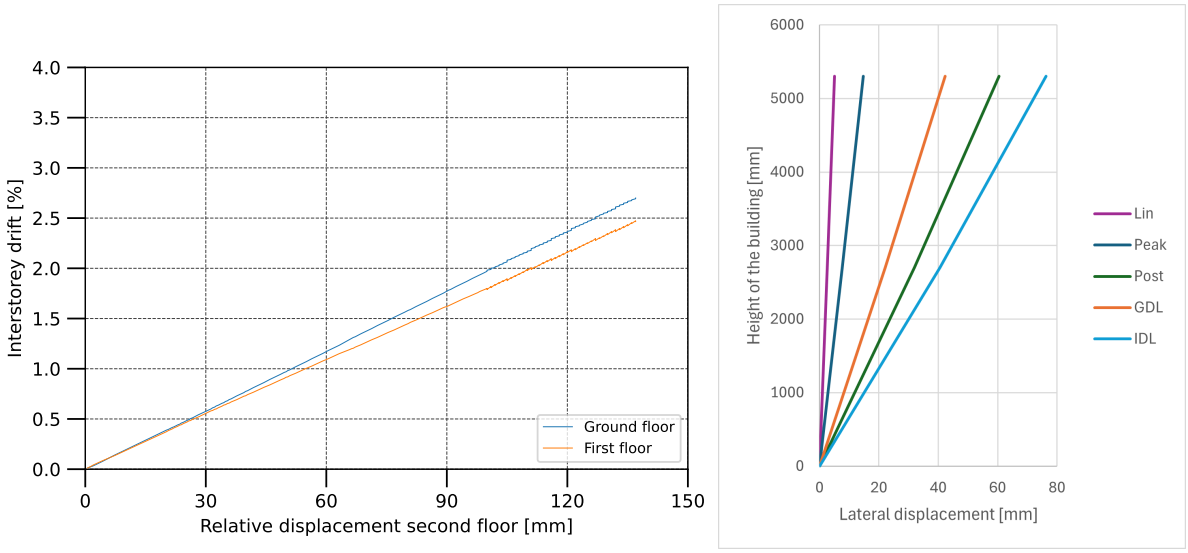

Figure 5.11: Interstorey drift of ground- and first floor and displacement profile of the base model

The interstorey drift is relevant for further comparison with the results of the models with geometry variations. Therefore, these results are summarised here. In the initial stage the interstorey drifts of both floors are identical, but they gradually diverge after reaching the peak. As shear cracks develop in the middle of the pier at ground floor level, further damage tends to concentrate in that specific area. This might explain the higher drift observed in the ground floor compared to the first floor. However, it should be noted that the interstorey drifts observed in both floors is very comparable in this geometry. The displacement profile of the house at the five levels marked in Figure 5.4, including the points where GDL and IDL are reached, is depicted in Figure 5.11.

5.3.2 MODEL WITH SPANDREL HEIGHT 81 MM

The model with a spandrel height of 81 mm, as presented in 5.2a, is discussed in this section. This model is only a slight variation on the base model. As described in section 5.1, in the model spandrels are introduced with a height related to the floor thickness. It provides insight in how the model is affected by the introduction of spandrels.

CAPACITY CURVE SPANDREL HEIGHT 81 MM

The capacity curve of the monotonic pushover analyses performed on the model with spandrel height of 81 mm is shown in Figure 5.12. Similar to the base model, the figure presents the base shear force obtained from the boundary condition at the bottom left of the left pier and the second-floor displacement from the top left of the left pier.

The peak force obtained from the numerical model is 73.6 kN, marking a 5% increase compared to the peak force obtained from the base model results. The slight change in maximum base shear force could be expected, since there is only a slight change in geometry compared to the base model.

The initial stiffness and secant stiffness are plotted in the same graph. The initial stiffness obtained from the model is 19.2 kN/mm, while the secant stiffness is 11.3 kN/mm. The ratio between the two values is 0.59, low values of this ratio are related to progressive damage, while when the ratio is close to 1 the cracking occurs close to the peak load and the max capacity is reached more suddenly.

CRACK EVOLUTION SPANDREL HEIGHT 81 MM

The initial cracks in the model with a spandrel height of 81 mm appear first at the top and bottom of the piers, mainly in the pier on the right side. These cracks gradually widen, implying a rocking mechanism in

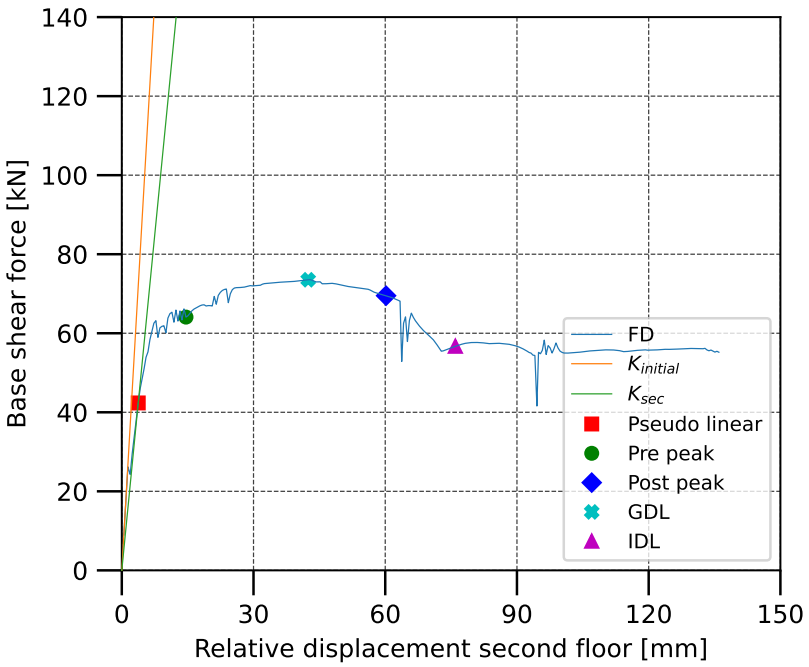

Figure 5.12: Capacity curve, initial stiffness, and secant stiffness of model with spandrel height 81 mm

both piers when the base shear force reaches 42.4 kN and a corresponding second-floor displacement of 3.74 mm. In Figure 5.13 this stage's crack pattern is displayed, revealing cracks not only in the piers but also in the transverse walls at the location of rigid connections between wall and floor.

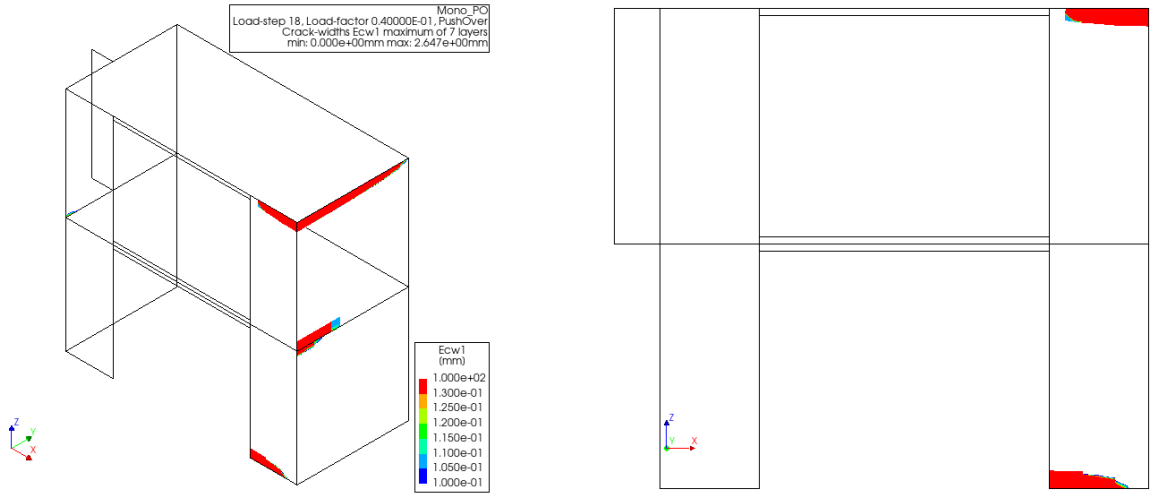

Figure 5.13: Crack pattern in the pseudo linear stage of model 81 mm

While the primary cracks persist in their positions at the top and bottom of the pier, they progressively extend into other areas of both the piers and the transverse walls. Notably, crack openings emerge at the edge of the left pier and into the transverse wall on the ground floor when the base shear force reaches 60.2 kN, and the lateral displacement of the second floor hits 14.6 mm. In Figure 5.14 the crack width at this stage is shown. With increasing displacement diagonal cracks emerge in the centre of the left pier at the ground floor. These shear cracks within the left pier further develop with increasing lateral displacement, a trend demonstrated in Figure 5.15, depicting the crack width when the base shear force and second-floor displacement attain 69.5

kN and 60.2 mm, respectively. This behaviour occurs in the post-peak region of the pushover capacity curve.

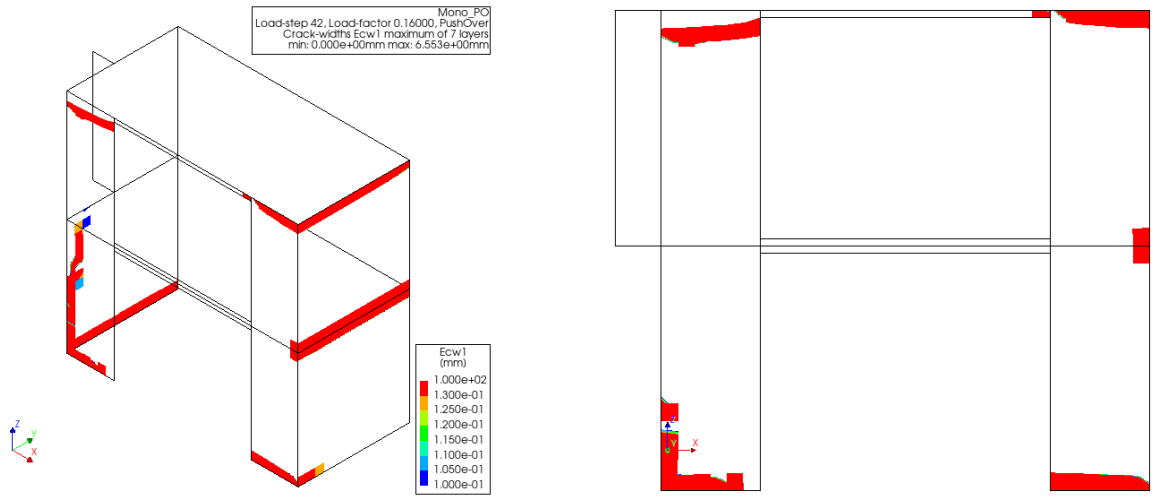

Figure 5.14: Crack pattern in the pre-peak stage of model 81 mm

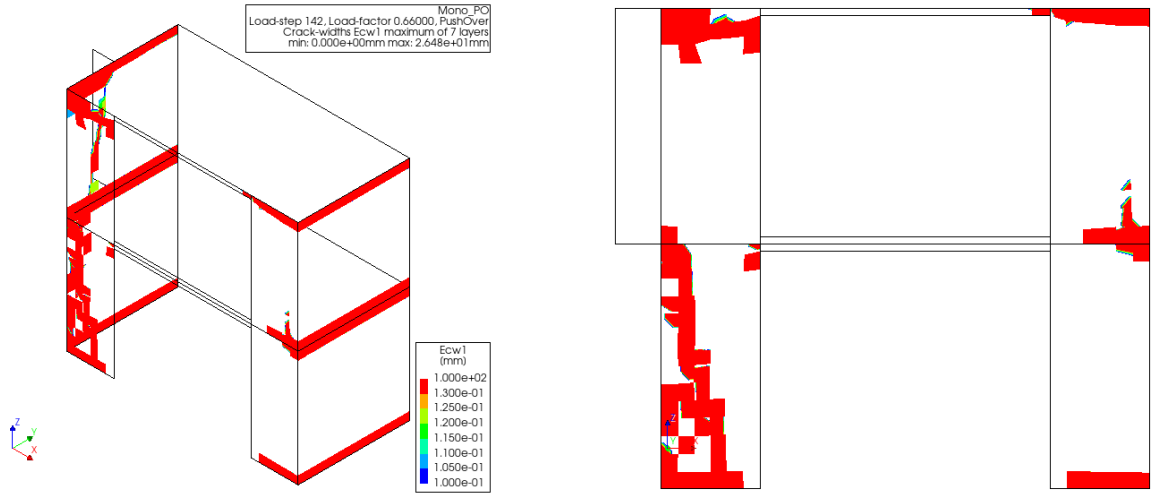

Figure 5.15: Crack pattern in the post-peak stage of model 81 mm

The global drift limit and interstorey drift limit for the model are also determined. A global drift of 0.8% is reached in load step 103, corresponding to a base shear force of 73.5 kN and a second-floor displacement of 42.5 mm. The crack widths occurring at this stage are show in Figure 5.16. An interstorey drift of 1.5% is reached in load step 177, the limit is reached in the ground floor level. At this stage the base shear force equals 56.7 kN, with a second-floor displacement of 76.0 mm. The cracks in this stage, shown in Figure 5.17, extend into the left pier on the first floor as well as the transverse wall on the left.

INTERSTOREY DRIFT SPANDREL HEIGHT 81 MM

In Figure 5.18 the interstorey drift for both floors is shown. The interstorey drift of the ground floor increases more than the interstorey drift of the first floor. Therefore, the limit of 1.5% is reached in the ground floor first. This is in line with the cracks observed, which are more prevalent in the ground floor.

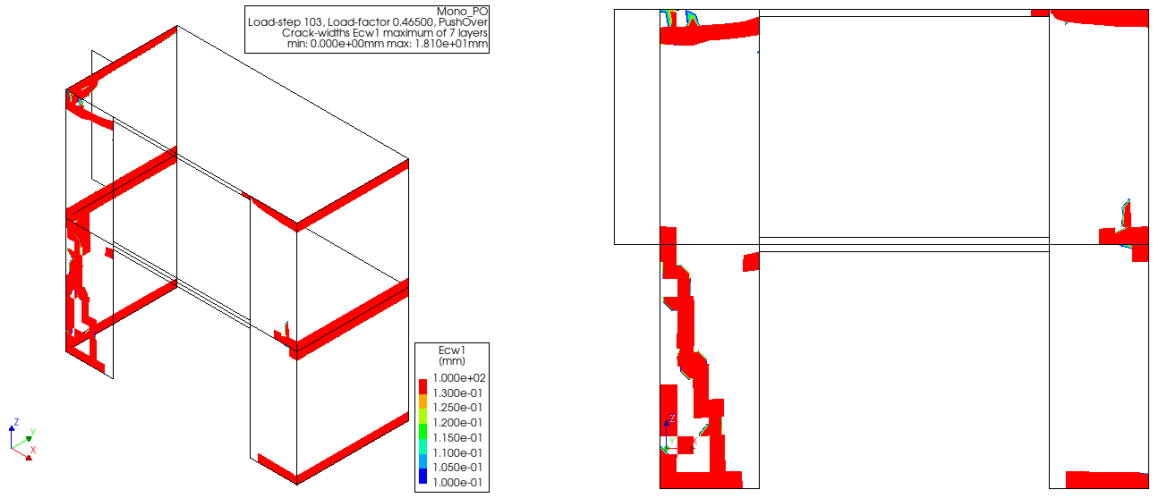

Figure 5.16: Crack width when global drift reaches 0.8% in model 81 mm

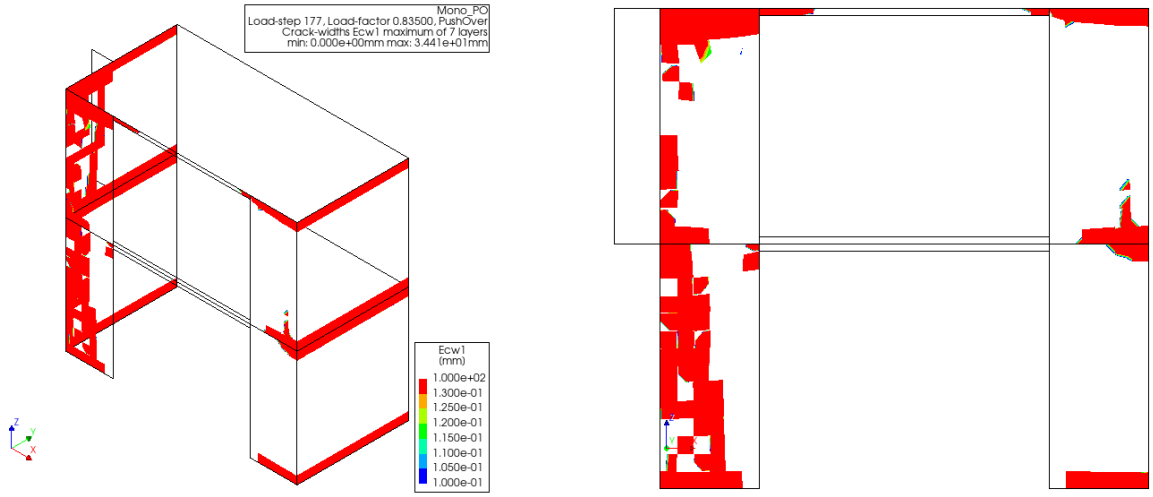

Figure 5.17: Crack width when interstorey drift reaches 1.5% in model 81 mm

In the initial stage the interstorey drifts of both floors are identical, but they gradually diverge after reaching the peak. As shear cracks develop in the middle of the pier at ground floor level, further damage tends to concentrate in that specific area. This might explain the higher drift observed in the ground floor compared to the first floor. The displacement profile of the house at the five levels marked in Figure 5.12, including the points where GDL and IDL are reached, is depicted in Figure 5.18.

5.3.3 MODEL WITH SPANDREL HEIGHT 200 MM

The model with a spandrel height of 200 mm, as presented in 5.2b, is discussed in this section. The spandrels in this model have a height of 200 mm, which is equal to a single element in the finite element model.

CAPACITY CURVE SPANDREL HEIGHT 200 MM

The capacity curve of the monotonic pushover analyses performed on the model with spandrel height of 200 mm is shown in Figure 5.19. This figure illustrates the base shear force, which is determined by the boundary conditions at the lower left corner of the left pier, and the displacement of the second floor at the upper left corner of the same pier, similar to the results observed in previous models.

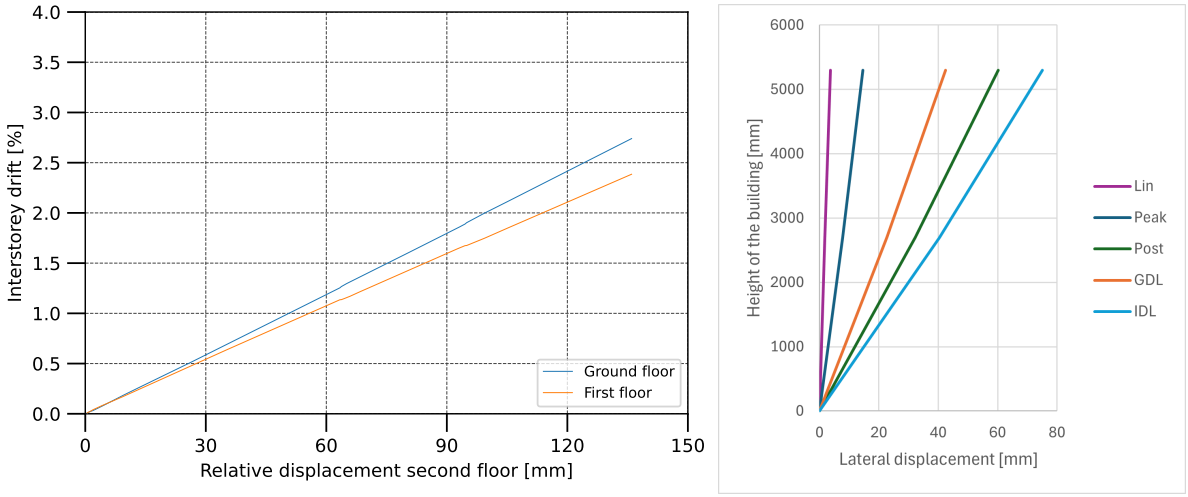

Figure 5.18: Interstorey drift of ground- and first floor and displacement profile of model 81 mm

The peak force obtained from the numerical model is 89.9 kN, marking a 22% increase compared to the peak force obtained from the model with an 81 mm spandrel height. The increase in spandrel height increases the area of the in-plane loaded wall and decreases the height of the piers between the spandrels. The reduces height might explain a higher resistance against a rocking type of failure.

The initial stiffness and secant stiffness are plotted in the same graph. The initial stiffness obtained from the model is 20.7 kN/mm, while the secant stiffness is 12.0 kN/mm. The ratio between the two values is 0.58, which is similar to the ratio found in the previous model and is associated to progressive damage.

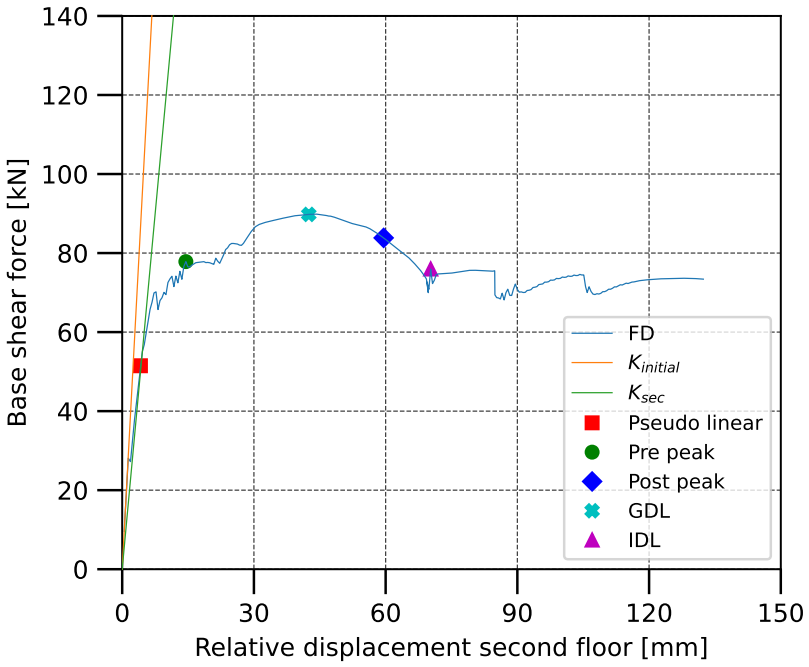

Figure 5.19: Capacity curve, initial stiffness, and secant stiffness of model with spandrel height 200 mm

CRACK EVOLUTION SPANDREL HEIGHT 200 MM

The initial signs of damage in the model, which features a spandrel height of 200 mm, manifest as cracks at the upper and lower regions of the piers, predominantly on the right-side pier. These cracks progressively expand, suggesting a rocking mechanism within both piers. This phenomenon becomes apparent when the base shear force reaches 51.5 kN, coinciding with a second-floor displacement of 4.15 mm. Figure 5.20 illustrates the crack pattern at this phase, highlighting not only the piers but also the transverse walls, particularly the formation of cracks where rigid connections exist between the walls and the floor.

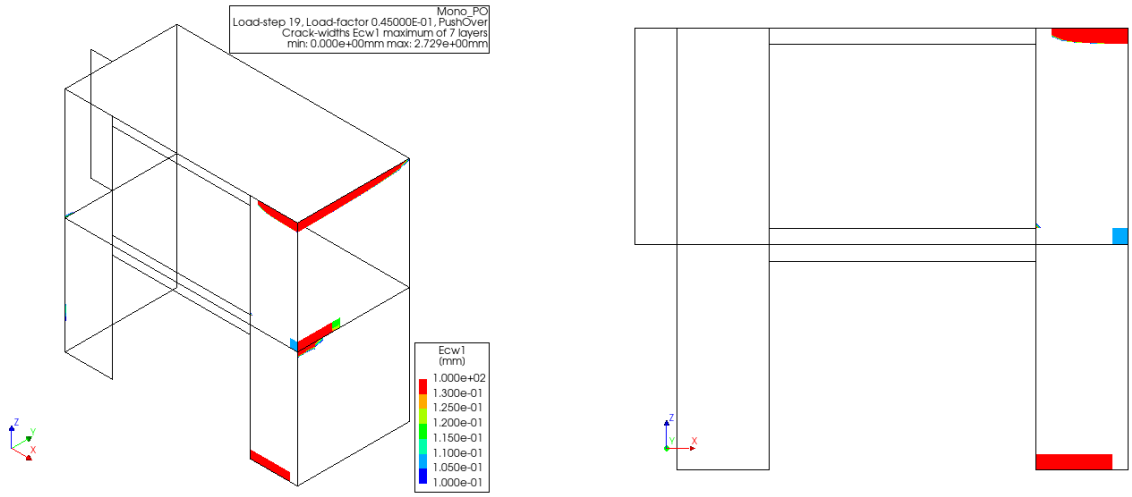

Figure 5.20: Crack pattern in the pseudo linear stage of model 200 mm

The primary cracks remain fixed at the top and bottom of the pier, yet they gradually spread to other sections of both the piers and the transverse walls. Notably, cracks begin to appear at the edge of the left pier and extend into the transverse wall on the ground floor when the base shear force hits 77.8 kN, coinciding with a lateral displacement of 14.5 mm on the second floor. The crack width in this stage is illustrated in Figure 5.21. As the displacement increases, diagonal cracks start to form in the centre of the left pier at the ground level. These shear cracks in the left pier continue to evolve as the lateral displacement grows, a pattern that is evident in Figure 5.22, which shows the crack width at the point where the base shear force reaches 83.8 kN and the second-floor displacement is 59.6 mm. At this point diagonal shear cracks also start to for in the right pier. This pattern of cracking is observed in the post-peak phase of the pushover capacity curve. Diagonal shear cracks in the right pier were not observed in the previous models.

The global drift limit and interstorey drift limit for the model are also determined. A global drift of 0.8% is reached in load step 104, corresponding to a base shear force of 89.8 kN and a second-floor displacement of 42.5 mm. The crack widths occurring at this stage are show in Figure 5.23. An interstorey drift of 1.5% is reached in load step 168, the limit is reached in the ground floor level. At this stage the base shear force equals 76.0 kN, with a second-floor displacement of 70.3 mm. The cracks in this stage, shown in Figure 5.24, propagate into the left pier on the first floor and the adjacent transverse wall. The rigid connection between floors and transverse walls are all fully cracked at this stage. The diagonal shear cracks in the right pier continue to grow at this stage.

INTERSTOREY DRIFT SPANDREL HEIGHT 200 MM

Figure 5.25 illustrates the interstorey drift for both the ground and first floors. It is evident that the drift experienced by the ground floor is significantly greater, than at the first floor. Consequently, the ground floor reaches the threshold limit of 1.5% interstorey drift before the first floor does. This observation correlates with the distribution of cracks, which are predominantly found on the ground floor. The sudden increase in interstorey drift at the ground floor around the 1.5% mark coincides with a sudden change in the capacity

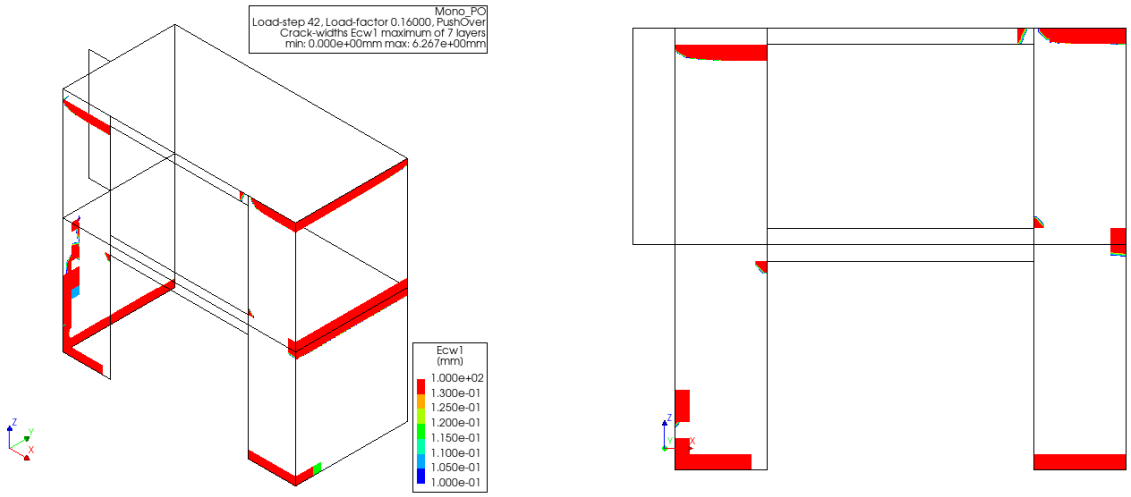

Figure 5.21: Crack pattern in the pre-peak stage of model 200 mm

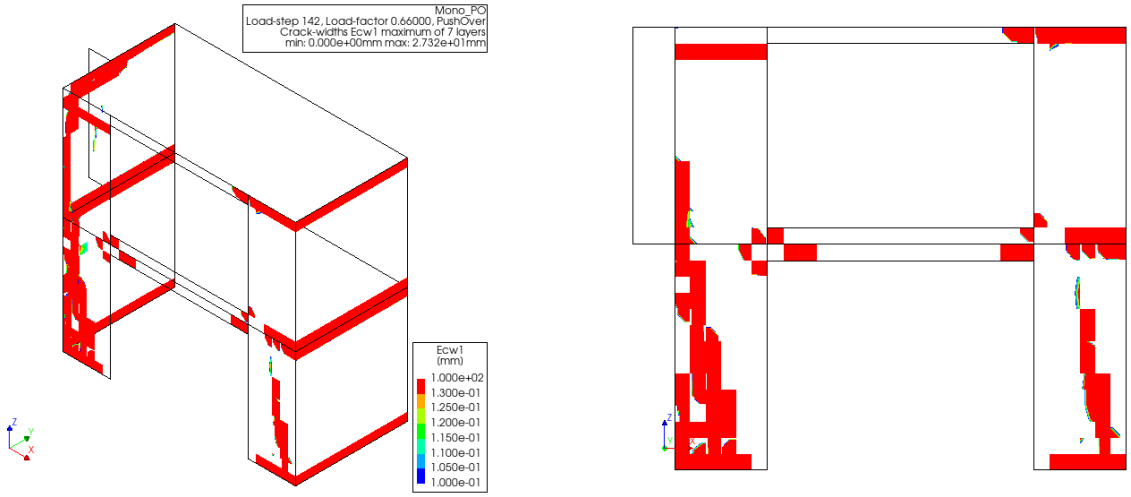

Figure 5.22: Crack pattern in the post-peak stage of model 200 mm

curve, which could be caused by the sudden formation of new cracks.

In the initial stage the interstorey drifts of both floors are identical, but they gradually diverge after reaching the peak. As shear cracks develop in the middle of the piers at ground floor level, further damage tends to concentrate in those areas. This might explain the higher drift observed in the ground floor compared to the first floor. The displacement profile of the house at the five levels marked in Figure 5.19, including the points where GDL and IDL are reached, is depicted in Figure 5.25.

5.3.4 MODEL WITH SPANDREL HEIGHT 300 MM

The model with a spandrel height of 300 mm, as presented in 5.2c, is discussed in this section. The spandrels in this model have a height of 300 mm, which is not a multiple of 200. This causes the mesh to be less regular, however not in such a way that it would influence the results.

CAPACITY CURVE SPANDREL HEIGHT 300 MM

The capacity curve of the monotonic pushover analyses performed on the model with spandrel height of 300 mm is shown in Figure 5.26. This figure illustrates the base shear force, which is determined by the boundary

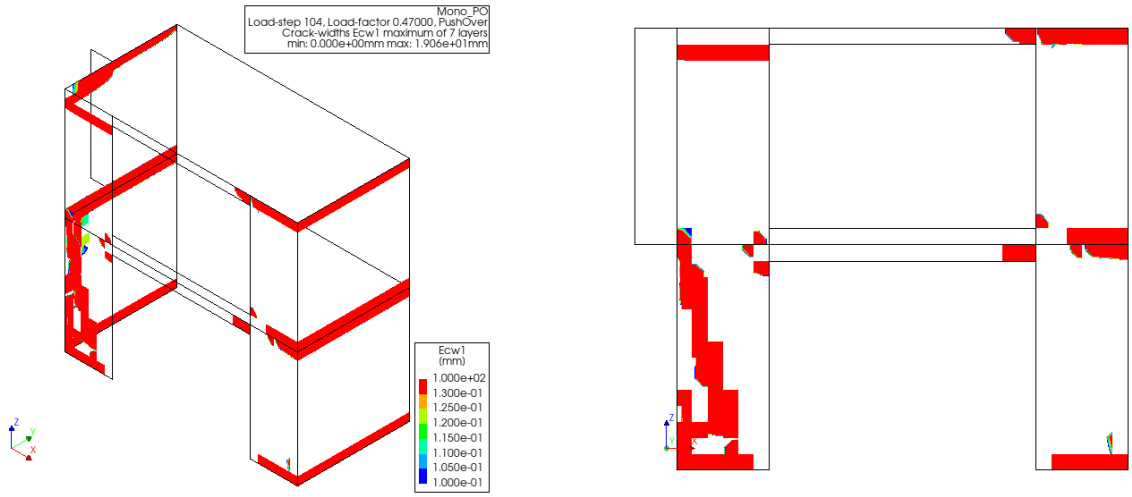

Figure 5.23: Crack width when global drift reaches 0.8% in model 200 mm

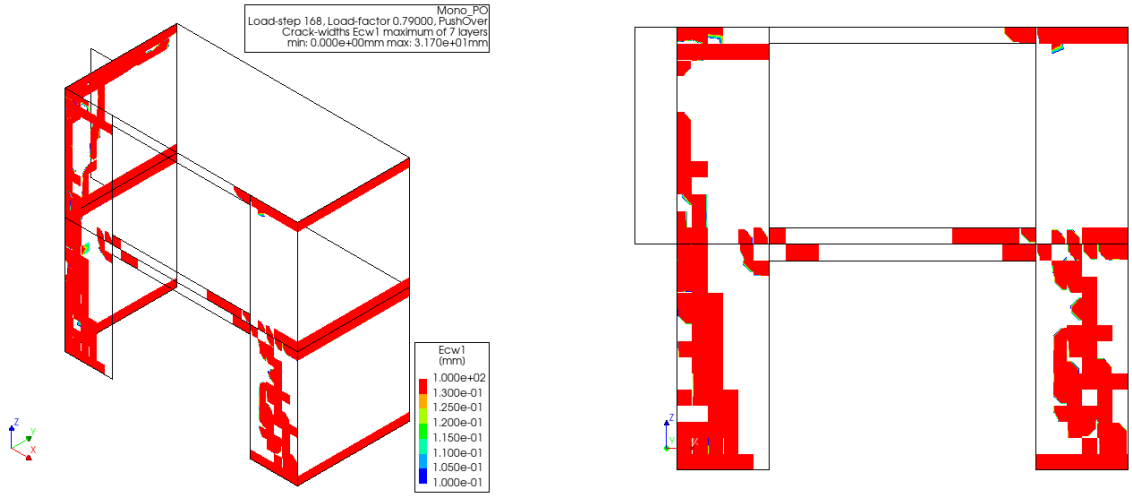

Figure 5.24: Crack width when interstorey drift reaches 1.5% in model 200 mm

conditions at the lower left corner of the left pier, and the displacement of the second floor at the upper left corner of the same pier, similar to the results observed in previous models.

The peak force obtained from the numerical model is 98.1 kN, marking a 9% increase compared to the peak force obtained from the model with a 200 mm spandrel height results. The increase in spandrel height increases the area of the in-plane loaded wall and decreases the height of the piers between the spandrels. The reduces height might explain a higher resistance against a rocking type of failure. The increase in spandrel height from 200 mm to 300 mm is relatively small compared to the increase from 81 mm to 200 mm, which might explain the smaller increase in maximum base shear force.

The initial stiffness and secant stiffness are plotted in the same graph. The initial stiffness obtained from the model is 23.5 kN/mm, while the secant stiffness is 14.6 kN/mm. The ratio between the two values is 0.62, which is slightly higher than the ratio found in the previous model and is associated to progressive damage.

A clear difference between the capacity curve and the curves of the models with less spandrel height is observed. Instead of a clear peak a sort of plateau with spikes occurs.

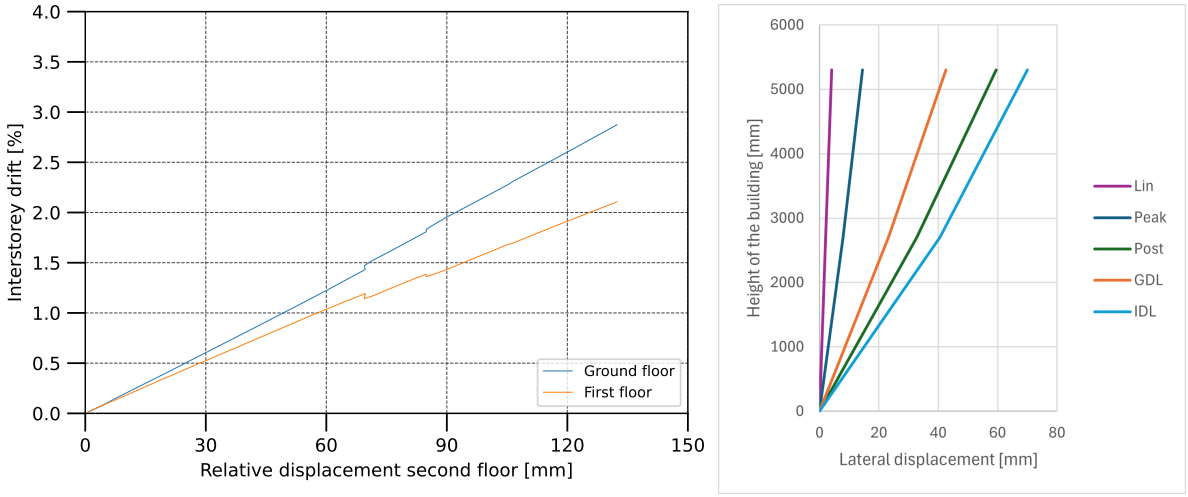

Figure 5.25: Interstorey drift of ground- and first floor and displacement profile of model 200 mm

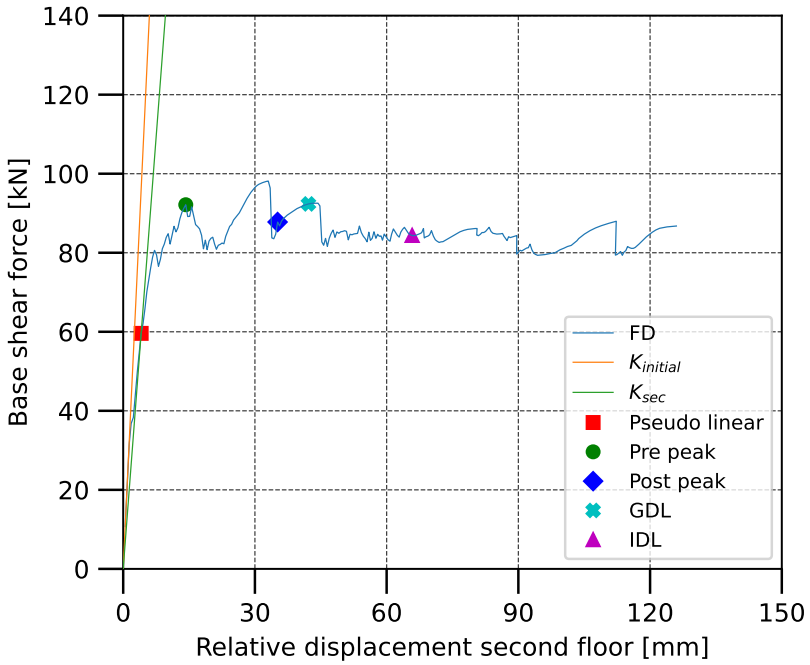

Figure 5.26: Capacity curve, initial stiffness, and secant stiffness of model with spandrel height 300 mm

CRACK EVOLUTION SPANDREL HEIGHT 300 MM

The initial signs of damage in the model, which features a spandrel height of 300 mm, manifest as cracks at the upper and lower regions of the piers, predominantly on the right-side pier. These cracks progressively expand, suggesting a rocking mechanism within both piers. However, in contrast to the previous models at this stage, cracks begin to appear at the edge of the left pier. Cracks also start to form at the bottom of the top-right pier, at the connection with the spandrel. This phenomenon becomes apparent when the base shear force reaches 59.6 kN, coinciding with a second-floor displacement of 4.09 mm. Figure 5.27 illustrates the crack pattern at this phase, highlighting not only the piers but also the transverse walls, particularly the formation of cracks where rigid connections exist between the walls and the floor.

The primary cracks remain fixed at the top and bottom of the pier, yet they gradually spread to other sections of both the piers and the transverse walls. It is notable the cracks forming at the top of the left pier

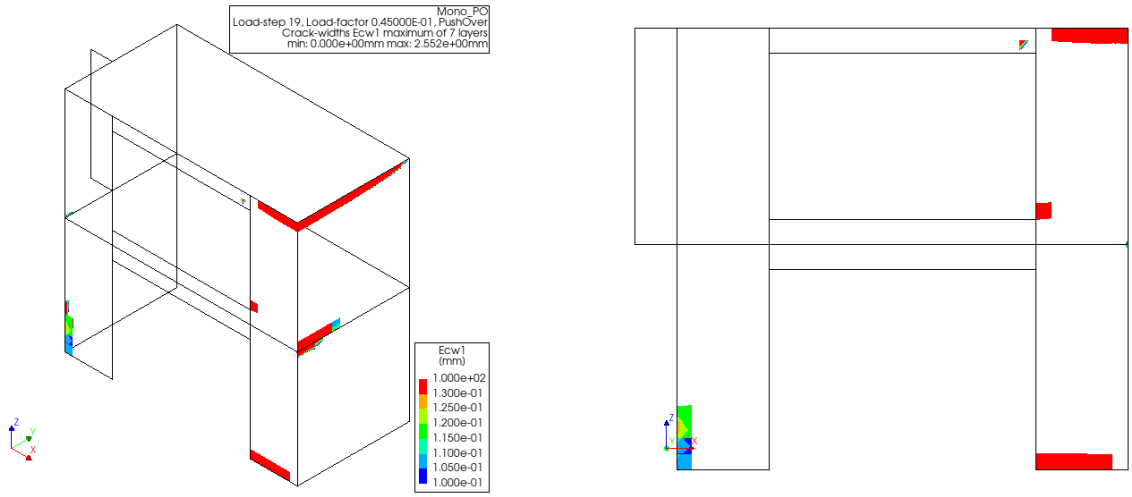

Figure 5.27: Crack pattern in the pseudo linear stage of model 300 mm

appear at the bottom of the spandrel. Diagonal shear cracks begin to appear at the bottom-left pier, with additional cracks developing at the pier's edge and extending into the transverse wall on the ground floor, when the base shear force reaches 92.1 kN, corresponding to a lateral displacement of 14.2 mm on the second floor. The crack width in this stage is illustrated in Figure 5.28. As the displacement increases, diagonal cracks extend in the centre of the left pier and start to form at the right pier at the ground level. These shear cracks continue to evolve as the lateral displacement grows, a pattern that is evident in Figure 5.29, which shows the crack width at the point where the base shear force reaches 87.8 kN and the second-floor displacement is 35.2 mm. This pattern of cracking is observed in the post-peak phase of the pushover capacity curve. It is also worth noting that there is crack development in the bottom spandrel, which was less apparent in the previous model. At this stage, the rigid connection between floors and transverse walls are all fully cracked.

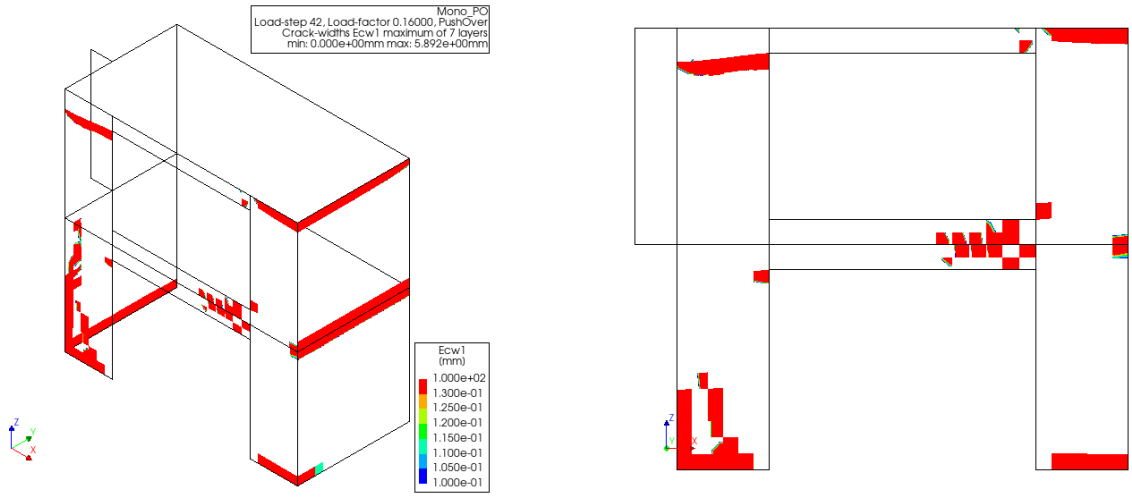

Figure 5.28: Crack pattern in the pre-peak stage of model 300 mm

The global drift limit and interstorey drift limit for the model are also determined. A global drift of 0.8% is reached in load step 106, corresponding to a base shear force of 92.4 kN and a second-floor displacement of 42.2 mm. The crack widths occurring at this stage are show in Figure 5.30. An interstorey drift of 1.5% is reached in load step 162, the limit is reached in the ground floor level. At this stage the base shear force equals 84.4 kN, with a second-floor displacement of 65.8 mm. The cracks in this stage, shown in Figure 5.31, propagate into the left pier on the first floor and the adjacent transverse wall. The piers at the height of the

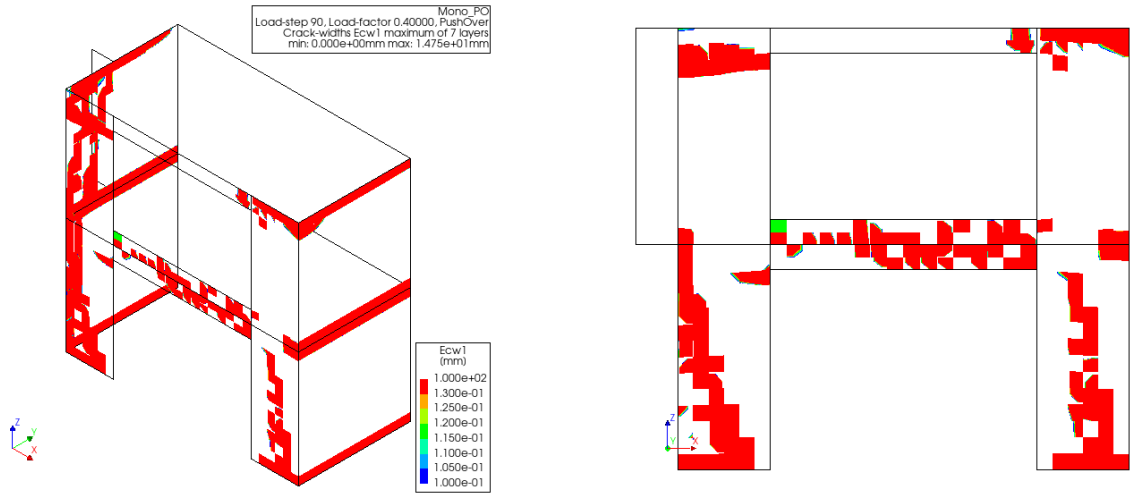

Figure 5.29: Crack pattern in the post-peak stage of model 300 mm

top spandrel are fully cracked. The diagonal shear cracks in both bottom piers continue to grow at this stage.

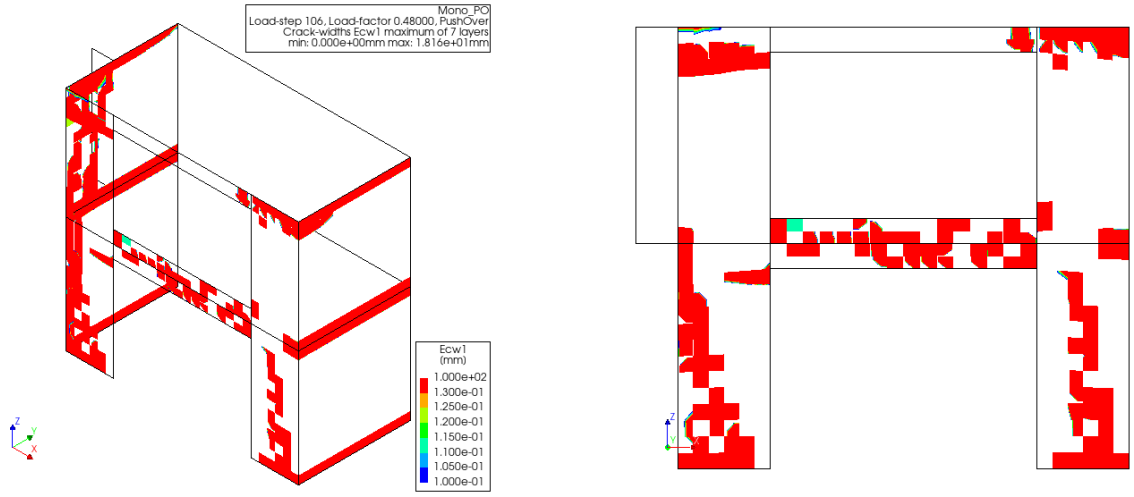

Figure 5.30: Crack width when global drift reaches 0.8% in model 300 mm

INTERSTOREY DRIFT SPANDREL HEIGHT 300 MM

Figure 5.32 illustrates the interstorey drift for both the ground and first floors. It is evident that the drift experienced by the ground floor is significantly greater, than at the first floor. Consequently, the ground floor reaches the threshold limit of 1.5% interstorey drift before the first floor does. This observation correlates with the distribution of cracks, which are predominantly found on the ground floor. In this model the first floor barely reaches the interstorey drift of 1.5%.

The interstorey drifts of both floors start to diverge early in the analysis. As shear cracks develop in the middle of the piers at ground floor level, further damage tends to concentrate in those areas and the lower spandrel. This might explain the higher drift observed in the ground floor compared to the first floor. The displacement profile of the house at the five levels marked in Figure 5.26, including the points where GDL and IDL are reached, is depicted in Figure 5.32. It is notable that the displacement profile becomes less linear compared to the previous geometries.

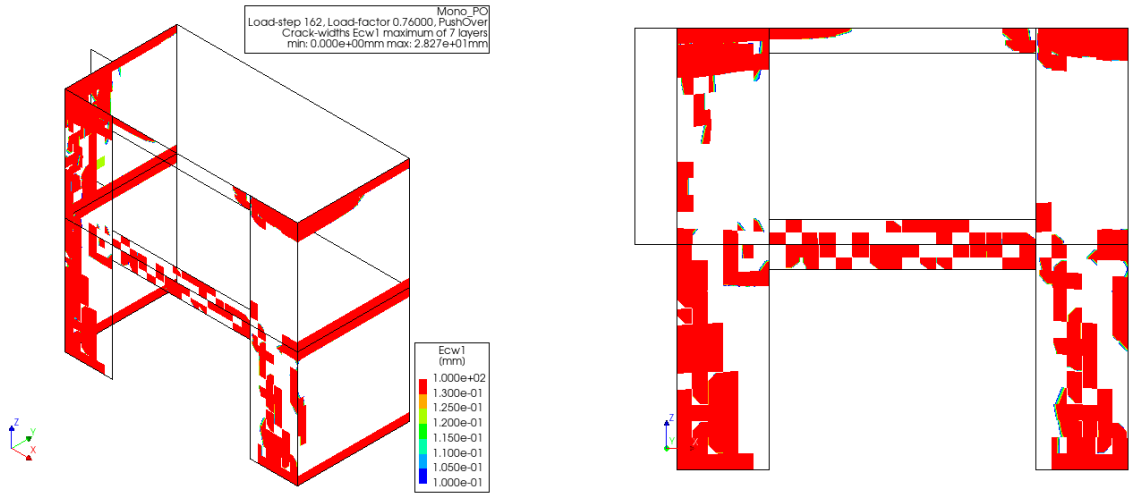

Figure 5.31: Crack width when interstorey drift reaches 1.5% in model 300 mm

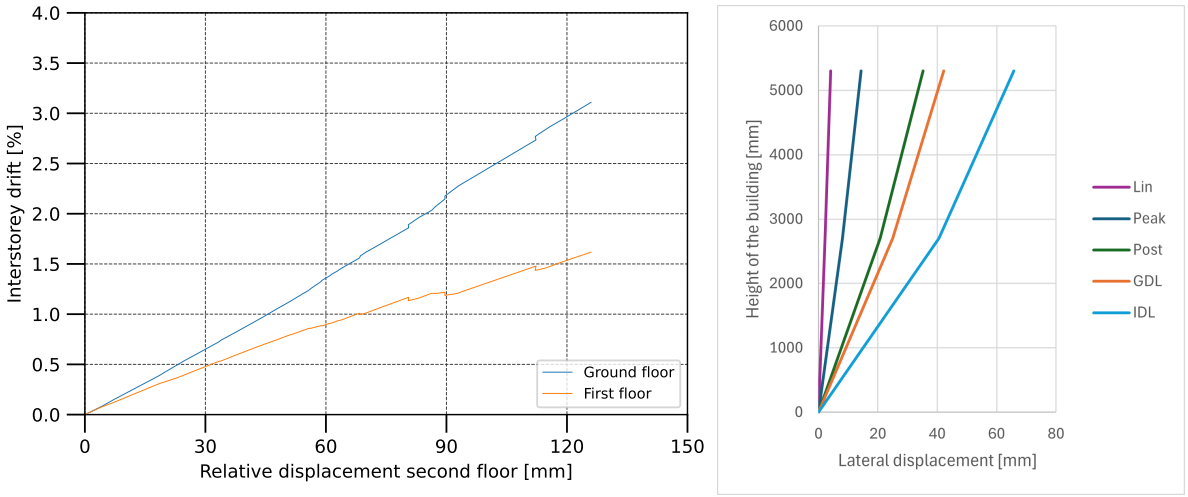

Figure 5.32: Interstorey drift of ground- and first floor and displacement profile of model 300 mm

5.3.5 MODEL WITH SPANDREL HEIGHT 400 MM

The model with a spandrel height of 400 mm, as presented in 5.2d, is discussed in this section. The spandrels in this model have a height of 400 mm, which is equal to two finite elements in the model.

CAPACITY CURVE SPANDREL HEIGHT 400 MM

The capacity curve of the monotonic pushover analyses performed on the model with spandrel height of 400 mm is shown in Figure 5.33. This figure illustrates the base shear force, which is determined by the boundary conditions at the lower left corner of the left pier, and the displacement of the second floor at the upper left corner of the same pier, similar to the results observed in previous models.

The peak force obtained from the numerical model is 104,2 kN, marking a 6% increase compared to the peak force obtained from the model with a 300 mm spandrel height results. The increase in spandrel height increases the area of the in-plane loaded wall and decreases the height of the piers between the spandrels. The reduces height might explain a higher resistance against a rocking type of failure. The increase in spandrel height from 300 mm to 400 mm is relatively small compared to the increase from 200 mm to 300 mm, which might explain the smaller increase in maximum base shear force.

The initial stiffness and secant stiffness are plotted in the same graph. The initial stiffness obtained from the model is 27.7 kN/mm, while the secant stiffness is 18.3 kN/mm. The ratio between the two values is 0.66, which is slightly higher than the ratio found in the previous model and is associated to progressive damage.

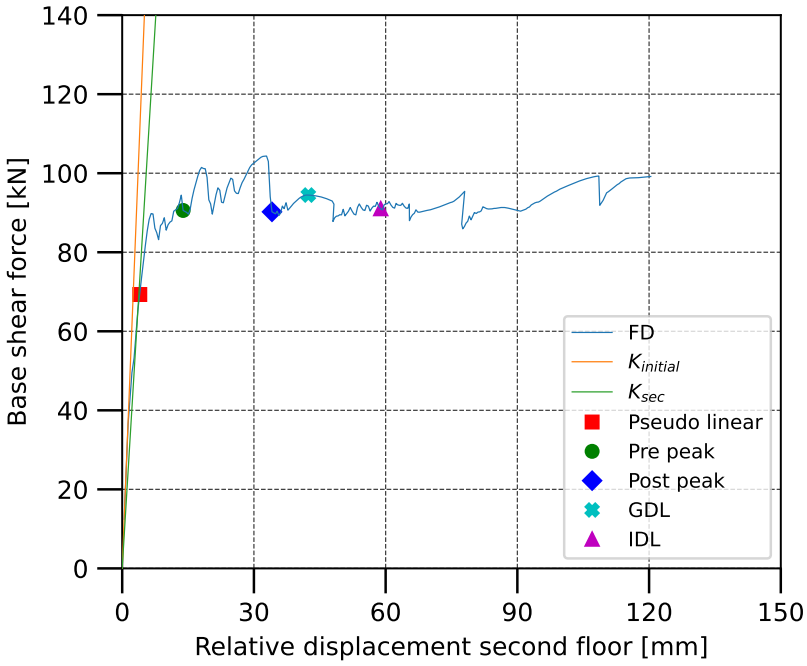

Figure 5.33: Capacity curve, initial stiffness, and secant stiffness of model with spandrel height 400 mm

CRACK EVOLUTION SPANDREL HEIGHT 400 MM

The initial signs of damage in the model, which features a spandrel height of 400 mm, manifest as cracks at the upper and lower regions of the piers, predominantly on the right-side pier. These cracks progressively expand, suggesting a rocking mechanism within both piers. Similar to the previous model at this stage, cracks begin to appear at the edge of the left pier. Cracks also start to form at the bottom of the top-right pier and the top of the bottom-left pier, at the connection with the spandrel. This phenomenon becomes apparent when the base shear force reaches 69.3 kN, coinciding with a second-floor displacement of 4.00 mm. Figure 5.34 illustrates the crack pattern at this phase, highlighting not only the piers but also the transverse walls, particularly the formation of cracks where rigid connections exist between the walls and the floor.

The primary cracks remain fixed at the top and bottom of the pier, yet they gradually spread to other sections of both the piers and the transverse walls. It is notable the cracks forming at the top of the left pier appear at the bottom of the spandrel. Diagonal shear cracks begin to appear in the lower piers, the cracks along the edge of the left pier, extend into the transverse wall on the ground floor. Cracks also start to form in the bottom spandrel predominantly on the right side of the building. These occur when the base shear force reaches 90.6 kN, coinciding with a lateral displacement of 13.9 mm on the second floor. The crack width in this stage is illustrated in Figure 5.35. As the displacement increases, diagonal cracks extend in the centre of both piers at the ground level. These shear cracks continue to evolve as the lateral displacement grows, a pattern that is evident in Figure 5.36, which shows the crack width at the point where the base shear force reaches 90.2 kN and the second-floor displacement is 34.1 mm. This pattern of cracking is observed in the post-peak phase of the pushover capacity curve. The cracks in the bottom spandrel further develop to the left and are evenly distributed. At this stage, the rigid connection between floors and transverse walls are fully cracked, except at the connection between the left transverse wall and the second floor. The cracks in the transverse wall develop at the height of the bottom of the top spandrel, similar to the adjacent pier. At the top of the bottom-left pier a horizontal crack starts to develop starting from the connection with the spandrel.

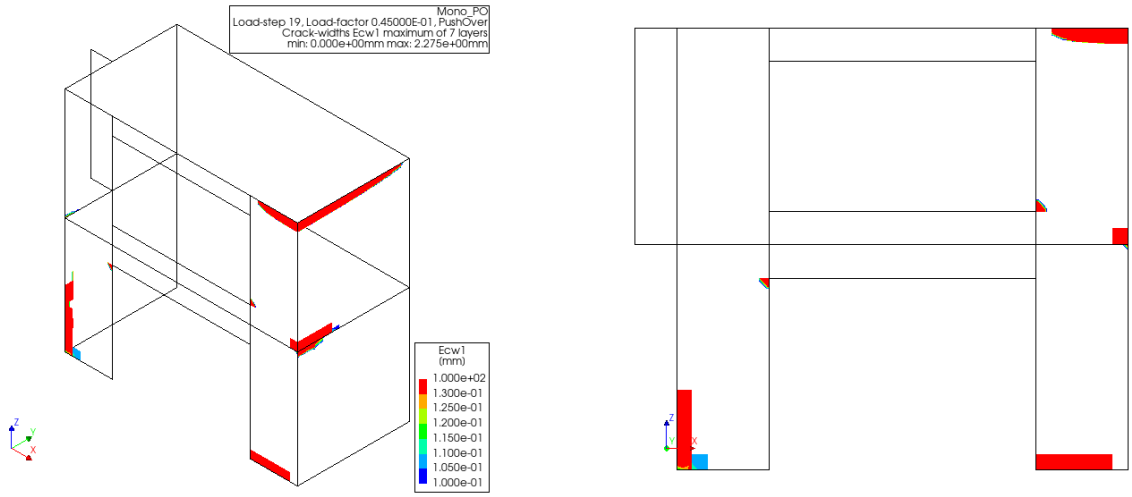

Figure 5.34: Crack pattern in the pseudo linear stage of model 400 mm

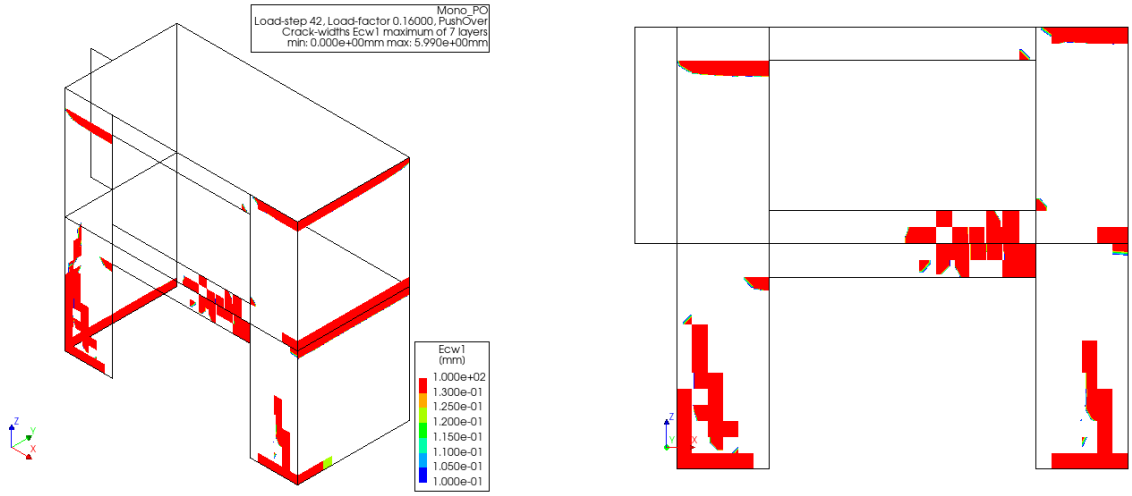

Figure 5.35: Crack pattern in the pre-peak stage of model 400 mm

The global drift limit and interstorey drift limit for the model are also determined. A global drift of 0.8% is reached in load step 110, corresponding to a base shear force of 94.5 kN and a second-floor displacement of 42.4 mm. The crack widths occurring at this stage are show in Figure 5.37. An interstorey drift of 1.5% is reached in load step 152, the limit is reached in the ground floor level. At this stage, the base shear force equals 91.0 kN, with a second-floor displacement of 58.9 mm. The cracks in this stage, shown in Figure 5.38, propagate into the left pier on the first floor and the adjacent transverse wall. Diagonal shear cracks are forming in the first-floor left pier, starting from the top. The piers at the height of the top spandrel are fully cracked. The diagonal shear cracks in both bottom piers and the cracks in the transverse wall at top spandrel height continue to grow at this stage.

INTERSTOREY DRIFT SPANDREL HEIGHT 400 MM

Figure 5.39 illustrates the interstorey drift for both the ground and first floors. It is evident that the drift experienced by the ground floor is significantly greater, than at the first floor. Consequently, the ground floor reaches the threshold limit of 1.5% interstorey drift before the first floor does. Moreover, the limit of 1.5% interstorey drift is not reached in the first floor in this analysis. This observation correlates with the distribution of cracks, which are predominantly found on the ground floor.

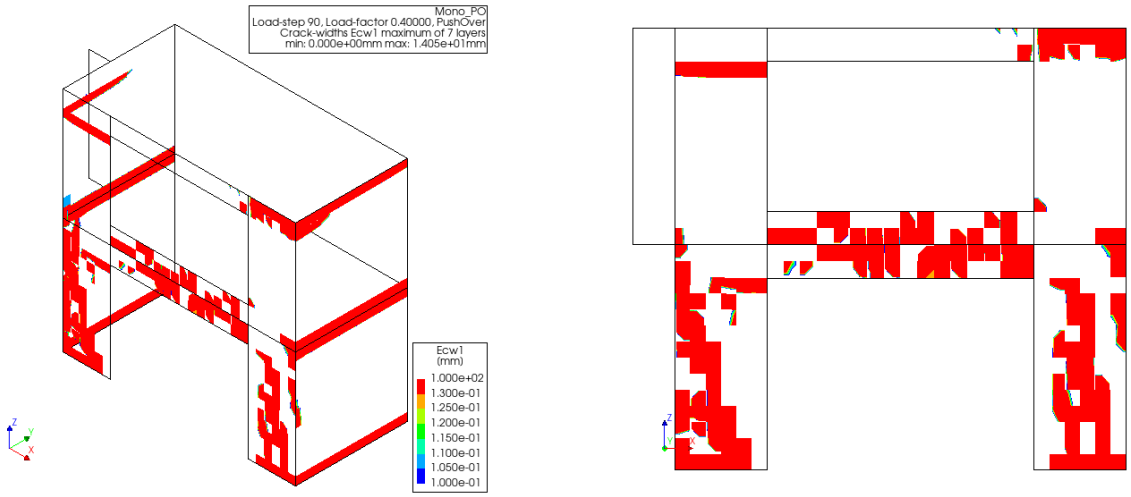

Figure 5.36: Crack pattern in the post-peak stage of model 400 mm

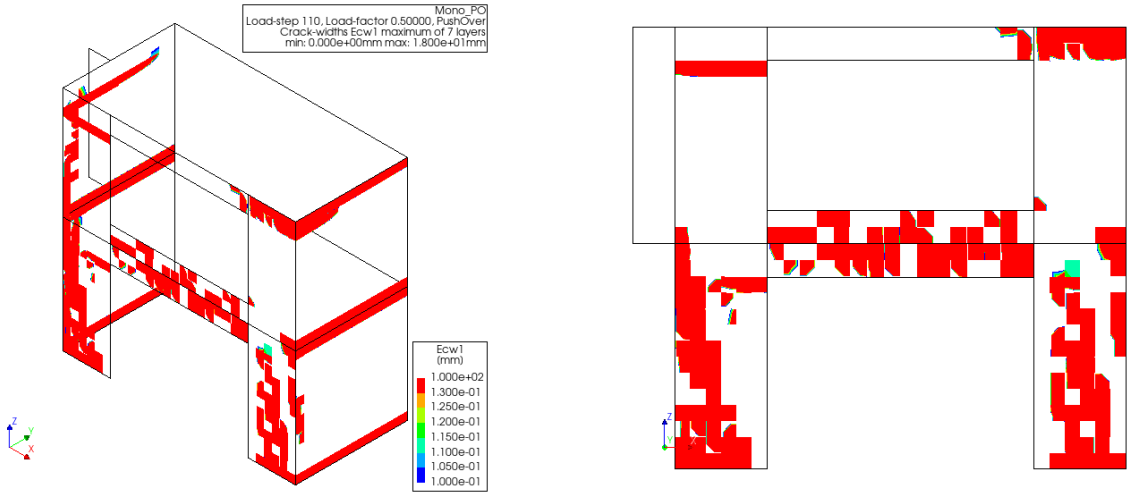

Figure 5.37: Crack width when global drift reaches 0.8% in model 400 mm

The interstorey drifts of both floors start to diverge early in the analysis, even earlier than the model with spandrel height 300 mm. As shear cracks develop in the middle of the piers at ground floor level, further damage tends to concentrate in those areas and the lower spandrel. This might explain the higher drift observed in the ground floor compared to the first floor. At a second-floor displacement around 80 mm here is a sudden change in interstorey drift, this corresponds to a point in the capacity curve where a sudden drop in capacity is present. The displacement profile of the house at the five levels marked in Figure 5.33, including the points where GDL and IDL are reached, is depicted in Figure 5.39. It is notable that the displacement profile becomes less linear compared to the previous geometries.

5.3.6 MODEL WITH SPANDREL HEIGHT 500 MM

The model with a spandrel height of 500 mm, as presented in 5.2e, is discussed in this section. The spandrels in this model have a height of 500 mm, which are represented by three finite elements. Since it is not a multiple of 200 the mesh is less regular, however not in such a way that it would influence the results.

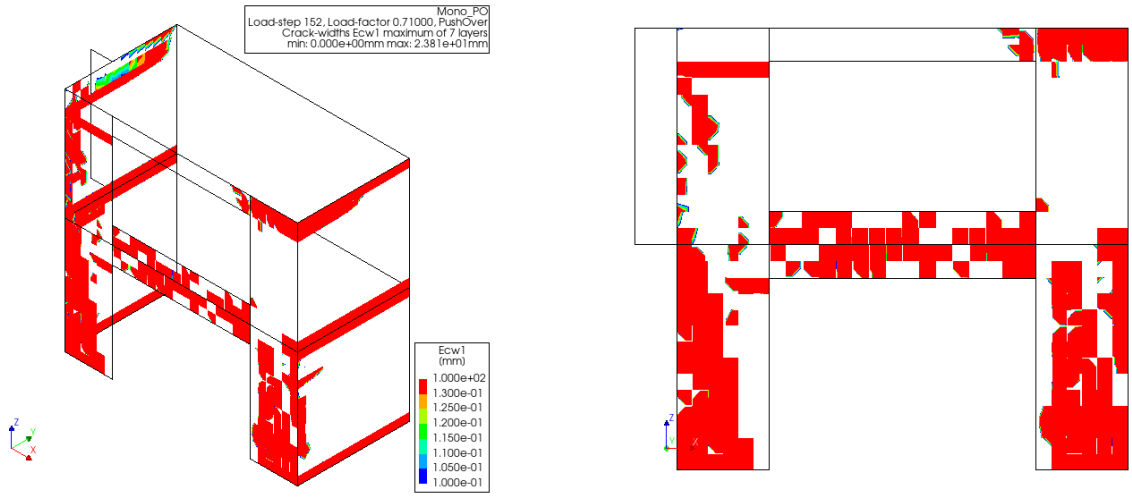

Figure 5.38: Crack width when interstorey drift reaches 1.5% in model 400 mm

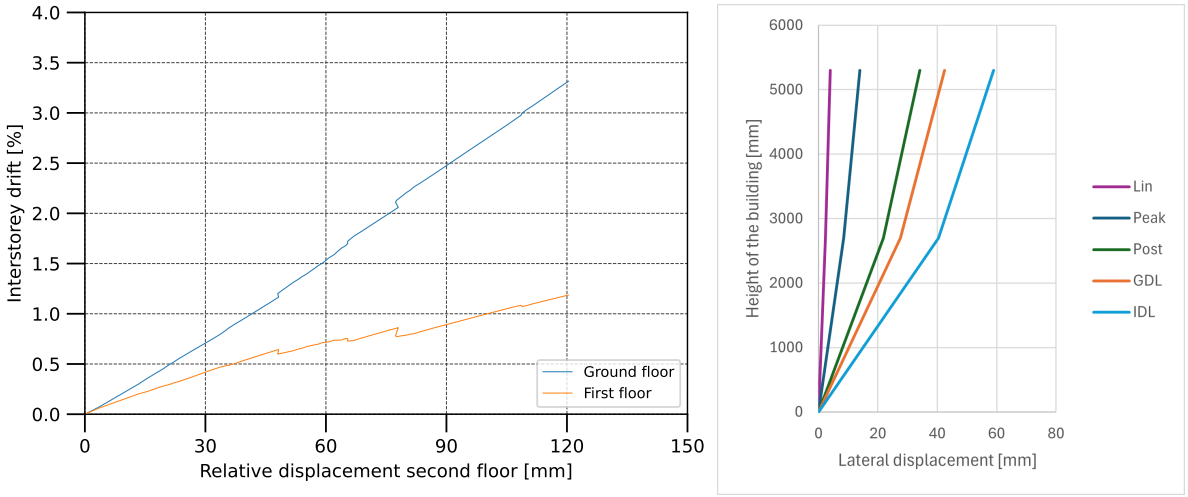

Figure 5.39: Interstorey drift of ground- and first floor and displacement profile of model 400 mm

CAPACITY CURVE SPANDREL HEIGHT 500 MM

The capacity curve of the monotonic pushover analyses performed on the model with spandrel height of 500 mm is shown in Figure 5.40. This figure illustrates the base shear force, which is determined by the boundary conditions at the lower left corner of the left pier, and the displacement of the second floor at the upper left corner of the same pier, similar to the results observed in previous models.

The peak force obtained from the numerical model is 111.5 kN, marking a 7% increase compared to the peak force obtained from the model with a 400 mm spandrel height results. The increase in spandrel height increases the area of the in-plane loaded wall and decreases the height of the piers between the spandrels. The reduces height might explain a higher resistance against a rocking type of failure. The increase in spandrel height from 400 mm to 500 mm is relatively small compared to the increase from 300 mm to 400 mm, however the increase in maximum base shear force is larger.

The initial stiffness and secant stiffness are plotted in the same graph. The initial stiffness obtained from the model is 33.0 kN/mm, while the secant stiffness is 25.6 kN/mm. The ratio between the two values is 0.78, which is significantly higher than the ratio found in the previous model and is associated with suddenly reaching the maximum capacity and less ductile behaviour.

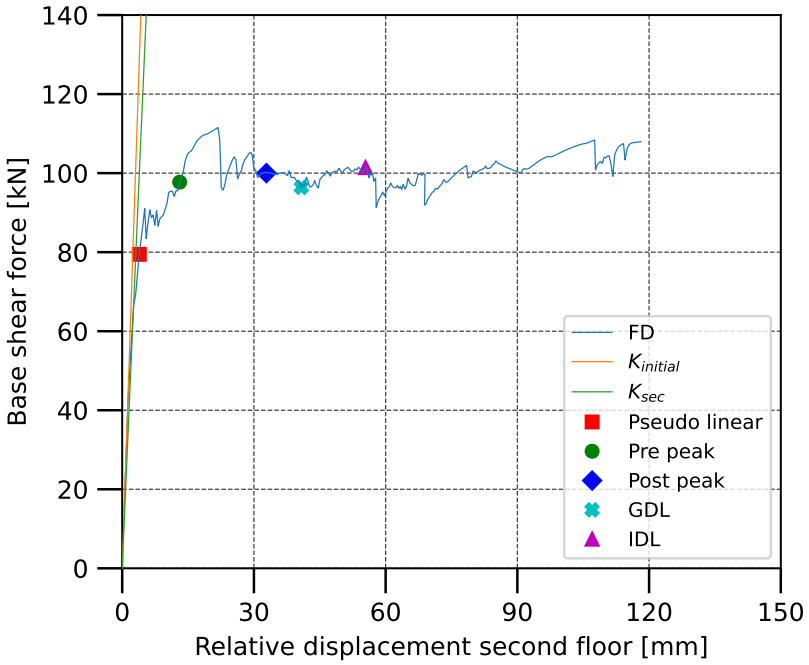

Figure 5.40: Capacity curve, initial stiffness, and secant stiffness of model with spandrel height 500 mm

CRACK EVOLUTION SPANDREL HEIGHT 500 MM

The initial signs of damage in the model, which features a spandrel height of 500 mm, manifest as cracks at the upper and lower regions of the piers, predominantly on the right-side pier. These cracks progressively expand, suggesting a rocking mechanism within both piers. Similar to the previous model at this stage, cracks begin to appear at the edge of the left pier. Cracks also start to form at the bottom of the top-right pier and the top of the bottom-left pier, at the connection with the spandrel. This phenomenon becomes apparent when the base shear force reaches 79.5 kN, coinciding with a second-floor displacement of 3.89 mm. Figure 5.41 illustrates the crack pattern at this phase, highlighting not only the piers but also the transverse walls, particularly the formation of cracks where rigid connections exist between the walls and the floor.

The primary cracks remain fixed at the top and bottom of the pier, yet they gradually spread to other sections of both the piers and the transverse walls. It is notable the cracks forming at the top of the left pier appear at the bottom of the spandrel. Diagonal shear cracks begin to appear in the lower piers, the cracks along the edge of the left pier, extend into the transverse wall on the ground floor. Cracks also start to form in the bottom spandrel predominantly on the right side of the building. Most rigid connections between transverse wall and floors or support are cracked in this stage. These occur when the base shear force reaches 97.7 kN, coinciding with a lateral displacement of 13.1 mm on the second floor. The crack width in this stage is illustrated in Figure 5.42. As the displacement increases, diagonal cracks extend in the centre of both piers at the ground level. These shear cracks continue to evolve as the lateral displacement grows, a pattern that is evident in Figure 5.43, which shows the crack width at the point where the base shear force reaches 100.0 kN and the second-floor displacement is 32.8 mm. This pattern of cracking is observed in the post-peak phase of the pushover capacity curve. The cracks in the bottom spandrel further develop to the left but are more significant on the right side. At this stage, the rigid connection between floors and transverse walls are fully cracked, except at the connection between the left transverse wall and the second floor. The cracks in the transverse wall develop at the height of the bottom of the top spandrel, similar to the adjacent pier. This behaviour is similar to that of the previous model. At the top of the bottom-left pier a horizontal crack develops and is almost fully cracked at this point.

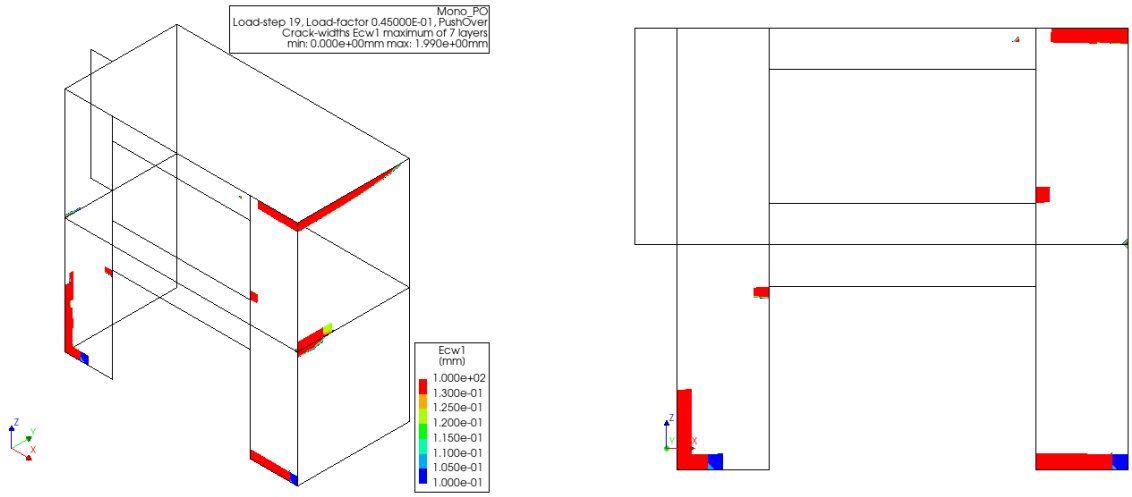

Figure 5.41: Crack pattern in the pseudo linear stage of model 500 mm

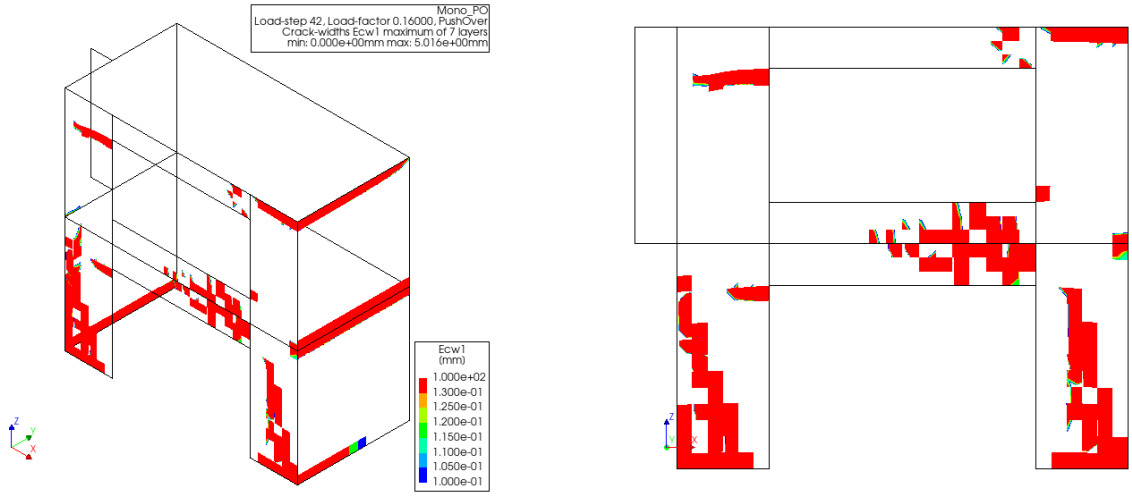

Figure 5.42: Crack pattern in the pre-peak stage of model 500 mm

The global drift limit and interstorey drift limit for the model are also determined. A global drift of 0.8% is reached in load step 110, corresponding to a base shear force of 96.4 kN and a second-floor displacement of 40.8 mm. The crack widths occurring at this stage are show in Figure 5.44. It is notable that cracks form at this stage in both transverse walls at the height of the bottom of both spandrels, starting from the piers. An interstorey drift of 1.5% is reached in load step 147, the limit is reached in the ground floor level. At this stage, the base shear force equals 101.4 kN, with a second-floor displacement of 55.4 mm. The cracks in this stage, shown in Figure 5.45, propagate into the left pier on the first floor and the adjacent transverse wall. Diagonal shear cracks are forming in the first-floor left pier, starting from the top. The piers at the height of the top spandrel are fully cracked. The diagonal shear cracks in both bottom piers and the cracks in the transverse walls at spandrel height continue to grow at this stage.

INTERSTOREY DRIFT SPANDREL HEIGHT 500 MM

Figure 5.46 illustrates the interstorey drift for both the ground and first floors. It is evident that the drift experienced by the ground floor is significantly greater, than at the first floor. Consequently, the ground floor reaches the threshold limit of 1.5% interstorey drift before the first floor does. Moreover, the limit of 1.5% interstorey drift is not reached in the first floor in this analysis. This observation correlates with the distribution

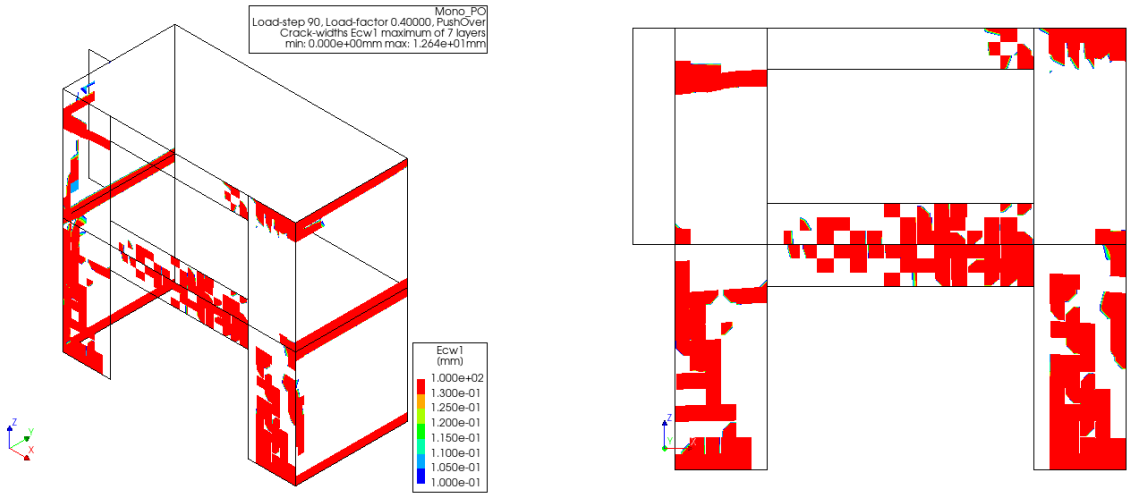

Figure 5.43: Crack pattern in the post-peak stage of model 500 mm

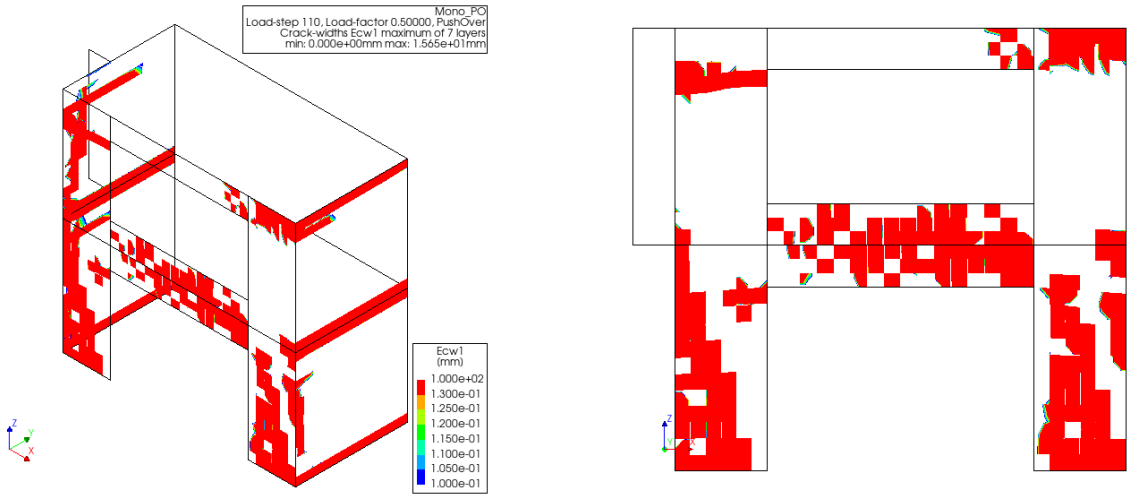

Figure 5.44: Crack width when global drift reaches 0.8% in model 500 mm

of cracks, which are predominantly found on the ground floor.

The interstorey drifts of both floors start to diverge early in the analysis, even earlier than the model with spandrel height 400 mm. As shear cracks develop in the middle of the piers at ground floor level, further damage tends to concentrate in those areas and the lower spandrel. This might explain the higher drift observed in the ground floor compared to the first floor. At a second-floor displacement around 70 mm here is a sudden change in interstorey drift, this corresponds to a point in the capacity curve where a sudden drop in capacity is present. The displacement profile of the house at the five levels marked in Figure 5.40, including the points where GDL and IDL are reached, is depicted in Figure 5.46. It is notable that the displacement profile becomes less linear compared to the previous geometries.

5.3.7 MODEL WITH SPANDREL HEIGHT 800 MM

The model with a spandrel height of 800 mm, as presented in 5.2f, is discussed in this section. The spandrels in this model have a height of 800 mm, which are represented by four finite elements. The model is used to get an insight in the behaviour in a more extreme case.

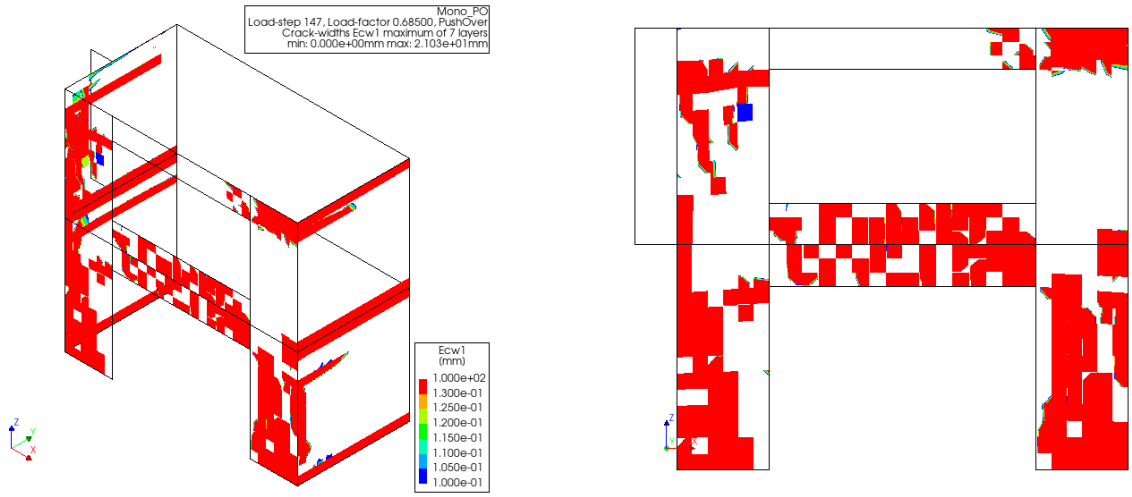

Figure 5.45: Crack width when interstorey drift reaches 1.5% in model 500 mm

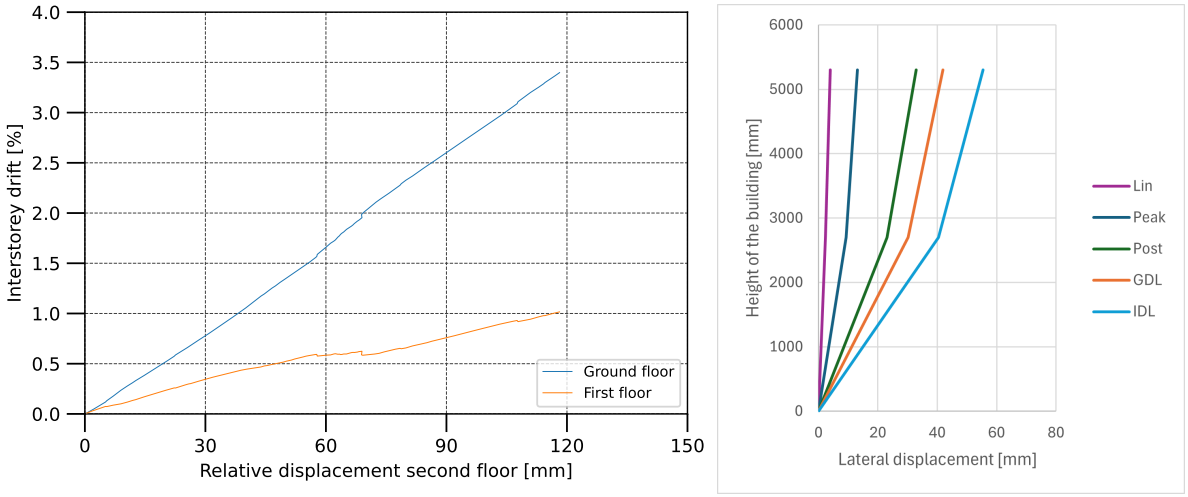

Figure 5.46: Interstorey drift of ground- and first floor and displacement profile of model 500 mm

CAPACITY CURVE SPANDREL HEIGHT 800 MM

The capacity curve of the monotonic pushover analyses performed on the model with spandrel height of 800 mm is shown in Figure 5.47. This figure illustrates the base shear force, which is determined by the boundary conditions at the lower left corner of the left pier, and the displacement of the second floor at the upper left corner of the same pier, similar to the results observed in previous models.

The peak force obtained from the numerical model is 129.8 kN, marking a 16% increase compared to the peak force obtained from the model with a 500 mm spandrel height results. The increase in spandrel height increases the area of the in-plane loaded wall and decreases the height of the piers between the spandrels. The reduces height might explain a higher resistance against a rocking type of failure. The increase in spandrel height from 500 mm to 800 mm is relatively large compared to the increase from 400 mm to 500 mm, which might explain the increase in maximum base shear force. It is notable there is an increase in base shear force after the first peak, which did not occur in the other models. The possible cause of this increase of capacity is discussed in Figure 5.4.1

The initial stiffness and secant stiffness are plotted in the same graph. The initial stiffness obtained from the model is 53.5 kN/mm, while the secant stiffness is 41.5 kN/mm. The ratio between the two values is 0.78,

which is similar to the ratio found in the previous model and is associated with suddenly reaching the maximum capacity and less ductile behaviour.

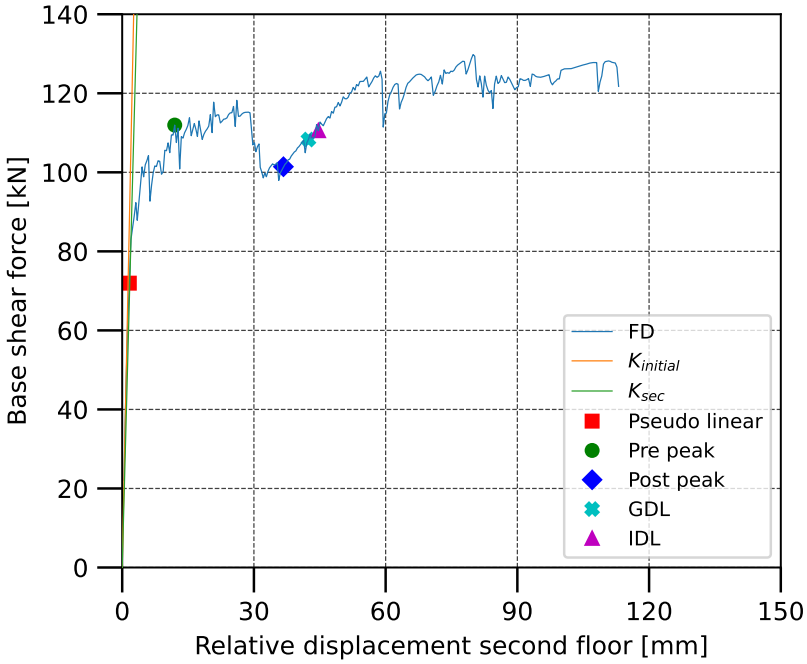

Figure 5.47: Capacity curve, initial stiffness, and secant stiffness of model with spandrel height 800 mm

CRACK EVOLUTION SPANDREL HEIGHT 800 MM

The initial signs of damage in the model, which features a spandrel height of 800 mm, manifest as cracks at the lower regions of the piers, predominantly on the right-side pier. These cracks expand into diagonal cracks, suggesting a shear mechanism within both piers. Similar to the previous model at this stage, cracks begin to appear at the edge of the left pier. Cracks also start to form at the top of the bottom-left pier, at the connection with the spandrel. This phenomenon becomes apparent when the base shear force exceeds 71.6 kN, coinciding with a second-floor displacement of 1.62 mm. Figure 5.48 illustrates the crack pattern at this phase. Up to this point, there are barely any cracks, and the behaviour remains fairly linear. However, as diagonal cracks begin to form, the behaviour becomes nonlinear.

The primary cracks remain fixed in the centre of the piers at the ground floor level, yet they gradually spread to other sections of both the piers and the transverse walls. It is notable the diagonal cracks from the right pier are extending into the right side of the bottom spandrel. Cracks are also forming at the edges between the piers and the transverse walls on the ground floor. Most rigid connections between transverse wall and floors or support are cracked in this stage. These occur when the base shear force reaches 112.0 kN, coinciding with a lateral displacement of 12.0 mm on the second floor. The crack width in this stage is illustrated in Figure 5.49. As the displacement increases, diagonal cracks extend in the centre of both piers at the ground level. These shear cracks continue to evolve as the lateral displacement grows, a pattern that is evident in Figure 5.50, which shows the crack width at the point where the base shear force reaches 101.4 kN and the second-floor displacement is 36.7 mm. At this stage, the piers and transverse walls at the level of the bottom of the lower spandrel are severely cracked. This pattern of cracking is observed in the post-peak phase of the pushover capacity curve, however, before the further increase in capacity. The cracks in the bottom spandrel further develop to the left but are more significant on the right side. At this stage, the rigid connection between floors and right transverse wall are fully cracked. The cracks in the left transverse wall develop at the height of the bottom of the lower spandrel, similar to the adjacent pier. There is a large cracked area in the right transverse wall forming at this stage.

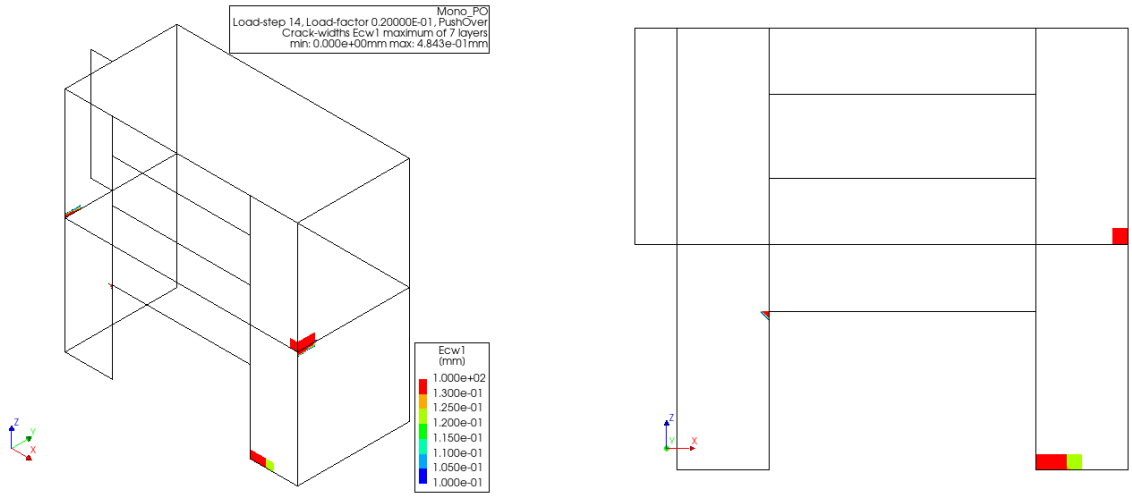

Figure 5.48: Crack pattern in the pseudo linear stage of model 800 mm

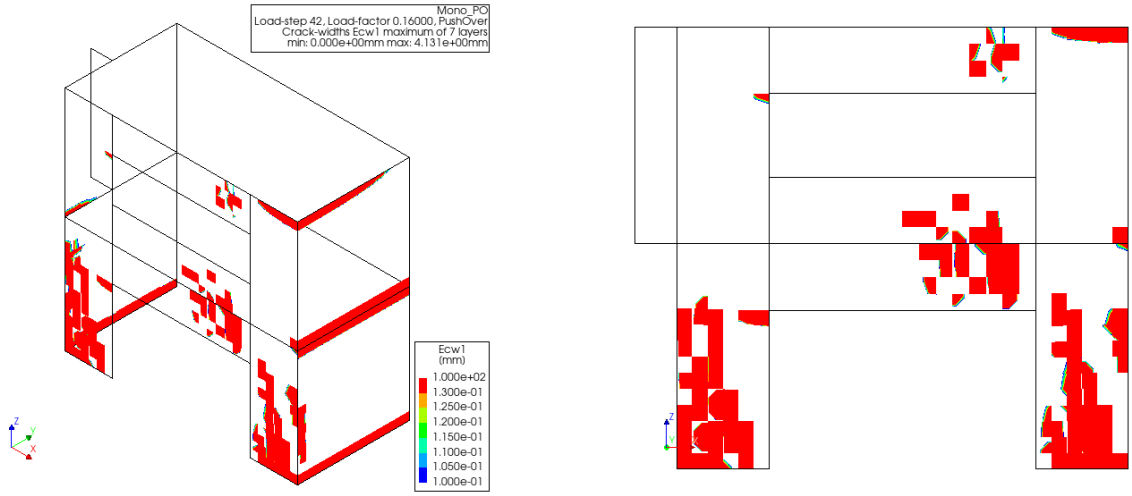

Figure 5.49: Crack pattern in the pre-peak stage of model 800 mm

The global drift limit and interstorey drift limit for the model are also determined. A global drift of 0.8% is reached in load step 126, corresponding to a base shear force of 108.3 kN and a second-floor displacement of 42.4 mm. The crack widths occurring at this stage are show in Figure 5.51. It is notable that cracks not many new cracks form at this stage, the large cracked area in the transverse wall is extending. An interstorey drift of 1.5% is reached in load step 132, the limit is reached in the ground floor level. At this stage, the base shear force equals 110.5 kN, with a second-floor displacement of 44.7 mm. The cracks in this stage, shown in Figure 5.52, are stable. Not many new cracks are formed, some new cracks occur in the lower spandrel and the large cracked area in the transverse wall is extending somewhat.

INTERSTOREY DRIFT SPANDREL HEIGHT 800 MM

Figure 5.53 illustrates the interstorey drift for both the ground and first floors. It is evident that the drift experienced by the ground floor is significantly greater, than at the first floor. Consequently, the ground floor reaches the threshold limit of 1.5% interstorey drift before the first floor does. Moreover, the limit of 1.5% interstorey drift is not reached in the first floor in this analysis. This observation correlates with the distribution of cracks, which are predominantly found on the ground floor. Almost all deformation is present in the ground floor, while the first floor is rigidly moving with it.

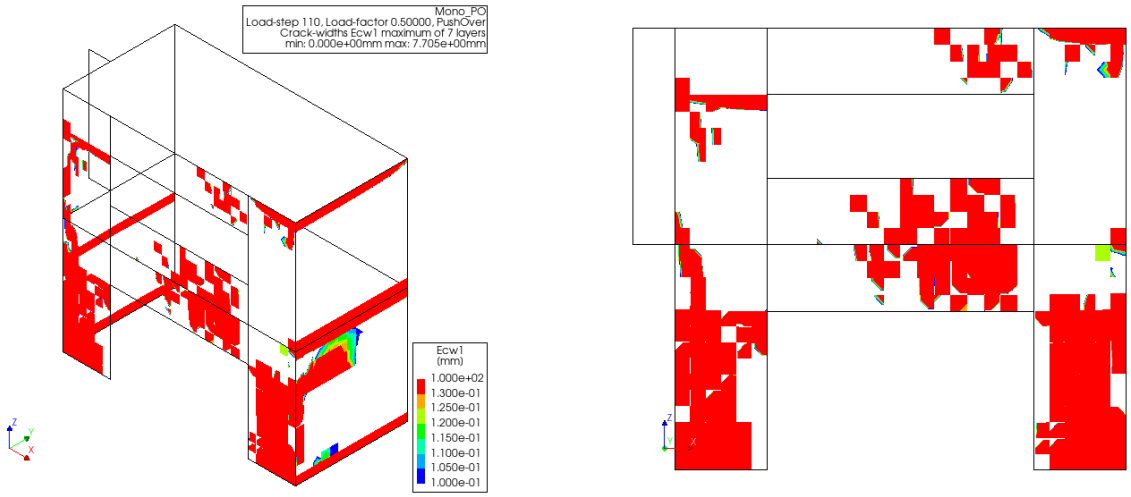

Figure 5.50: Crack pattern in the post-peak stage of model 800 mm

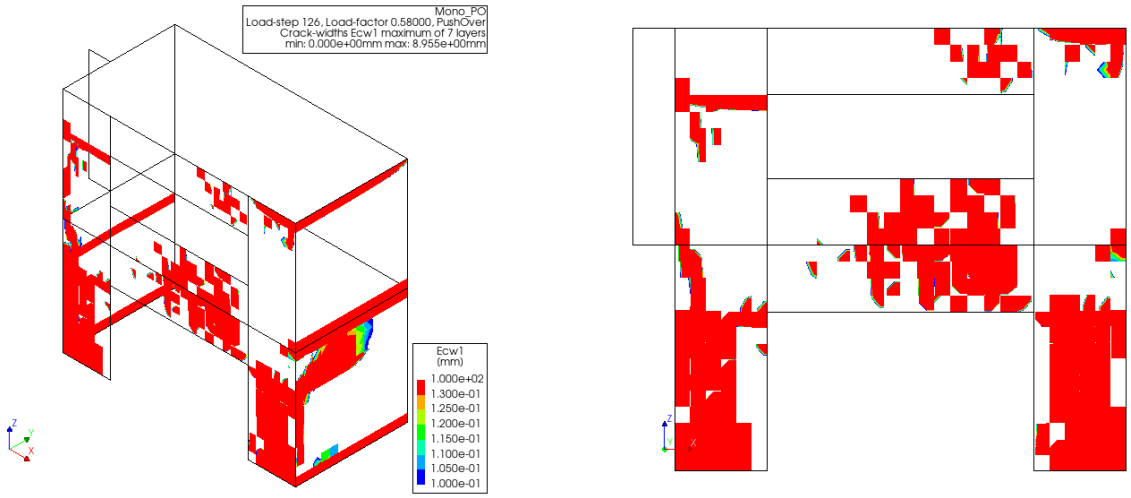

Figure 5.51: Crack width when global drift reaches 0.8% in model 800 mm

The interstorey drifts of both floors are diverging from the start of the analysis. As shear cracks develop in the middle of the piers at ground floor level, further damage tends to concentrate in those areas and the lower spandrel. After the first peak in the capacity curve the walls are all, almost fully, cracked at the height of the bottom of the lower spandrel. The displacement profile of the house at the five levels marked in Figure 5.47, including the points where GDL and IDL are reached, is depicted in Figure 5.53. It is notable that almost all deformation is in the bottom storey.

5.4 DISCUSSION AND COMPARISON

In section 5.3 the results of the NLPO analyses on the masonry house models with different geometries are shown. In this section the results are further discussed, the main goal is to compare the results of the models obtain insight in the effect of the geometry variations on the structural behaviour. The geometries are mainly compared on structural capacity, stiffness degradation and failure mechanism.

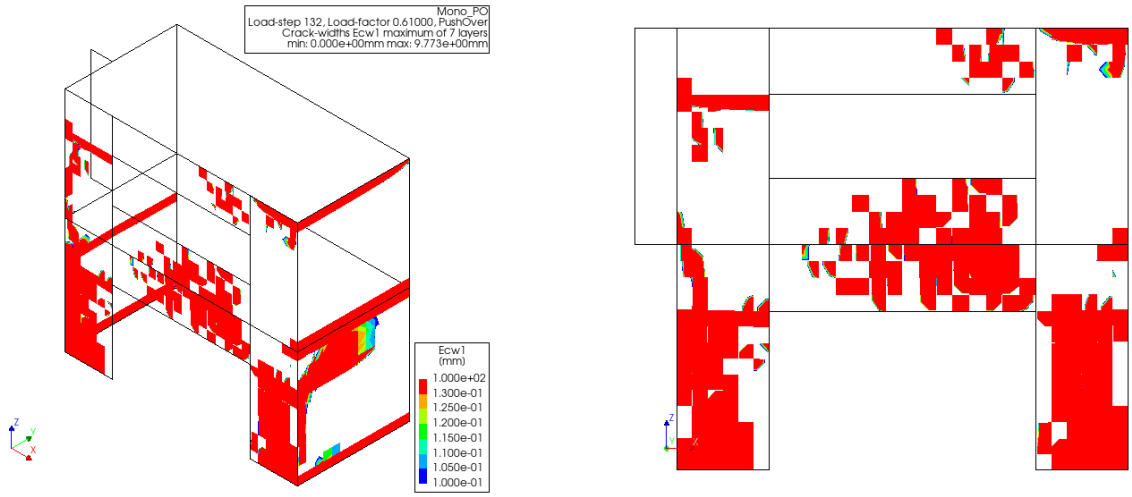

Figure 5.52: Crack width when interstorey drift reaches 1.5% in model 800 mm

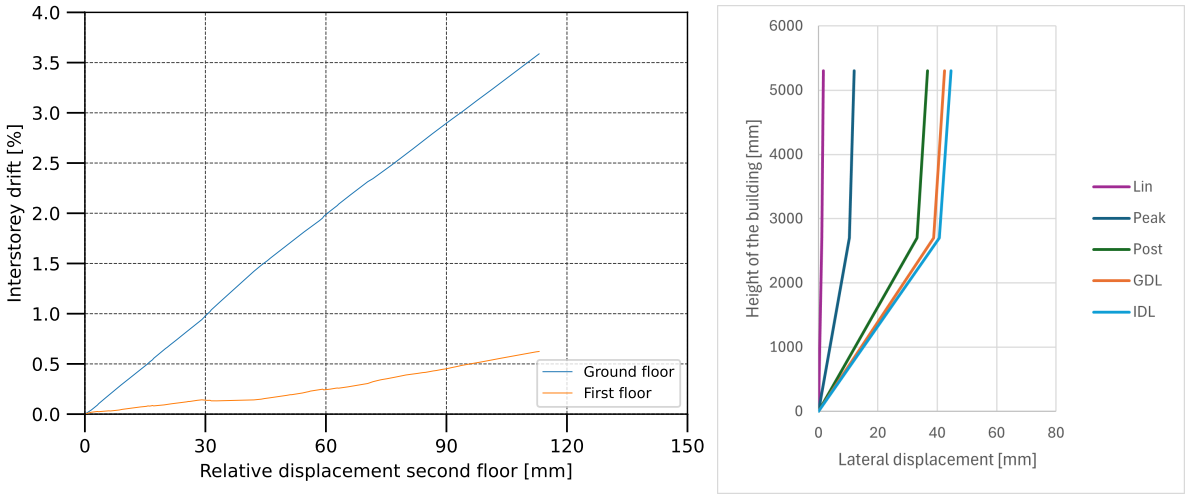

Figure 5.53: Interstorey drift of ground- and first floor and displacement profile of model 800 mm

5.4.1 STRUCTURAL CAPACITY

In Figure 5.54 the capacity curves of the models are shown. Some remarkable points in the capacity curves are indicated with arrows. The significance of these points is discussed in the following sections. There are some general trends observed in the capacity curves of the models. The observed maximum base shear force increases with spandrel height. A similar relation is observed for stiffness, both initial- and secant stiffness increase with spandrel height.

A notable change in the capacity curves is observed in the models with spandrel heights of 300 mm and more. Models with smaller spandrels show a clear peak in their capacity, while these models with higher spandrels reach a plateau where spikes in capacity are observed. Why these spikes occur is not clear. They might be caused numerically, some cracks closing, others opening, which leads to approximately the same base shear force, but not exactly. Furthermore, why the plateau occurs and no clear peak force is found in these models is not clear either. It might be related to the change in deformation profile over the height where more of the deformation concentrates in the ground floor storey without a significant reduction in the base shear force. However, there might be other reasons why this behaviour occurs in these models.

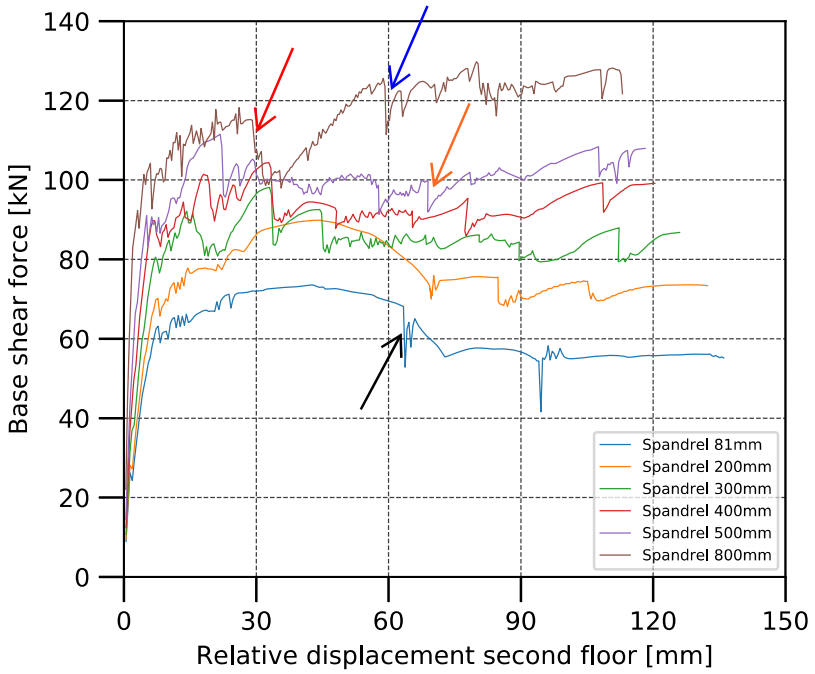

Figure 5.54: Capacity curves of geometry variations

MODEL WITH SPANDREL HEIGHT 81 MM

The model shown in Figure 5.55 is the variation with a spandrel width of 81 mm. The crack pattern is shown in two consecutive load steps indicated by the black arrow in Figure 5.54, i.e. load step 149 and load step 150. In the capacity curve a sudden drop is visible at these load steps, which could have either a physical or a numerical cause. Here it is clearly caused by a physical phenomenon, namely the sudden formation of new cracks. The cracks form mainly in the left transverse wall and the connection to the adjacent pier.

The sudden formation of cracks and the corresponding change in stiffness also results in numerical issues in this case. Due to the change in stiffness, it becomes harder to find a converged solution. Both load step 150 and 151 of the analysis did not converge, which are the only non-converged steps of the analysis. After a sudden stiffness change it could take some load steps to find a converged solution again. Load step 151 was already closer to meeting the convergence criteria again. As long as there are not many consecutive non-converged load steps, the impact on the result of the analysis is small.

MODEL WITH SPANDREL HEIGHT 500 MM

The model shown in Figure 5.56 is the variation with a spandrel height of 500 mm. The crack pattern is shown in two consecutive load steps, i.e. load step 64 and load step 65. This corresponds to the point in the capacity curve first significantly drops, around a second-floor displacement of 20 mm. It is clear from the image that a sudden increase in cracks causes this drop in capacity. From load step 64 to 65 a full crack develops at the connection between the transverse wall and the first floor. It is notable that despite the sudden change in stiffness the following load steps all find a converged solution.

Another sudden change in the capacity curve is indicated by the orange arrow in Figure 5.54, i.e. load step 178 and load step 179. This drop again is caused by the formation of new cracks, especially in the transverse walls. It is clear from Figure 5.57 that the cracks at the right transverse wall mainly develop at the same height as the spandrel. Load step 179 is the only non-converged step of the analysis. In this case the non-convergence again could be explained by the sudden change in stiffness. Since there is only one non-converged step and the out of balance force and displacement variation were not far off the convergence criteria, the impact on the result is small.

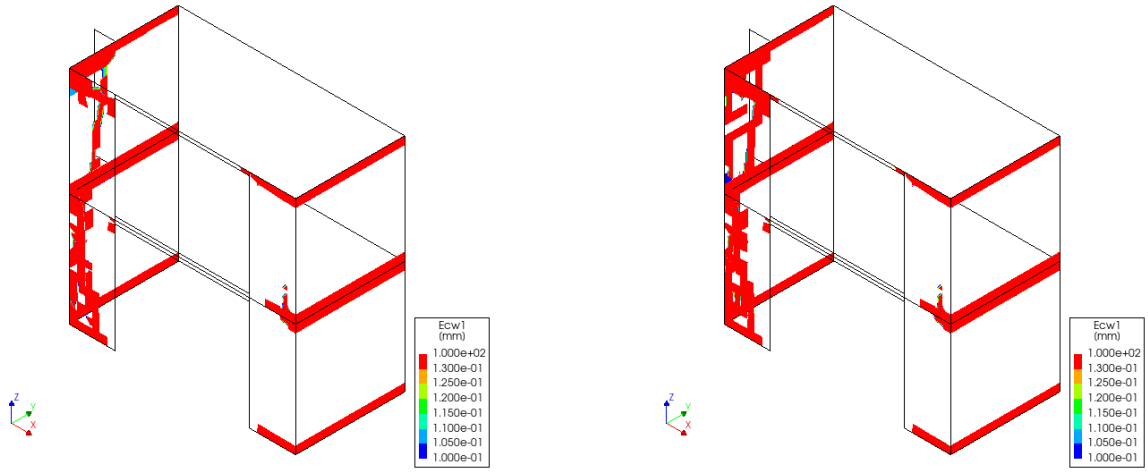

Figure 5.55: Crack pattern before and after drop in capacity model with spandrel height 81 mm

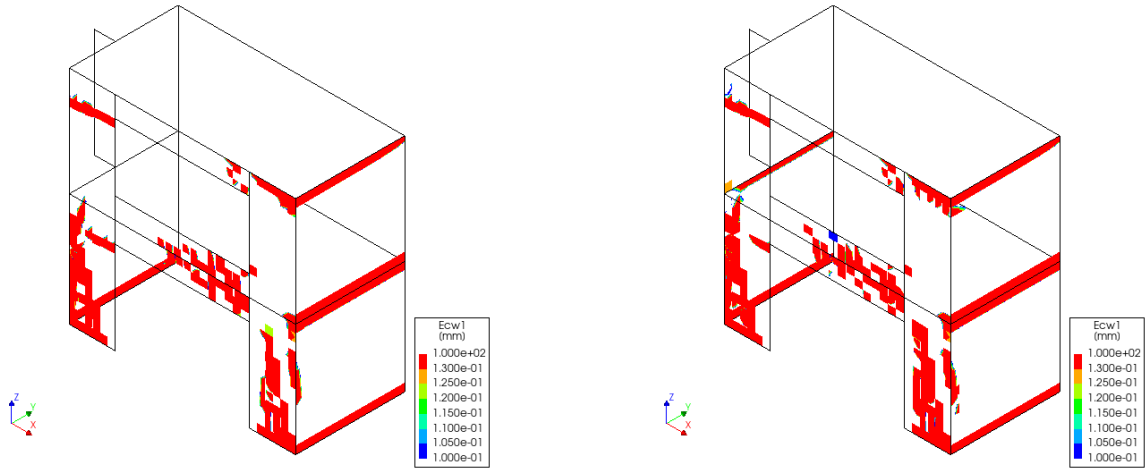

Figure 5.56: Crack pattern before and after first drop in capacity model with spandrel height 500 mm

MODEL WITH SPANDREL HEIGHT 800 MM

The model shown in Figure 5.58 is the variation with a spandrel height of 800 mm. The crack pattern is shown in two load steps indicating the start and end of the decrease in capacity marked by de red arrow in Figure 5.54, i.e. load step 80 and load step 110. The decrease in capacity is gradual in this case and corresponds to the formation of cracks in the right transverse wall. The cracks form over the height between the bottom of the lower spandrel and first floor level. Since the stiffness reduction in this phase of the analysis is more gradual due to the gradual formation of cracks, there are no numerical issues, and all load steps converged.

A more sudden change in the capacity curve of the model with spandrel height 800 is indicated by the blue arrow in Figure 5.54. It occurs at a second-floor displacement of 60 mm, corresponding to load step 170 and 171. The crack pattern in these two load steps is shown in Figure 5.59. There is not a clear cause for this sudden drop in capacity. There is some progressive crack development, however it is not extensive. Furthermore, there are no numerical issues in the analysis. All load steps in the analysis are converged.

The cracks starting to form over the height between the bottom of the lower spandrel and first floor level, as shown in Figure 5.58, further develop during the analysis. The location of these cracks was already visible in the model with spandrel height 500. By increasing the height of the spandrel, the part of the structure be-

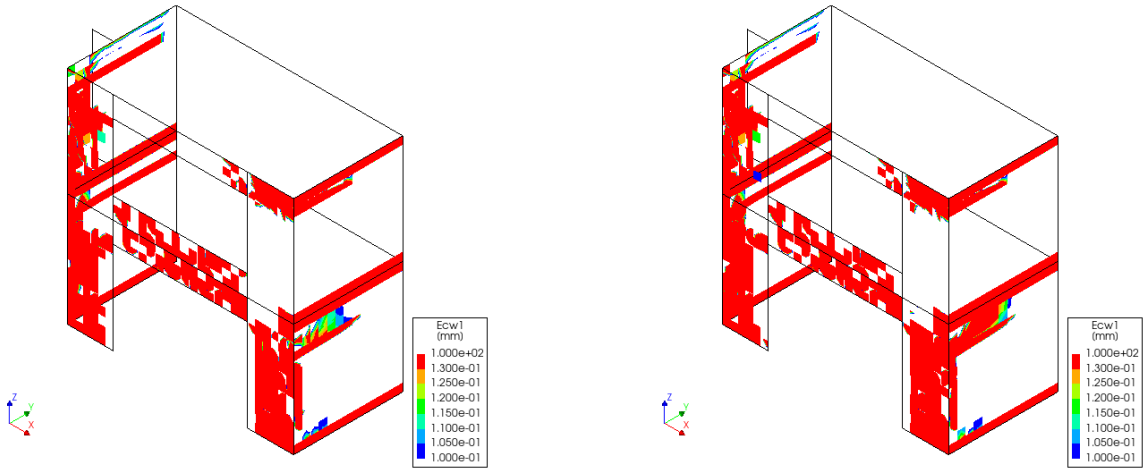

Figure 5.57: Crack pattern before and after drop in capacity model with spandrel height 500 mm

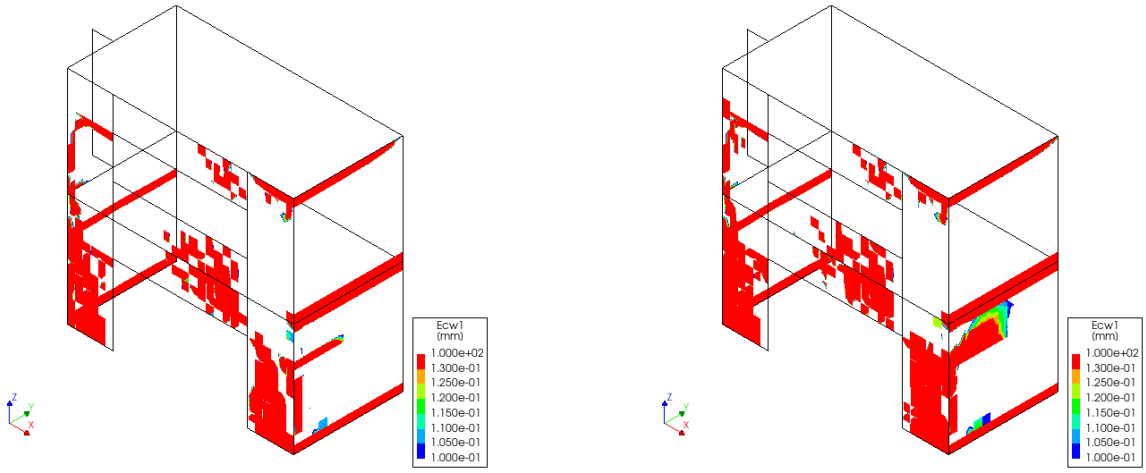

Figure 5.58: Crack pattern before and after gradual drop in capacity model with spandrel height 800 mm

comes relatively stiff, causing to transfer more load. The transverse wall on the right side of the building is loaded out of plane by the spandrel. It is the reason these cracks start to develop at the side of the spandrels and not uniform over the length of the transverse wall.

In the models with higher spandrel heights, specifically the model with spandrel height 800 mm, cracking in piers of multiple adjacent elements is observed. A result of these adjacent cracked elements is a reduced effective cross section of the pier. It requires a redistribution to transfer forces to the foundation. Additionally, when multiple adjacent integration points are cracks the crack width can no longer be accurately estimated. One single large crack might be distributed over multiple elements in the model.

After the gradual drop in capacity there is a phase of hardening. In Figure 5.60 the compressive stress distribution is shown before and after the drop in capacity. A clear change in compressive strut is observed in both piers. Especially the strut in the right pier changes. This might be the cause of the increasing capacity after the drop. A re-orientation of the strut could cause an increase in capacity due to the amount of compressive forces that can be transferred in the strut.

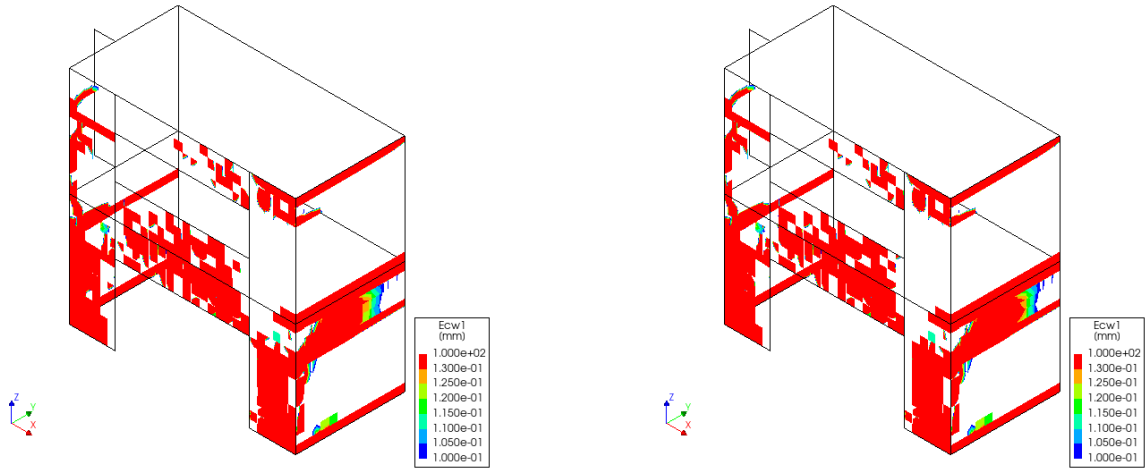

Figure 5.59: Crack pattern before and after sudden drop in capacity model with spandrel height 800 mm

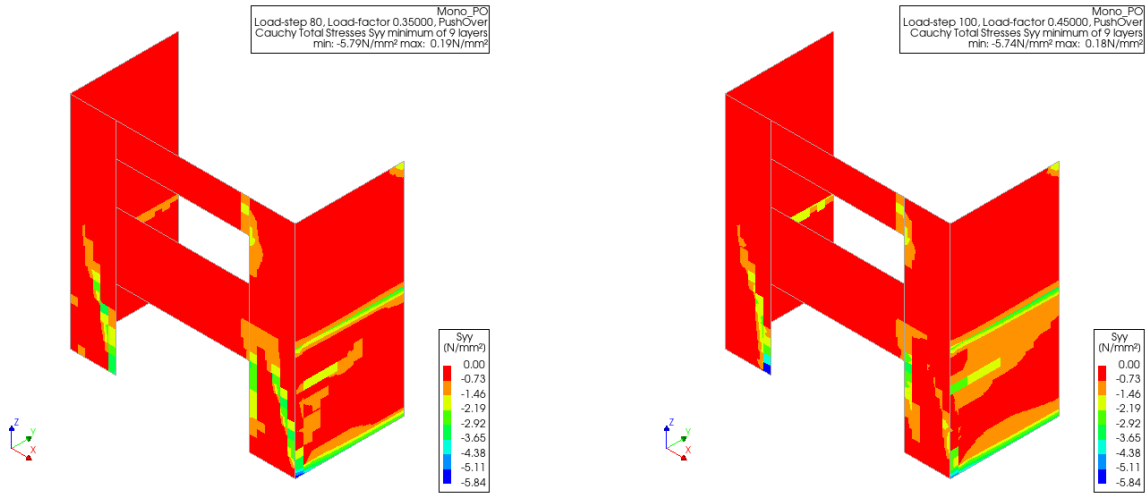

Figure 5.60: Compressive stress distribution

5.4.2 STIFFNESS DEGRADATION

During the analyses, the prescribes deformation increases and cracks in the masonry start to form. The initial pseudo linear behaviour becomes nonlinear. The initial stiffness of the models is relatively high, while the stiffness reduces quickly when the first cracks occur. In Figure 5.61 two plots are shown. The first plot shows the secant stiffness for all geometry variation in the first load steps up to a second-floor displacement of 10 mm. The second plot is similar but shows the normalized secant stiffness, based on the initial stiffness.

As shown in section 5.3 the initial stiffness of the models increases with spandrel height. Over the first load steps the secant stiffness follows the same trend, i.e. a higher spandrel results in a higher stiffness. However, it is not clear how much the stiffness degrades over the first load steps. The normalized plot provides a clearer view on the degradation. In the most extreme case, a spandrel height of 800 mm, the stiffness reduced by 80% compared to the initial stiffness. The reduction also starts at a smaller second-floor displacement. This reduction is only 60% in the model with a spandrel height of 300 mm and starts at a larger second-floor displacement.

Considering the crack plots shown in section 5.3 it is expected to see the largest relative decrease in stiffness in the models with spandrel height 500 mm and 800 mm. At the stage of the analysis where they reach a

second-floor displacement of 10 mm there is considerable cracking. In Figure 5.42 and Figure 5.49 the crack formation in these models is shown. There is already a full shear crack present in both piers in these models. This is not the case for the model with spandrel height 300 mm for example, which has a lower stiffness reduction in this stage of the analysis. In Figure 5.28 the crack formation in this stage of the analysis is shown. There are some cracks related to a rocking mechanism and the start of a shear crack in the left pier starts to from.

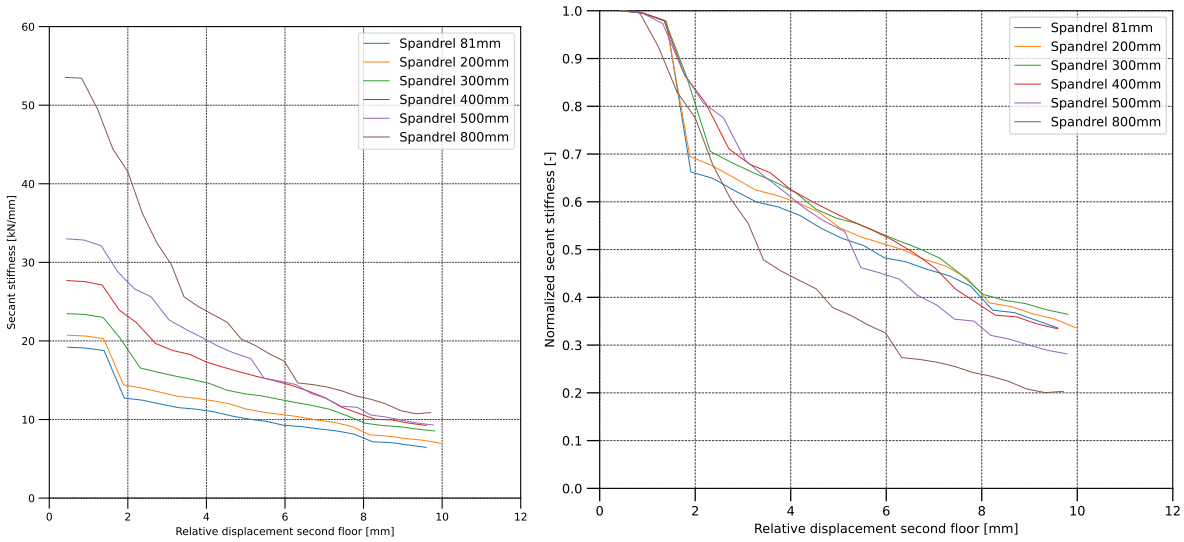

Figure 5.61: Reduction in stiffness in the first load steps of the analyses

The secant stiffness at 60% of the maximum base shear force of the capacity curve is used as a reliable equivalent stiffness to bi-linearise the force-displacement curve [68]. Comparing this secant stiffness to the initial stiffness provides insight in the stiffness degradation in the structure. If the secant stiffness and initial stiffness are close together, it suggests a sudden reach of the maximum base shear force, with many cracks occurring simultaneously, rapid stiffness degradation, and thus more brittle behaviour. Conversely, if the secant and initial stiffness are further apart, cracks occur more gradually, stiffness degrades more slowly, and the maximum base shear force is reached after considerable deformation, suggesting more ductile behaviour.

To show this the ratio between the secant stiffness and the initial stiffness for the geometry variations is plotted in Figure 5.62. The models with a spandrel height of 81 mm and 200 mm have a very similar ratio between the secant stiffness at 60% of the maximum base shear force and the initial stiffness. These two models have a very similar shape of capacity curve, with a maximum base shear force at approximately the same second-floor displacement. The subsequent models show an increasing ratio with increasing spandrel height, until the last models. These models show a maximum base shear force at decreasing second-floor displacement. The models with a spandrel height of 500 mm and 800 mm show a similar ratio. This means that for both of these models 60% of the maximum base shear force is reached at an early phase in the analysis. However, the model with a spandrel height of 500 mm reaches its maximum base shear force at a lower second-floor displacement than the model with a spandrel height of 800 mm. This does not mean the stiffness does not degrade in the latter model, there is only a phase in the analysis where the degradation occurs more slowly. However, this occurs at a stage in the analysis where the interstorey drift limit of 1.5% is reached and the structure could be considered in "Near Collapse" damage state.

5.4.3 FAILURE MECHANISMS

The observed failure mechanisms in the geometry variations are discussed in this section. It is based on the failure mechanism described in section 2.3 and the crack patterns observed in the models.

The formation of cracks along the bottom of the transverse wall, the connection with the first floor and

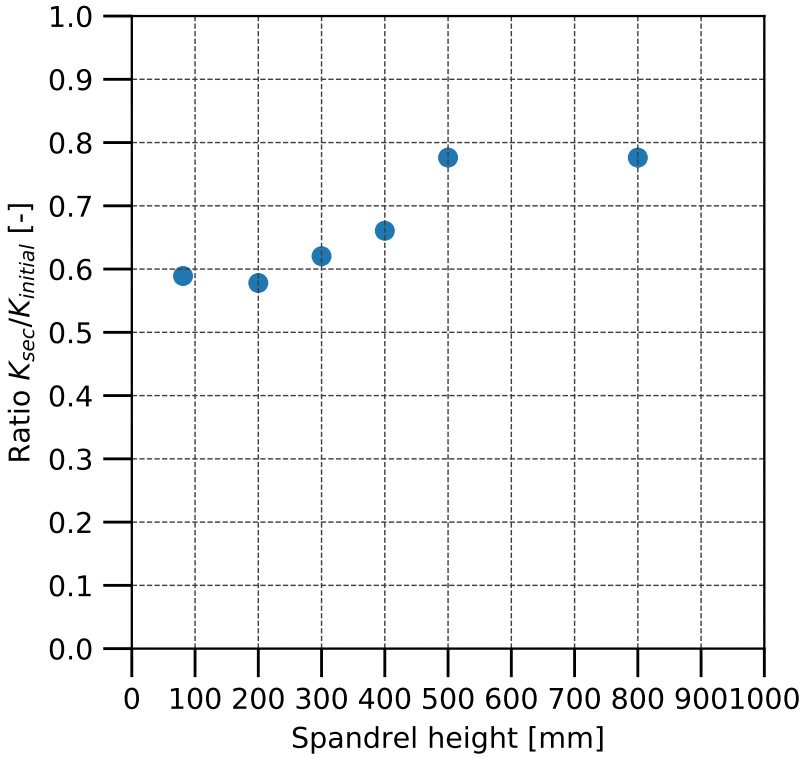

Figure 5.62: Ratio between secant stiffness at 60% of maximum base shear force and initial stiffness

the connection between the transverse wall and piers indicate a two-way out-of-plane mechanism in the transverse wall. The two-way mechanism is observed due to the use of a running bond, therefore modelling a fixed connection, between the piers and the transverse walls. The typical diagonal cracks of the two-way mechanism, as shown in 2.21b, are not present in the models. The mechanism is observed in all of the models, predominantly in the left transverse wall. The right transverse wall shows mainly cracks along the bottom of the transverse wall, the connection with the first floor. The models with a spandrel height of 300 mm and higher also show cracks along the connection between the right transverse wall and pier for large second-floor displacement. Indicating that in a late stage of the analysis, the two-way out-of-plane mechanism is also present in the right transverse wall. In that phase there is also clear crushing occurring in the right transverse wall, especially at the support and connection with the first floor, shown for the model with a spandrel height of 81 mm and 800 mm in Figure 5.63. While on one side of the cross-section cracks form the other side is subject to crushing, indicating bending stresses in the wall.

The in-plane loaded walls show a clear transition in observed failure mechanisms. However, all models show toe crushing in the right bottom corner of the left pier. This is observed in an early stage of the analysis. It is one of the reasons for the reduction in capacity of the models. The occurrence of fully crushed elements in the bottom right corner of the left pier causes the effective cross section at the bottom to reduce, since a crushed elements can no longer transfer compressive stresses.

Later in the analysis crushing occurs in the right pier at the connection with the spandrel. This is observed in all models, but a larger part of the piers is affected for the models with higher spandrels. The only exception to this is the model with spandrel height of 800 mm, which has a slightly less affected area compared to the model with a spandrel height of 500 m. It is also notable that crushing occurs in al layers of the elements, which corresponds to a compressive stress over the entire thickness of the elements. This is explained by the way the stresses are transmitted axially through the spandrel into the pier. The model with a spandrel height of 800 mm is the only model the shows a diagonal in the lower right pier in the crushing plot.

The transition in failure mechanism is best observed in the crack plots presented in section 5.3. The mod-

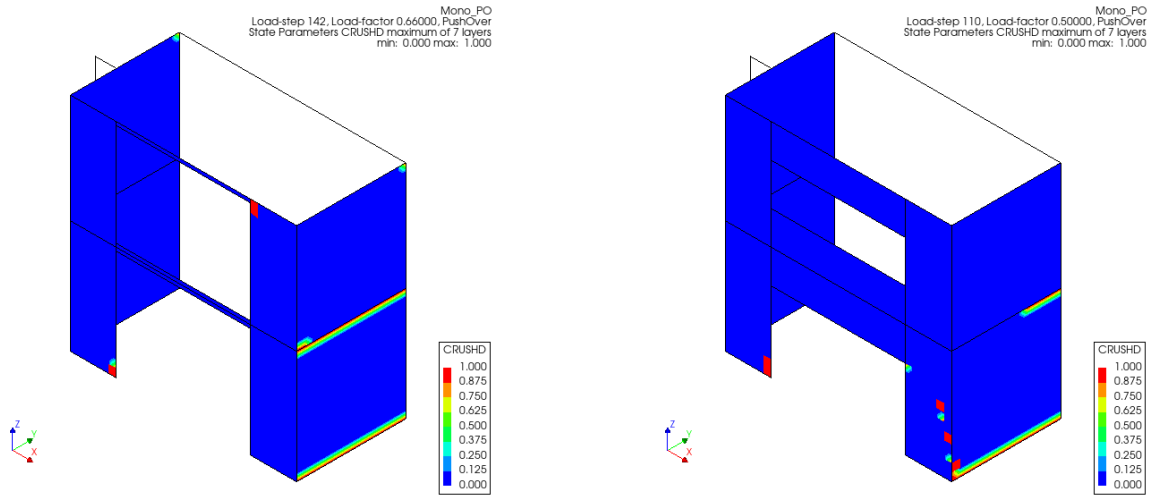

Figure 5.63: Crushing in the post-peak phase spandrel height 81 and 800 mm

els with smaller spandrel height show a rocking mechanism, which is associated to the observed toe crushing as well. With increasing spandrel height, the behaviour starts to change. The first diagonal shear cracks occur earlier in the analysis, while in the models with smallest spandrels these cracks develop well in the post-peak phase. In the model with a spandrel height of 300 mm these cracks are already developing in the stage around the peak of the capacity curve, while cracks corresponding to a rocking mechanism are still observed. This same behaviour is seen in the model with a spandrel height of 400 mm, except the diagonal shear cracks are even further developed in this stage. The only model that clearly shows diagonal shear failure in the bottom piers prior to any other cracks is the model with a spandrel height of 800 mm. With increasing deformation this model also shows development of crack patterns associated to a rocking mechanism. However, as shown in the displacement profile of this model, presented in Figure 5.53, the deformation is concentrated in the bottom storey, which is where diagonal shear cracks are prevailing.

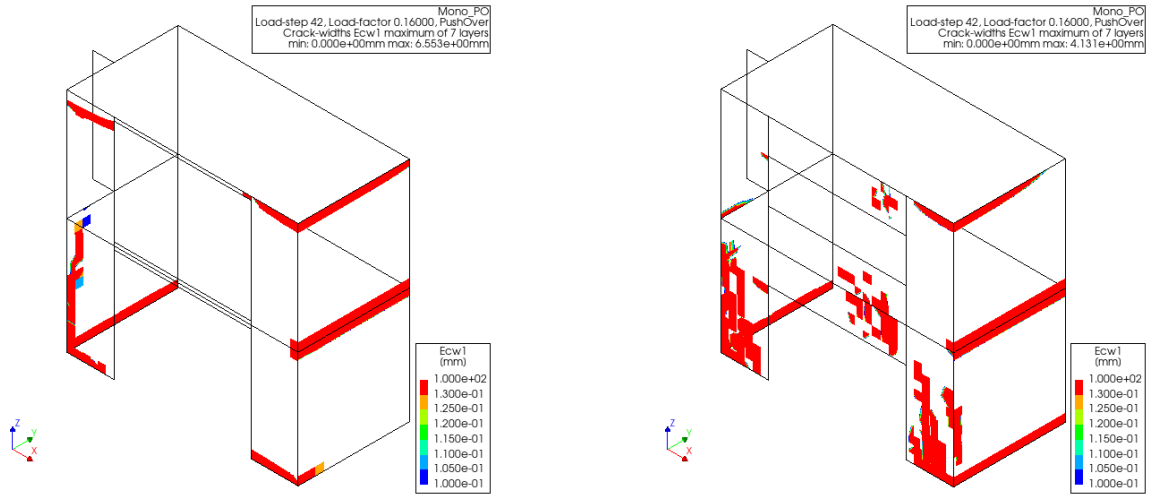

Figure 5.64: Cracking in the pre-peak phase spandrel height 81 and 800 mm

In Figure 5.64 the pre-peak crack distributions for the models with a spandrel height of 81 mm and 800 mm are shown. A clear difference in damage localization is observed. The model with spandrel height 800 mm is subject to significant cracking in the bottom piers, while the model with spandrel height 81 mm is subject to a more even distribution of cracks. In this stage of the analysis the second-floor displacement of both models is approximately equal, however the distribution of displacement over the height is different.

While the model with spandrel height 81 mm shows an almost linear distribution, i.e. interstorey drift in ground floor and first floor are similar. The distribution of deformation in the model with spandrel height 800 mm is not linear in this stage. There is a clear difference in interstorey drift between the ground floor and first floor. The ground floor shows a larger interstorey drift, in line with the concentration of damage in the piers at ground floor level.

CHAPTER 6

CONCLUSIONS AND RECOMMENDATIONS

6.1 CONCLUSIONS

The current research aimed to investigate the influence of geometry variations on structural behaviour of an unreinforced masonry building. Prior to this research, a full-scale calcium silicate brick masonry assemblage was tested in a quasi-static pushover experiment at Delft University of Technology. Based on those experimental results numerical analyses were performed to model the seismic response of the building, which served as a base for this research.

In this research the use of a monotonic nonlinear pushover analysis on a symmetrical version of the same CS masonry assemblage was performed to have a base to investigate the influence on the seismic response of masonry buildings with varying spandrel heights. Finite element models for six buildings were created with spandrel heights ranging from 81 mm to 800 mm. The seismic response of these buildings compared to the base model was discussed extensively in terms of capacity, stiffness, crack propagation and failure mechanisms.

From this research the following conclusions are drawn:

- By comparing the seismic response of the base model to the model with a spandrel height of 81 mm, equal to the floor thickness, it is shown that the introduction of spandrels of limited height does not influence the seismic response in the finite element model of the building. Both models show similar peak base shear force, initial- and secant stiffness, crack patterns and displacement distribution over the height of the building at a global drift of 0.8% and an interstorey drift of 1.5%.

- Introduction of larger spandrels to the finite element model increases the maximum base shear force, up to 85% for the model with spandrel height 800 mm compared to the base model. There is a positive relationship between the spandrel size and the maximum base shear force, i.e. increasing spandrel height results in a larger capacity.

- A similar positive relation is found for the initial- and secant stiffness of the finite element models. Stiffness increases with spandrel height, as well as the ratio between the secant- and initial stiffness. Initial- and secant stiffness increase respectively with a factor 2.82 and 3.74 for the model with spandrel height 800 mm compared to the base model. The increasing ratio between secant- and initial stiffness shows less gradual stiffness degradation with increasing spandrel height.

- Deformation behaviour is shown to be changing with increasing spandrel height. The models with a small spandrel height show a relative linear deformation over the height of the building, while the higher the spandrel height the more deformation is concentrated at the ground floor level.

- Damage in the piers occurs mainly in the bottom storey, independent of spandrel height. However, for smaller piers the damage is more significant in the left pier, while damage is more evenly distributed between piers in models with higher spandrel height. High spandrels can effectively redistribute the axial loads evenly over both piers, creating a frame effect and resulting in more evenly distributed damage over both piers.
- Smaller spandrels are associated with a rocking failure mechanism and formation of shear cracks after significant damage has already occurred. Shear cracks occur earlier in models with a larger spandrel height and become the governing failure mechanism in the model with the largest spandrel height. Toe crushing is observed in the bottom right corner of the left pier in all models and associated with a decrease in capacity.
- The out-of-plane failure mechanism in the transverse walls is influenced by spandrel height. With smaller spandrels, the out-of-plane mechanism is associated with a one-way spanning wall. Models with larger spandrels show an out-of-plane mechanism associated with a two-way spanning wall, due to cracks along the running bond connections with the piers. However, diagonal cracks commonly associated with this mechanism were not observed.
- The post-peak softening behaviour observed in the base model and the models with a spandrel height of 81 mm and 200 mm changes for the models with larger spandrels. Those models show a more or less horizontal development of the capacity curve.
- The used finite element models performed well. Drops in capacity are shown to correlate to the formation of cracks in the models. There are no significant parts of the analyses where convergence issues occurred that could influence the analysis results.
- The model with a spandrel height of 800 mm is the only model where peak base shear force is not reached before the interstorey drift limit is reached.

6.2 RECOMMENDATIONS

Based on the findings of this thesis, the drawn conclusions, the assumptions made and the shortcomings of the applied methods, the following recommendations are made to further advance the research on the topic.

- Previous research has shown that the pushover analysis method is well suited for determining an upper bound for the maximum base shear force in the structure; however, post-peak softening may be underestimated. Alternative constitutive models, such as a total strain-based crack model, could be adopted to provide a more accurate representation of post-peak material degradation. In particular, spandrel heights of 300 mm and above should be considered, as post-peak softening was less clearly observed in those buildings.
- Apart from other constitutive models, less computational demanding methods might be considered to be investigated. Based on the findings in this research a Simplified Lateral Mechanisms Analysis method could be applied to investigate how well the seismic behaviour could be determined by such a method and verify its validity for practical application.
- The analyses performed in this research are based on a macro-modelling approach, which gives insight in the global behaviour of the structure, however some detail is smeared out over the finite elements. To investigate the influence of the chosen constitutive model, other constitutive models for the smeared crack approach could be adopted. Additionally, to more extensively investigate the seismic behaviour, and more specifically the behaviour in the spandrels, a micro-modelling approach could be adopted. Both 2D- and 3D-elements could be considered, including explicit modelling of the bricks, mortar, and interface between them.
- The monotonic pushover method used in the analyses of the considered geometries in this research is based on an equal distribution of force over the first and second floor, however the models with higher spandrels show a concentration of deformation in the ground floor. For further research, the influence of the type of applied pushover method might be changed to determine the influence on structural behaviour.

- This research is based on the experimental results found during the quasi-static pushover analysis performed on the full-scale house model at Delft University of technology. In the setup of that experiment certain assumptions were made to build a typical Dutch terraced house. However, there is a large variability in houses. It is recommended to further investigate geometry variations, used materials and types of floors.
  - Additional geometry variations could include the addition of outer leaves and investigate their influence on the seismic behaviour of the structure. The cooperation between inner- and outer leaf could be determined based on the number of effective cavity wall ties per m^2.
  - Further geometry variations might investigate the influence of various common roof structures on the transfer of seismic load and the overall seismic response of the building.
  - The influence of a running bond between piers and transverse walls could be further investigated along with variations in the interface between these elements to determine the influence of connection type on the seismic behaviour.
  - The connection applied between the first floor and the piers and spandrel only transferred out-of-plane loads, it is recommended to investigate the influence of the type of connection on the seismic behaviour.
  - The calcium silicate brick masonry used in the models could be changed. The application of the method related to older or newer buildings could be investigated that way. Material properties for brick masonry could be applied for older buildings, while material properties of calcium silicate blocks could be applied for newer buildings.
  - The application of the push-over method on buildings with flexible diaphragms could be further explored, since there is a lot of buildings in the Groningen area where timber floors are present.
  - An addition to the current model could be the inclusion of lintels over the openings to support the spandrels and investigating how this influences the load transfer and seismic response of the building.
- Apart from variations on the current model, based on a typical terraced house it would be valuable to further extend the findings to different common building types in the Groningen area. For example, detached houses with large adjacent barns and how the interaction between the two parts influences its seismic behaviour. Another common type for further research is 'krimpenhuizen,' which are characterized by their wider rear section and narrow front.

BIBLIOGRAPHY

[1] G. Ravenshorst, R. Esposito, R. Schipper, F. Messali, A. Tsouvalas, E.-M. Lourens, and J. G. Rots, *Structural behaviour of a calcium silicate brick masonry assemblage: quasi-static cyclic pushover and dynamic identification test.*, Tech. Rep. (Delft University of Technology, Department of Structural Engineering, 2016).

[2] T. Xu, *Modeling the seismic response of a two-storey calcium silicate brick masonry structure with nonlinear pushover and time-history analyses*, Master's thesis, Delft University of Technology (2018).

[3] J. A. C. Barraza, *Numerical Model for Nonlinear Analysis of Masonry Walls*, Ph.D. thesis, Rheinisch-Westfälischen Technischen Hochschule Aachen (2012).

[4] T. T. Bakeer, *Collapse Analysis of Masonry Structures Under Earthquake Actions*, Ph.D. thesis, Technische Universität Dresden (2009).

[5] L. Schwer, *Laboratory tests for characterizing geomaterials,* Class Notes: Concrete and Geomaterial Modeling with LS-DYNA, Schwer Engineering and Consulting Services (2001).

[6] G. Vasconcelos, *Experimental investigations on the mechanics of stone masonry: Characterization of granites and behavior of ancient masonry shear walls*, Ph.D. thesis, Universidade do Minho (2005).

[7] H. B. Kaushik, D. C. Rai, and S. K. Jain, *Stress-strain characteristics of clay brick masonry under uniaxial compression,* Journal of Materials in Civil Engineering **19**, 728 (2007).

[8] A. V. Bergami, *Implementation and experimental verification of models for nonlinear analysis of masonry infilled r.c. frames*, Ph.D. thesis, Università degli studi ROMA TRE (2007).

[9] P. B. Lourenço, *Computational strategies for masonry structures*, Ph.D. thesis, Delft University of Technology (1996).

[10] R. van der Pluijm, *Shear behaviour of bed joints,* in *Proc. 6th North American Masonry Conference* (Philadelphia, USA, 1993) pp. 125 – 136.

[11] M. Dhanasekar, A. W. Page, and P. W. Kleeman, *The failure of brick masonry under biaxial stresses.* Proceedings of the Institution of Civil Engineers **79**, 295 (1985).

[12] A. W. Page, *The biaxial compressive strength of brick masonry.* Proceedings of the Institution of Civil Engineers **71**, 893 (1981).

[13] K. T. Doherty, *An investigation of the weak links in the seismic load path of unreinforced masonary buildings*, Ph.D. thesis (2000).

[14] J. Vaculik, *Unreinforced masonry walls subjected to out-of-plane seismic actions*, Ph.D. thesis, The University of Adelaide School of Civil, Environmental & Mining Engineering (2012).

[15] P. B. Lourenço, J. G. Rots, and J. Blaauwendraad, *Two approaches for the analysis of masonry structures: Micro and macro-modeling,* HERON **40** (1995).

[16] Wikimedia Commons, *File:fault types.svg — wikimedia commons, the free media repository,* (2024), [Online; accessed 11-September-2024].

[17] Wikimedia Commons, *File:epicenter hypocenter.svg — wikimedia commons, the free media repository,* (2022), [Online; accessed 11-September-2024].

[18] Wikimedia Commons, *File:love wave.svg — wikimedia commons, the free media repository,* (2024), [Online; accessed 11-September-2024].

[19] J. Spetzler and B. Dost, *Probabilistic seismic hazard analysis for induced earthquakes in Groningen*, Tech. Rep. (Royal Netherlands Meteorological Institute, De Bilt, 2017) update June 2017.

[20] L. Facconi, G. Plizzari, and F. Vecchio, *Disturbed stress field model for unreinforced masonry,* Journal of Structural Engineering **140**, 1 (2013).

[21] A. Tsouvalas, *Lecture Notes CIE5260 Structural Response to Earthquakes - Module II: Seismic response of simple structures* (Delft University of Technology, Delft, The Netherlands, 2017).

[22] J. Manie and W. P. Kikstra, *DIANA User's Manual: Element Library*, DIANA FEA bv, Delft, The Netherlands (2017).

[23] J. Manie and W. P. Kikstra, *DIANA User's Manual: Material Library*, DIANA FEA bv, Delft, The Netherlands (2017).

[24] Royal Netherlands Meteorological Institute, *Aardbevingen door gaswinning,* (2014), accessed: 2017-07-13.

[25] L. Evers, *Nieuwe hazardkaart groningen: daling seismische dreiging,* (2016), accessed: 2017-07-13.

[26] M. Blondet *et al.*, *Construction and maintenance of masonry houses–for masons and craftsmen,* (2005).

[27] M. Angelillo, *Mechanics of Masonry Structures*, CISM International Centre for Mechanical Sciences (Springer Vienna, 2014).

[28] A. Hillerborg, M. Modéer, and P.-E. Petersson, *Analysis of crack formation and crack growth in concrete by means of fracture mechanics and finite elements,* Cement and Concrete Research **6**, 773 (1976).

[29] J. C. Almeida, P. B. Lourenço, and J. A. O. Barros, *Characterization of brick and brick–mortar interface under uniaxial tension,* in *VII International Seminar on Structural Masonry for Developing Countries* (2002) pp. 67–76.

[30] R. van der Pluijm, *Material properties of masonry and its components under tension and shear,* in *Proc. 6th Canadian Masonry Symposium* (University of Saskatchewan, Saskatoon, Canada, 1992) pp. 675 – 686.

[31] R. H. Atkinson, B. P. Amadei, S. Saeb, and S. Sture, *Response of masonry bed joints in direct shear,* Journal of Structural Engineering **115**, 2276 (1989).

[32] A. Anthoine, *In-plane behaviour of masonry: A literature review*, Tech. Rep. (Commission of the European Communities, Luxembourg, 1992).

[33] J. A. Charry Ablanque, *Estudio experimental del comportamiento de paredes de obra de fábrica de ladrillo ante la acción de cargas laterales*, Ph.D. thesis (2010).

[34] S. Grabowski, *Material properties for the test in WP 7 and 8 and the verification of the design model of WP 4*, Tech. Rep. (ESECMaSE Technische Universität München., Germany, 2005).

[35] *NEN-EN 1996-1-1+A1 Eurocode 6: Ontwerp en berekening van constructies van metselwerk - Deel 1-1: Algemene regels voor constructies van gewapend en ongewapend metselwerk*, NEN (CEN, Brussels, 2013).

[36] A. W. Page, *The strength of brick masonry under biaxial compression-tension.* International journal of masonry construction. **3**, 26 (1983).

[37] C. Calderini, S. Cattari, and S. Lagomarsino, *In-plane strength of unreinforced masonry piers,* Earthquake Engineering & Structural Dynamics **38**, 243 (2009), https://onlinelibrary.wiley.com/doi/pdf/10.1002/eqe.860 .

[38] W. A. van der Mersch, *Modelling the Seismic Response of an Unreinforced Masonry Structure*, Master's thesis, Delft University of Technology (2015).

[39] U. Andreaus, *Failure criteria for masonry panels under in-plane loading*, Journal of structural engineering **122**, 37 (1996).

[40] T. J. Massart, *Multi-scale modeling of damage in masonry structures*, Ph.D. thesis, TUE : Department of Mechanical Engineering (2003).

[41] L. Gambarotta and S. Lagomarsino, *Damage models for the seismic response of brick masonry shear walls. part i: the mortar joint model and its applications,* Earthquake engineering & structural dynamics **26**, 423 (1997).

[42] G. P. A. G. Van Zijl, *Computational modelling of masonry creep and shrinkage*, Ph.D. thesis, Delft University of Technology (2000).

[43] L. Berto, A. Saetta, R. Scotta, and R. Vitaliani, *An orthotropic damage model for masonry structures,* International Journal for Numerical Methods in Engineering **55**, 127 (2002).

[44] G. Pande, J. Liang, and J. Middleton, *Equivalent elastic moduli for brick masonry,* Computers and Geotechnics **8**, 243 (1989).

[45] E. Papa, *Sulla meccanica del danneggiamento con particolare riferimento alle murature*, Ph.D. thesis, Politecnico di Milano, Dipartimento di Ingegneria Strutturale (1990).

[46] A. Anthoine, *Derivation of the in-plane elastic characteristics of masonry through homogenization theory,* International journal of solids and structures **32**, 137 (1995).

[47] R. Luciano and E. Sacco, *Homogenization technique and damage model for old masonry material,* International Journal of Solids and Structures **34**, 3191 (1997).

[48] A. Cecchi and R. Di Marco, *Homogenization of masonry walls with a computational oriented procedure. rigid or elastic block?* European Journal of Mechanics-A/Solids **19**, 535 (2000).

[49] A. Cecchi and R. Di Marco, *Homogenized strategy toward constitutive identification of masonry,* Journal of engineering mechanics **128**, 688 (2002).

[50] A. Zucchini and P. B. Lourenço, *A micro-mechanical model for the homogenisation of masonry,* International Journal of Solids and Structures **39**, 3233 (2002).

[51] T. J. Massart, R. H. J. Peerlings, and M. G. D. Geers, *Mesoscopic modeling of failure and damage-induced anisotropy in brick masonry,* European Journal of Mechanics-A/Solids **23**, 719 (2004).

[52] J. G. Rots, *Computational modeling of concrete fracture*, Ph.D. thesis, Technische Universiteit Delft (1988).

[53] USGS Earthquake Hazards Program, *Earthquake glossary: fault,* (n.d.), accessed: 2018-06-13.

[54] USGS Earthquake Hazards Program, *Earthquake glossary: hypocentre,* (n.d.), accessed: 2018-06-13.

[55] USGS Earthquake Hazards Program, *Earthquake glossary: epicentre,* (n.d.), accessed: 2018-06-13.

[56] F. M. M. Mulders, *Modelling of stress development and fault slip in and around a producing gas reservoir*, Ph.D. thesis, TU Delft, Delft University of Technology (2003).

[57] T. Van Eck, F. Goutbeek, H. Haak, and B. Dost, *Seismic hazard due to small-magnitude, shallow-source, induced earthquakes in the netherlands,* Engineering Geology **87**, 105 (2006).

[58] S. Akkar, M. Sandıkkaya, and J. Bommer, *Empirical ground-motion models for point- and extended-source crustal earthquake scenarios in europe and the middle east,* Bulletin of earthquake engineering **12**, 359 (2013).

[59] B. Dost, M. Caccavale, T. van Eck, and D. Kraaijpoel, *Report on the expected PGV and PGA values for induced earthquakes in the Groningen area*, Tech. Rep. (Royal Netherlands Meteorological Institute, De Bilt, 2013).

[60] NAM., *Technical addendum to the winningsplan groningen 2013 – subsidence, induced earthquakes and seismic hazard analysis in the groningen field,* (2013).

[61] *NEN-EN 1998-1: Eurocode 8 - Ontwerp en berekening van aardbevingsbestendige constucties - Deel 1: Algemene regels, seismische belastingen en regels voor gebouwen*, NEN (CEN, Brussels, 2005).

[62] A. Tsouvalas, *Lecture Notes CIE5260 Structural Response to Earthquakes - Module III: Seismic Analysis of Complex Structures* (Delft University of Technology, Delft, The Netherlands, 2017).

[63] P. A. Korswagen Eguren, *Structural Damage to Masonry Housing due to Earthquake-Flood Multi-hazards*, Master's thesis, Delft University of Technology (2016).

[64] E. Sionti, *Non-linear seismic assessment & retrofitting of unreinforced masonry buildings*, Master's thesis, Delft University of Technology (2016).

[65] Y. Nakamura, G. Magenes, and M. Griffith, *Comparison of pushover methods for simple building systems with flexible diaphragms,* (2014).

[66] J. Rots, F. Messali, R. Esposito, S. Jafari, and V. Mariani, *Computational modeling of masonry with a view to groningen induced seismicity,* in *10th international conference on Structural Analysis of Historical Constructions, SAHC* (2016) pp. 13–15.

[67] S. Bhattarai, F. Messali, and R. Esposito, *NUMERICAL STUDY ON RETROFITTING MEASURES FOR LOW-RISE URM BUILDINGS*, Tech. Rep. (Delft University of Technology, Department of Structural Engineering, 2019).

[68] NEN, *Npr 9998—assessment of structural safety of buildings in case of erection, reconstruction and disapproval—induced earthquakes—basis of design, actions and resistances,* (2018).